

# INVESTIGATIONS ON POWER FLOW CONTROL AND POWER QUALITY IMPROVEMENT IN RENEWABLE ENERGY SOURCES INTEGRATED SMART GRID

Thesis

Submitted in partial fulfilment of the requirements for the degree of

DOCTOR OF PHILOSOPHY

by

NAGARAJ C



DEPARTMENT OF ELECTRICAL AND ELECTRONICS ENGINEERING,  
NATIONAL INSTITUTE OF TECHNOLOGY KARNATAKA,  
SURATHKAL, MANGALORE -575025

November, 2019



# DECLARATION

*by the Ph.D. Research Scholar*

I hereby *declare* that the Research Thesis entitled “**Investigations on Power Flow Control and Power Quality Improvement in Renewable Energy Sources Integrated Smart Grid**” which is being submitted to the **National Institute of Technology Karnataka, Surathkal** in partial fulfillment of the requirement for the award of the Degree of **Doctor of Philosophy** in **Department of Electrical and Electronics Engineering** is a *bonafide report of the research work carried out by me*. The material contained in this Research Thesis has not been submitted to any University or Institution for the award of any degree.

.....

Nagaraj C, 138037EE13F02

Department of Electrical and Electronics Engineering

Place: NITK-Surathkal

Date:



# CERTIFICATE

This is to *certify* that the Research Thesis entitled “**Investigations on Power Flow Control and Power Quality Improvement in Renewable Energy Sources Integrated Smart Grid**” submitted by **Nagaraj C** (Register Number: 138037EE13F02) as the record of the research work carried out by him, is *accepted as the Research Thesis submission* in partial fulfillment of the requirements for the award of degree of **Doctor of Philosophy**.

Dr. K. Manjunatha Sharma  
(Research Guide)

Dr. K. N. Shubhanga  
(Chairman-DRPC, EEE dept.)



## Acknowledgements

It gives me immense pleasure and great sense of satisfaction to express my heartfelt gratitude to those who made this dissertation possible.

I would like to express my sincere gratitude to *Dr. K. Manjunatha Sharma* for his guidance, encouragement, and for having been my Ph.D. supervisor. He has been a constant source of inspiration throughout this journey. I feel proud to have worked under his guidance.

I thank National Institute of Technology Karnataka (NITK), Surathkal for giving me an opportunity for doing research and Ministry of Human Resource Development (MHRD), Government of India for awarding research scholarship.

I wish to thank my research progress assessment committee (RPAC) members *Dr. B. Venkatesa Perumal*, and *Dr. Vidya Shetty K*, for their constructive feedback and guidance.

Thanks also goes to *Dr. Jora M. Gonda*, *Dr. Vinatha U* and *Dr. B. Venkatesa Perumal*, former HODs for providing the necessary resources in the department to carry out my research. Also, I would like to thank HOD, *Dr. K. N. Shubhanga* for his thought-provoking ideas and suggestions.

I thank my dearest friend *Dr. M. V. Gururaj* who has always supported me in his capacity. Without my friends in and out of NITK Surathkal, life would have been dull.

I would like to express my deepest gratitude towards my parents, sister, son, brother in law and wife for their love and patience which kept me going in this journey. Their faith and unconditional love towards me are the reason for whatever I have achieved in my life.

Finally, I thank God Almighty for giving me strength at all times.

Nagaraj C





Dedicated to my Nation, father Chinnamadha and  
mother Puttalakshmi



# Abstract

Due to the growth of population along with suburban and urban industries, the demand for power is growing day-by-day. As the power consumption rate is high, the supply from fossil fuels is not enough to meet consumer demand. Further, the depletion of fossil fuels and environmental concern forces the extraction of power from low carbon fuels causes generation problems due to its uncertainty and intermittent nature. So, low carbon fuels such as wind, solar, etc. can therefore, be incorporated into a more efficient hybrid system.

This research work proposes a hybrid system configurations are the AC coupled micro-grid, DC coupled micro-grid, and the AC-DC coupled micro-grid. However, a significant amount of non-linear power electronic loads in the system causes power quality problems. These issues have to be addressed adequately by developing an appropriate SAPF based bi-directional control methods.

Firstly, the most implemented hybrid system around the globe is the AC coupled micro-grid. In this system, hybrid renewable energy sources or distributed generation are connected to the main-grid through individual DC-AC converters. This system is reliable because if any one of the DC-AC converters fails, the other DC-AC converter can supply power to the loads. But, the control algorithm is very complex, and also there is a need for synchronization with the main-grid.

Secondly, nowadays, more and more DC loads like LED lights are connected to the AC distribution system, which increases power quality problems and power conversion stages. These issues are taken into consideration by the DC coupled hybrid micro-grid system. This system is simpler because there is no reactive power control. Further, there is no need for synchronization to integrate renewable energy sources or distributed generations with the main-grid. However, this topology needs to restructure the current distribution system, and consequently, the cost increases drastically. Also, the DC protection system is more challenging than the AC protection system.

Lastly, based on the benefits of the individual AC and DC coupled hybrid micro-grid systems, an AC-DC coupled hybrid micro-grid system is proposed in this research work. It consists of AC renewable energy sources, and the AC loads are connected to the AC bus, whereas the DC renewable energy sources and DC loads are connected to the DC bus, thereby reducing the power conversion stages. Further, the power conversion loss calculation is also discussed by compared with the AC-DC coupled hybrid micro-grid system over individual AC and DC coupled hybrid micro-grid systems.

The shunt active power filter based  $3\phi$  4-leg DC-AC bi-directional intermediate converter using d-q load current control without a phase-locked loop is proposed to achieve the inverter-based and rectifier-based power flow between the AC and DC bus with acceptable power quality as per IEEE 519 standards at a common connecting point. The hysteresis based current control is used to compare the actual current with a reference current to generate switching pulses to drive the bi-directional intermediate converter.

The MATLAB simulation is carried out, and the performance of the proposed system is analyzed using the d-q load current control based fuzzy logic and PI controller. To validate the proposed control technique, different case studies are performed by considering balanced and unbalanced grid and load conditions with variation in renewable energy sources. The observed results demonstrate that the overall system performance improves with the d-q load current control based fuzzy logic controller.

# Contents

Abstract . . . . .	i
List of figures . . . . .	vii
List of tables . . . . .	xi
Abbreviations . . . . .	xii
<b>1 INTRODUCTION</b>	<b>1</b>
1.1 Overview . . . . .	1
1.2 Research Gaps . . . . .	5
1.3 Research Objectives . . . . .	6
1.4 Thesis Outline . . . . .	6
1.4.1 Organization of the Thesis . . . . .	6
<b>2 Performance Analysis of AC Coupled Hybrid Micro-grid System</b>	<b>11</b>
2.1 Introduction . . . . .	11
2.2 Design and Implementation of Control System . . . . .	12
2.2.1 Conventional p-q Load Current Control . . . . .	12
2.2.2 Proposed d-q Load Current Control . . . . .	13
2.2.3 Hysteresis Based Current Control . . . . .	17
2.2.4 Simulation Results for Proposed Controller Over the Conventional Controller . . . . .	18
2.2.4.1 Without RES – Balanced undistorted grid and balanced non-linear load conditions (BUGBNL) . . . . .	19
2.2.4.2 Without RES – Unbalanced distorted grid and unbalanced non-linear load conditions (UDGUNL) . . . . .	19
2.3 Overall Control Diagram of the AC Coupled Hybrid Micro-grid System	22
2.3.1 PV Array Model . . . . .	23
2.3.2 PMSG Variable Wind Turbine Model . . . . .	24

2.3.3	DFIG Variable Wind Turbine Model . . . . .	25
2.3.4	DC Link Voltage Control of the Interfacing Converter . . . . .	27
2.3.4.1	PI Controller . . . . .	27
2.3.4.2	Fuzzy logic Controller . . . . .	28
2.3.5	DC-DC Boost Converter . . . . .	29
2.3.6	Coupling Inductive Filter of the Interfacing Converter . . . . .	30
2.4	Simulation Results for AC CHM System . . . . .	30
2.4.1	AC CHM (PMSG+PV) – Balanced undistorted grid and balanced non-linear load conditions . . . . .	31
2.4.2	AC CHM (PMSG+PV) – Unbalanced distorted grid and unbalanced non-linear load conditions . . . . .	33
2.4.3	AC CHM (DFIG+PV) – Balanced undistorted grid and balanced non-linear load conditions . . . . .	35
2.4.4	AC CHM (DFIG+PV) – Unbalanced distorted grid and unbalanced non-linear load conditions . . . . .	37
2.5	Summary . . . . .	39
<b>3</b>	<b>Performance Analysis of DC Coupled Hybrid Micro-grid System</b>	<b>41</b>
3.1	Introduction . . . . .	41
3.2	Overall Control Diagram of the DC Coupled Hybrid Micro-grid System	42
3.3	Simulation Results for DC CHM System . . . . .	43
3.3.1	DC CHM (PMSG+PV) – Balanced undistorted grid and balanced non-linear load conditions . . . . .	43
3.3.2	DC CHM (PMSG+PV) – Unbalanced distorted grid and unbalanced non-linear load conditions . . . . .	46
3.4	Summary . . . . .	48
<b>4</b>	<b>Performance Analysis of AC-DC Coupled Hybrid Micro-grid System</b>	<b>51</b>
4.1	Introduction . . . . .	51
4.2	Overall Control Diagram of the AC-DC Coupled Hybrid Micro-grid System . . . . .	52
4.3	Simulation Results for AC-DC CHM System . . . . .	53
4.3.1	AC-DC CHM (PMSG+PV) – Balanced undistorted grid and balanced non-linear load conditions . . . . .	53

4.3.2	AC-DC CHM (PMSG+PV) – Balanced undistorted grid and unbalanced non-linear load conditions . . . . .	55
4.3.3	AC-DC CHM (PMSG+PV) – Unbalanced distorted grid and unbalanced non-linear load conditions . . . . .	57
4.3.4	AC-DC CHM (DFIG+PV) – Balanced undistorted grid and balanced non-linear load conditions . . . . .	59
4.3.5	AC-DC CHM (DFIG+PV) – Balanced undistorted grid and unbalanced non-linear load conditions . . . . .	61
4.3.6	AC-DC CHM (DFIG+PV) – Unbalanced distorted grid and unbalanced non-linear load conditions . . . . .	63
4.4	Summary . . . . .	65
<b>5</b>	<b>Comparative Analysis of Power Conversion Losses for Various Configurations of the Hybrid Micro-grid Systems</b>	<b>69</b>
5.1	Introduction . . . . .	69
5.2	Generalized Power Conversion Loss Analysis of the IGBT device . . . . .	70
5.3	Overall Control Diagram of the Various Topologies of the Hybrid Micro-grid Systems . . . . .	72
5.4	Simulation Results . . . . .	73
5.4.1	AC CHM (PMSG+PV) – Power flow balance and conversion losses under undistorted grid voltage conditions . . . . .	74
5.4.2	AC CHM (PMSG+PV) – Power flow balance and conversion losses under distorted grid voltage conditions . . . . .	76
5.4.3	DC CHM (PMSG+PV) – Power flow balance and conversion losses under undistorted grid voltage conditions . . . . .	78
5.4.4	DC CHM (PMSG+PV) – Power flow balance and conversion losses under distorted grid voltage conditions . . . . .	80
5.4.5	AC-DC CHM (PMSG+PV) – Power flow balance and conversion losses under undistorted grid voltage conditions . . . . .	82
5.4.6	AC-DC CHM (PMSG+PV) – Power flow balance and conversion losses under distorted grid voltage conditions . . . . .	84
5.5	Summary . . . . .	86
<b>6</b>	<b>Conclusion and Future Work</b>	<b>89</b>
6.1	Conclusion . . . . .	89

6.2	Future Work . . . . .	91
<b>A</b>	<b>Generalized Curve Fitting Approach for IGBT Device</b>	<b>93</b>
A.1	Conduction Losses of the IGBT Switch . . . . .	93
A.1.1	Transistor-conduction power loss calculation ( $P_{CL-t}$ ) . . . . .	94
A.1.2	Antiparallel diode-conduction power loss calculation ( $P_{CL-d}$ ) . . . . .	97
A.2	Switching Losses of the IGBT Switch . . . . .	100
A.2.1	Transistor-switching power loss calculation ( $P_{SL-t}$ ) . . . . .	101
A.2.2	Antiparallel diode-switching power loss calculation ( $P_{SL-d}$ ) . . . . .	102
	<b>Bibliography</b>	<b>103</b>
	<b>Publications based on the thesis</b>	<b>113</b>



# List of Figures

1.1	Block diagram of the AC coupled hybrid micro-grid system . . . . .	3
1.2	Block diagram of the DC coupled hybrid micro-grid system . . . . .	3
1.3	Block diagram of the proposed AC-DC coupled hybrid micro-grid system	4
1.4	Block diagram of the conduction and switching loss of the proposed IGBT device . . . . .	4
2.1	Conventional p-q load current control . . . . .	12
2.2	Proposed d-q load current control . . . . .	14
2.3	Phasor diagram of transformation of frames . . . . .	14
2.4	Unit vector generation without PLL . . . . .	16
2.5	Hysteresis based current control . . . . .	17
2.6	Schematic diagram of the p-q or d-q load current control . . . . .	18
2.7	Comparison waveforms for p-q and d-q load current control under BUGBNL . . . . .	20
2.8	Comparison waveforms for p-q and d-q load current control under UD-GUNL . . . . .	21
2.9	Overall control diagram of the AC CHM . . . . .	22
2.10	DC voltage regulation using FLC . . . . .	28
2.11	Input and output variables of the ETMF . . . . .	29
2.12	Power flow analysis of AC CHM with PMSG+PV under BUGBNL . . . . .	31
2.13	Harmonic analysis of AC CHM with PMSG+PV under BUGBNL . . . . .	32
2.14	Power flow analysis of AC CHM with PMSG+PV under UDGUNL . . . . .	33
2.15	Harmonic analysis of AC CHM with PMSG+PV under UDGUNL . . . . .	34
2.16	Power flow analysis of AC CHM with DFIG+PV under BUGBNL . . . . .	35
2.17	Harmonic analysis of AC CHM with DFIG+PV under BUGBNL . . . . .	36
2.18	Power flow analysis of AC CHM with DFIG+PV under UDGUNL . . . . .	37

2.19	Harmonic analysis of AC CHM with DFIG+PV under UDGUNL . . .	38
2.20	Grid and load neutral current of AC CHM under UDGUNL with a) PMSG+PV b) DFIG+PV . . . . .	39
3.1	Overall control diagram of DC CHM . . . . .	42
3.2	Power flow analysis of DC CHM with PMSG+PV under BUGBNL . .	44
3.3	Harmonic analysis of DC CHM with PMSG+PV under BUGBNL . .	45
3.4	Power flow analysis of DC CHM with PMSG+PV under UDGUNL . .	46
3.5	Harmonic analysis of DC CHM with PMSG+PV under UDGUNL . .	47
3.6	Grid and load neutral current of AC CHM with PMSG+PV under UDGUNL . . . . .	48
4.1	Overall control diagram of AC-DC CHM . . . . .	52
4.2	Power flow analysis of AC-DC CHM with PMSG+PV under BUGBNL	53
4.3	Harmonic analysis of AC-DC CHM with PMSG+PV under BUGBNL	54
4.4	Power flow analysis of AC-DC CHM with PMSG+PV under BUGUNL	55
4.5	Harmonic analysis of AC-DC CHM with PMSG+PV under BUGUNL	56
4.6	Power flow analysis of AC-DC CHM with PMSG+PV under UDGUNL	57
4.7	Harmonic analysis of AC-DC CHM with PMSG+PV under UDGUNL	58
4.8	Power flow analysis of AC-DC CHM with DFIG+PV under BUGBNL	59
4.9	Harmonic analysis of AC-DC CHM with DFIG+PV under BUGBNL	60
4.10	Power flow analysis of AC-DC CHM with DFIG+PV under BUGUNL	61
4.11	Harmonic analysis of AC-DC CHM with DFIG+PV under BUGUNL	62
4.12	Power flow analysis of AC-DC CHM with DFIG+PV under UDGUNL	63
4.13	Harmonic analysis of AC-DC CHM with DFIG+PV under UDGUNL	64
4.14	Grid and load neutral current of AC-DC CHM under UDGUNL with a) PMSG+PV b) DFIG+PV . . . . .	65
5.1	Generalized block diagram of power conversion loss analysis of IGBT device . . . . .	70
5.2	Overall control diagram of the AC CHM for power flow and conversion loss analysis . . . . .	72
5.3	Overall control diagram of the DC CHM for power flow and conversion loss analysis . . . . .	73

5.4	Overall control diagram of the AC-DC CHM for power flow and conversion loss analysis . . . . .	73
5.5	Power loss analysis of AC CHM with PMSG+PV under undistorted grid voltage . . . . .	74
5.6	Power flow analysis of AC CHM with PMSG+PV under undistorted grid voltage . . . . .	75
5.7	Power loss analysis of AC CHM with PMSG+PV under distorted grid voltage . . . . .	76
5.8	Power flow analysis of AC CHM with PMSG+PV under distorted grid voltage . . . . .	77
5.9	Power loss analysis of DC CHM with PMSG+PV under undistorted grid voltage . . . . .	78
5.10	Power flow analysis of DC CHM with PMSG+PV under undistorted grid voltage . . . . .	79
5.11	Power loss analysis of DC CHM with PMSG+PV under distorted grid voltage . . . . .	80
5.12	Power flow analysis of DC CHM with PMSG+PV under distorted grid voltage . . . . .	81
5.13	Power loss analysis of AC-DC CHM with PMSG+PV under undistorted grid voltage . . . . .	82
5.14	Power flow analysis of AC-DC CHM with PMSG+PV under undistorted grid voltage . . . . .	83
5.15	Power loss analysis of AC-DC CHM with PMSG+PV under distorted grid voltage . . . . .	84
5.16	Power flow analysis of AC-DC CHM with PMSG+PV under distorted grid voltage . . . . .	85
A.1	SKM75GB123D IGBT switch under consideration . . . . .	93
A.2	SKM75GB123D transistor characteristic curves: a) $T_{min} = 25^{\circ}\text{C}$ and b) $T_{max} = 125^{\circ}\text{C}$ . . . . .	94
A.3	Curve fitting waveform for transistor-conduction power loss at $25^{\circ}\text{C}$ with respect to $i_t$ . . . . .	95
A.4	Curve fitting waveform for transistor-conduction power loss at $125^{\circ}\text{C}$ with respect to $i_t$ . . . . .	96

A.5	SKM75GB123D diode characteristic curves at $T_{min}= 25^{\circ}\text{C}$ and $T_{max}= 125^{\circ}\text{C}$ . . . . .	98
A.6	Curve fitting graph for diode-conduction power loss at $25^{\circ}\text{C}$ with respect to $i_d$ . . . . .	99
A.7	Curve fitting graph for diode-conduction power loss at $125^{\circ}\text{C}$ with respect to $i_d$ . . . . .	99
A.8	Curve fitting graph for transistor-switching power loss at $25^{\circ}\text{C}$ with respect to $i_t$ . . . . .	101
A.9	Curve fitting graph for transistor-switching power loss at $125^{\circ}\text{C}$ with respect to $i_t$ . . . . .	101
A.10	Diode turn-off energy dissipation loss per one switching . . . . .	102

# List of Tables

2.1	Parameters of the main-grid and load . . . . .	19
2.2	Performance of the grid current THD for proposed d-q load current control over the conventional p-q load current control . . . . .	22
2.3	Parameters of the PV array model . . . . .	23
2.4	Parameters of the PMSG variable wind turbine model . . . . .	24
2.5	Parameters of the DFIG variable wind turbine model . . . . .	25
2.6	Fuzzy rule mechanism . . . . .	28
2.7	Parameters of the UIC, DC-DC boost converter, and main-grid . . .	30
2.8	Performance of the grid current THD for AC CHM system . . . . .	40
3.1	Parameters of the PMSG variable wind turbine model . . . . .	43
3.2	Performance of the grid current THD for DC CHM system . . . . .	49
4.1	Performance of the grid current THD for AC-DC CHM system . . . .	67
5.1	Comparison of the power conversion losses for AC-DC CHM over the AC and DC CHM systems . . . . .	87
A.1	$V_{ce}-i_t$ curve extracted points for $V_{ge}= 15$ V at $T_{min}= 25^{\circ}\text{C}$ . . . . .	95
A.2	$V_{ce}-i_t$ curve extracted points for $V_{ge}= 15$ V at $T_{min}= 125^{\circ}\text{C}$ . . . . .	96
A.3	$V_{ce}-i_t$ curve extracted points for $V_{ge}= 15$ V at $T_{min}= 25^{\circ}\text{C}$ . . . . .	98
A.4	$V_{ce}-i_t$ curve extracted points for $V_{ge}= 15$ V at $T_{max}= 125^{\circ}\text{C}$ . . . . .	99
A.5	Extraction of the samples for deducing the switching factor at $T_{max}= 125^{\circ}\text{C}$ . . . . .	102

## List of Abbreviations

AC	Alternating current
DC	Direct current
RES	Renewable energy sources
DGs	Distributed generations
SAPF	Shunt active power filter
PV	Photovoltaic
DFIG	Doubly fed induction generator
RSC	Rotor side converter
GSC	Grid side converter
PMSG	Permanent magnet synchronous generator
UIC	Unidirectional interfacing converter
PLL	Phase-locked loop
BIC	Bi-directional intermediate converter
IGBT	Insulated-gate bipolar transistor
HBCC	Hysteresis based current control
PI	Proportional controller
FLC	Fuzzy logic controller
ETMF	Equilateral triangular membership function
CHM	Coupled hybrid micro-grid
HSWES	Hybrid solar-wind energy sources
BUGBNL	Balanced undistorted grid and balanced non-linear load
BUGUNL	Balanced undistorted grid and unbalanced non-linear load
UDGUNL	Unbalanced distorted grid and unbalanced non-linear load
THD	Total harmonic distortion
CCP	Common connecting point
LED	Light emission diode

# Chapter 1

## INTRODUCTION

The use of renewable energy is essential for the world as global energy consumption is increasing, while fossil fuel energy sources are no longer sufficient to satisfy the energy demand. Thus, the growing demand for energy and the depletion of fossil fuel resources has motivated the researcher to discover a sustainable solution. In this context, renewable energy sources (RES) or distributed generations (DGs) offer a broad range of possibilities. The RES can be integrated with a stand-alone system or grid-connected system. Due to the capital cost, maintenance cost, and chemical pollution of the battery, the stand-alone system is less feasible in terms of medium- and large-scale power generation. Hence, the grid-connected system is quite suitable over the stand-alone system, as it ensured maximum utilization of the RES. In the present research work, investigations were carried out for power flow control and power quality improvements for the RES integrated grid system.

### 1.1 Overview

The management of the electric power network becomes more difficult with the increase in customer load demand. In the power distribution system, the intermittent solar-wind RES and non-linear power electronic loads connected to the main-grid cause harmonics, which deteriorate the power quality of the system. The micro-grid suffers from power generation issues because of the intermittent RES and power electronics applications. These issues were taken into consideration effectively by the shunt active power filter (SAPF) to limit the grid current harmonics with real and reactive power generation simultaneously (Tareen et al., 2017).

The SAPF has been extensively studied only with grid-connected AC coupled RES or DGs, which are applied to the unidirectional power flow transfer to the AC grid side with active power filtering (Moreira et al., 2017, Mehrasa et al., 2016, Singh et al., 2010). The grid-connected AC coupled RES consists of DC sources like the Photovoltaic (PV) array, fuel cell, etc. or AC sources like the Doubly fed induction generator (DFIG) wind, Permanent magnet synchronous generator (PMSG) wind, etc. These sources are connected to the DC-AC unidirectional interfacing converter (UIC) through the converters to supply AC or DC loads on the AC grid side with current harmonics mitigation. Further, the compensation of reactive power and neutral current was carried out. Among these features, the harmonic currents mitigation plays a significant role as the number of non-linear loads are increasing day-by-day in the power distribution system.

In (Song and Nian, 2014, Sun and Wang, 2016, Hu et al., 2014), the back-to-back converter controls of the DFIG variable wind with a phase-locked loop (PLL) was developed to mitigate the stator and rotor current harmonics under non-ideal harmonic grid voltage conditions. An appropriate design of the PLL was employed to synchronize with the main-grid. Grid synchronization with high accuracy is a critical requirement for the control system of the grid-connected converters. So, the performance of the direct power control strategies of the DFIG variable wind is highly dependent on the frequency or phase-detection accuracy of the PLL. To overcome this challenge, the back-to-back converter controls of the DFIG variable wind without PLL was developed to mitigate the grid harmonic currents under non-ideal harmonic grid voltage conditions (Nian et al., 2015, Li et al., 2017). The available state-of-art literature in the SAPF focuses only on unidirectional power flow applications.

The research articles published on micro-grid were on converter control of the power flow management, voltage and frequency variations, etc. (Rajesh et al., 2017, Fooladivanda et al., 2017, Boukettaya and Krichen, 2014, Khanh et al., 2010). The power quality analysis was carried out with the effect of a grid-connected AC coupled hybrid micro-grid system consisting of solar or wind under balanced undistorted grid and balanced non-linear load scenarios (Munir and Li, 2013, Kumar and Zare, 2015, Sivakumar and Arutchelvi, 2018).

In the grid-connected AC coupled hybrid micro-grid system (Majumder, 2013, Justo et al., 2013), the AC or DC DGs/RES has converted to AC through AC-DC converters, DC-DC boosters, and DC-AC converters to supply AC linear/non-linear loads.



Also, the AC-DC and DC-DC converters are required to supply DC voltages for the DC loads as shown in Figure 1.1.

In the grid-connected DC coupled hybrid micro-grid system (Yi et al., 2018, Eid, 2014), the AC or DC supply from DGs/RES are converted to DC through the AC-DC converters and DC-DC boosters to supply DC loads. The DC-AC converters are necessary to supply AC loads as shown in Figure 1.2. The role of a bi-directional

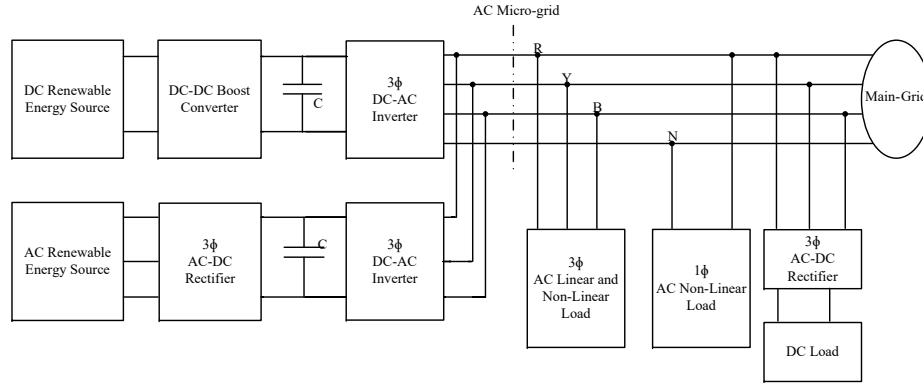


**Figure 1.1:** Block diagram of the AC coupled hybrid micro-grid system

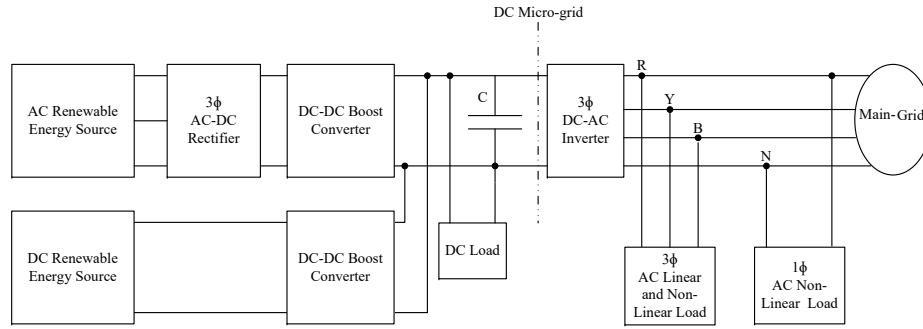


**Figure 1.2:** Block diagram of the DC coupled hybrid micro-grid system

intermediate converter (BIC) in (Liu et al., 2011, Liang et al., 2019, Wang et al., 2013, Nejabatkhah and Li, 2014, Eghtedarpour and Farjah, 2014) had studied for bi-directional power flow control between the AC and DC bus, but the power quality and power conversion losses were not evaluated.

In both the AC and DC coupled hybrid micro-grid system, because of the DC-AC-DC/AC-DC-AC power conversion stages, more losses has encountered, which reduces the efficiency of the overall system. Therefore, in the present research work, the AC-

DC coupled hybrid micro-grid system is proposed with minimum power conversion stages and losses as shown in Figure 1.3. Figure 1.4 represents the generalized block

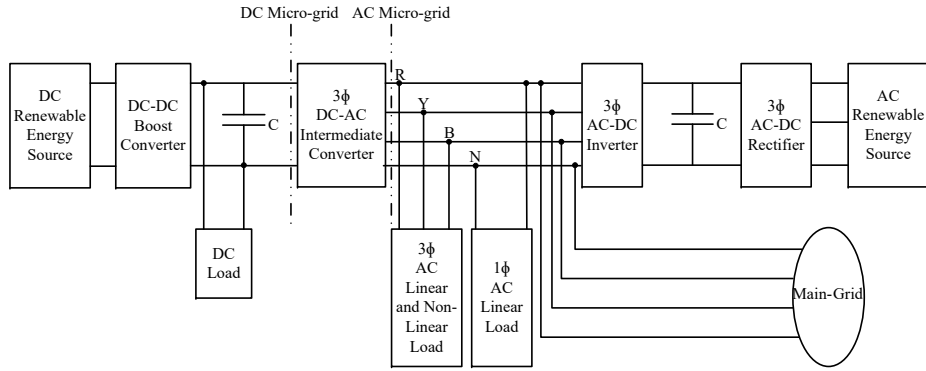


**Figure 1.3:** Block diagram of the proposed AC-DC coupled hybrid micro-grid system

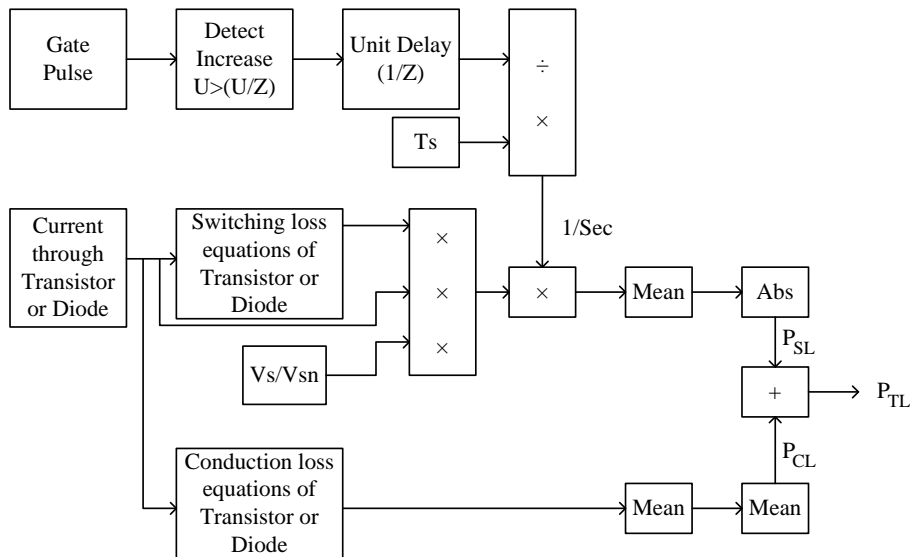


**Figure 1.4:** Block diagram of the conduction and switching loss of the proposed IGBT device

diagram for power conversion loss analysis by incorporating conduction and switching loss of the IGBT device. The grid-connected AC-DC coupled hybrid micro-grid system consists of the PV array and the DC load at the DC bus interlinks with the DFIG or PMSG variable wind and the AC linear and non-linear loads at the AC bus through the bi-directional converter (acting as inverter or rectifier). In the AC-DC

coupled hybrid micro-grid system, the power management control schemes are more complex than the individual AC or DC coupled hybrid micro-grid systems. Proper co-ordination control among the various converters is necessary to: (i) extract maximum power from the RES/DGs, (ii) minimize power transfer between the AC and DC networks, and (iii) to maintain stable operation of both the AC and DC networks. The advancement in power electronics and control technologies employed in the AC-DC coupled hybrid micro-grid system, which helps to build a smart power grid in the future.

## 1.2 Research Gaps

Based on the literature review, the following research gaps were observed:

- Firstly, the existing control methods of the AC coupled hybrid micro-grid system for power quality analysis have not examined the unbalanced distorted grid as well as unbalanced non-linear load scenarios. Also, the DC load fed by the AC-DC converter impacts on power quality. These issues have to be addressed by the development of appropriate control methods.
- Secondly, the SAPF based bi-directional power flow applications of the DC coupled hybrid micro-grid system have not discussed. The main advantage of this system is that there is no circulation of the reactive current and no need for synchronization of the DGs/RES in the network. Despite all these advantages, there has been almost no standardization for the DC system, particularly at a low voltage level. Also, this system requires a higher modification of the distribution network, which increases the cost drastically. Hence, the DC coupled hybrid micro-grid system has combined with the AC coupled hybrid micro-grid system through the BIC. The performance analysis of both systems has to be carried out for power flow control and power quality issues.
- Thirdly, the BIC of the AC-DC coupled hybrid micro-grid system has studied the bi-directional power flow control between the AC and DC bus; however, the power quality issues have not evaluated. In both the AC and DC coupled hybrid micro-grid systems, because of more power conversion stages, the internal losses are more, leading to lower efficiency. Hence, the design of an optimum scheme

with decreased losses has to be done, which eventually reduces the size of the set-up.

- Finally, the power conversion loss in the power converter stages in various configurations of the hybrid micro-grid systems have to be evaluated to arrive at the best configuration from operation and control perspectives.

## 1.3 Research Objectives

Based on the research gaps discussed in the previous section, the objectives of the research are as follows:

1. Development of control strategies for various topologies of the grid-connected AC, DC, and AC-DC coupled hybrid micro-grid system.
2. Performance analysis of power flow control with improved power quality for the AC coupled hybrid micro-grid system under various grid and load scenarios.
3. Performance analysis of power flow control with improved power quality for the DC coupled hybrid micro-grid system under various grid and load scenarios.
4. Performance analysis of power flow control with improved power quality for the AC-DC coupled hybrid micro-grid system under various grid and load scenarios.
5. Comparative analysis of power conversion losses in the AC-DC coupled hybrid micro-grid system over the AC and DC coupled hybrid micro-grid systems under various grid and load scenarios.

## 1.4 Thesis Outline

The thesis has been organized into six chapters as discussed below,

### 1.4.1 Organization of the Thesis

**Chapter 1:** The context and motivation of the thesis, along with the literature review is presented in this chapter. The research gaps, research objectives, and thesis outline have also discussed.

**Chapter 2:** At the level of the distribution system, the intermittent solar-wind RES and non-linear power electronic loads connected to the main-grid cause harmonics, which distorts its current. These issues can be effectively addressed by introducing SAPF applications. The performance of the conventional SAPF based instantaneous real and reactive power (p-q) load current control is analyzed and compared with the SAPF based proposed instantaneous real and reactive current (d-q) load current control. These controllers are validated using the MATLAB/Simulink for different case scenarios. It has been observed from the results that the conventional p-q control violates the limits on harmonics in case of unbalanced distorted grid and unbalanced non-linear load conditions.

The proposed d-q load current technique controls the harmonics within permissible limits under unbalanced distorted grid and unbalanced non-linear load conditions. The hybrid renewable energy system comprising of PV array, PMSG variable wind, and DFIG variable wind has modeled. The DC-DC boost converter is designed for conditioning the power generated by the wind and the PV RES.

The AC coupled hybrid micro-grid system comprises of PV and PMSG or DFIG variable wind RES integrated with the main-grid through the  $3\phi$  AC-DC-AC converter, DC-DC boosters, and the  $3\phi$  DC-AC UIC. The DC loads are connected at the AC grid side through the DC-DC booster and the  $3\phi$  AC-DC converters. The SAPF based UIC is controlled by the proposed fuzzy logic based d-q load current control. The hysteresis based current control (HBCC) is employed to compare the actual current with a reference current to drive the UIC. This provides a real and reactive power flow control with improved power quality at the AC grid side. The benefits of the proposed control technique over PI control have been illustrated.

The analysis of the AC coupled hybrid micro-grid system is performed for different case scenarios namely,

- (a) In the case of balanced undistorted grid and balanced non-linear load conditions, the simulations are carried out by considering that the load demands are more than the RES generations. Hence, the required deficit power is supplied by the

main-grid to meet the load demands.

- (b) In the case of unbalanced distorted grid and unbalanced non-linear load conditions, the simulations are carried out by considering that the load demands are less than the RES generations. Hence, surplus power is injected to the main-grid.

In both cases, the observed grid current total harmonic distortion (THD) has been reduced with the d-q load current control based fuzzy logic controller (FLC).

**Chapter 3:** In this chapter, the configuration of the DC coupled hybrid micro-grid system comprising of the PV and PMSG variable wind RES integrated with the main-grid has been analyzed. The AC linear/non-linear loads are connected at the AC side whereas, the DC load is connected at the DC side. The SAPF based BIC is controlled by the proposed d-q load current control based FLC. The HBCC is employed to compare the actual current with a reference current to drive the BIC. This provides a bi-directional power flow control between the AC and DC bus with improved power quality at the AC bus. The benefits of the proposed control technique over PI control have been illustrated.

The analysis of the DC coupled hybrid micro-grid system is performed for different case scenarios namely,

- (a) In this balanced undistorted grid and balanced non-linear load case, the simulation is carried out by considering the wind and the PV generating power more than the AC and DC load demands. Thus, the BIC acts as an inverter, and the grid receives surplus power.
- (b) In this unbalanced distorted grid and unbalanced non-linear load case, the simulation is carried out by considering the wind and the PV generating power less than the AC and DC load demands. Thus, the BIC acts as a rectifier, and the grid supplies the deficit power.

In both cases, the observed results of the grid current THD is reduced with d-q load current control based FLC.

**Chapter 4:** This chapter presents the AC-DC coupled hybrid micro-grid system with minimum power conversion stages. This system consists of the PV array and the PMSG or DFIG variable wind RES integrated with the main-grid through the  $3\phi$  AC-DC converter, DC-DC boosters, and the  $3\phi$  DC-AC BIC. The AC linear/non-linear loads are connected at the AC bus through the  $3\phi/1\phi$  AC-DC converters, whereas, the DC load is connected at the DC bus. The SAPF based BIC is controlled by the proposed d-q load current control based FLC. The HBCC is employed to compare the actual current with a reference current to drive the BIC. The benefits of the proposed control technique over PI control have been illustrated.

The analysis of the AC-DC coupled hybrid micro-grid system is performed for different case scenarios namely,

- (a) The simulation is carried out by considering that the AC and DC load demands are less than the wind and PV generation under balanced undistorted grid and balanced non-linear load conditions. Hence, the BIC operates in inverter mode and the main-grid receives surplus power.
- (b) The simulation is carried out by considering that the DC load demand is equal to the PV generation, and the AC load demands are met by wind generation under balanced undistorted grid and unbalanced non-linear load conditions. Hence, there is no action of the BIC as no power flows between the AC and DC bus links. The main-grid receives surplus power.
- (c) The simulation is carried out by considering that the AC and DC load demands are more than the wind and PV generation under unbalanced distorted grid and unbalanced non-linear load conditions. Thus, the BIC operates in rectifier mode, and the main-grid supply the deficit power.

In all the three cases, the observed results of the grid current THD has been reduced with d-q load current control based FLC.

**Chapter 5:** This chapter deals with the comparative power conversion loss analysis of the AC-DC coupled hybrid micro-grid system over the individual AC and DC coupled hybrid micro-grid systems. There are five converters employed for loss analysis in the AC coupled hybrid micro-grid such as, the two DC-DC boost converters,

$3\phi$  4-leg UIC,  $3\phi$  AC-DC-AC converter, and the  $3\phi$  AC-DC converter. There are four converters employed for loss analysis in the DC coupled hybrid micro-grid such as, the two DC-DC boost converters,  $3\phi$  4-leg BIC, and the  $3\phi$  AC-DC converter. There are three converters employed for loss analysis in the AC-DC coupled hybrid micro-grid such as, the DC-DC boost converter,  $3\phi$  4-leg BIC, and the  $3\phi$  AC-DC-AC converter. The power conversion loss analysis equations of the transistor and antiparallel diode are deduced from the curve fitting of the proposed IGBT device.

The power conversion loss analysis of the AC, DC, and the AC-DC coupled hybrid micro-grid system have been performed and compared using the MATLAB/Simulink block diagram given in Figure 1.4 in the previous section, for different case scenarios using appropriate parameters as below:

- (a) In the case of balanced undistorted grid and balanced non-linear load conditions, the simulation is carried out by considering that the RES power generations are less than the AC and DC load demands. The main-grid voltage is in phase with the main-grid current. Thus, the main-grid are supplying deficit power to meet the load demands.
- (b) In the case of unbalanced distorted grid and unbalanced non-linear load conditions, the simulation is carried out by considering that the RES generating power is more than the AC and DC load demands. The grid voltage is in phase opposition with the grid current. Thus, the main-grid receives surplus power from the RES.

In both cases, the observed results prove that the power conversion losses are reduced with the AC-DC coupled hybrid micro-grid system over the individual AC and DC coupled hybrid micro-grid systems.

**Chapter 6:** This chapter summarizes the conclusions drawn from the research work carried out. Further, the scope for future work is suggested.



# Chapter 2

## Performance Analysis of AC Coupled Hybrid Micro-grid System

### 2.1 Introduction

The most implemented hybrid micro-grid system around the world is the AC coupled. Due to its ease of operation in conjunction with the main-grid, the AC coupled hybrid micro-grid system is a more predominant structure. In this system, the intermittent hybrid RES or DGs are connected via individual UIC to the AC bus or CCP and main-grid. If any one of the UIC fails, the hybrid RES or DGs can still supply the required amount of power from the remaining sources (Justo et al., 2013). Therefore, this system is reliable but requires a complicated control algorithm for the individual UIC to regulate the real and reactive power. In addition, the non-linear loads at the AC bus or the CCP connected to the main-grid cause harmonics, which distorts its current. Also, many DC loads connected through the converters at the CCP cause even more harmonics in the grid current. These issues have to be addressed by the development of appropriate SAPF based control methods.

In this chapter, firstly, a suitable SAPF based proposed control is developed by comparing with the SAPF based conventional control through the simulation results. Secondly, the overall control of the AC coupled hybrid micro-grid system is discussed. Finally, the simulation results of the AC coupled hybrid micro-grid system are discussed through a comparative study.

## 2.2 Design and Implementation of Control System

The SAPF based conventional and proposed control strategies are compared and evaluated for their performance under different grid and load scenarios using a PI controller.

### 2.2.1 Conventional p-q Load Current Control

The p-q load current control is employed for the SAPF applications to regulate the real and reactive power as well as grid current harmonics (Raj and Rathi, 2015, Appala et al., 2013). Figure 2.1 shows the control diagram of the conventional p-q load current control. The grid voltages ( $V_{sa}$ ,  $V_{sb}$ , and  $V_{sc}$ ) and load currents ( $I_{la}$ ,  $I_{lb}$ , and  $I_{lc}$ ) are transformed from  $3\phi$  abc co-ordinates to the  $3\phi$   $\alpha\beta 0$  co-ordinates.

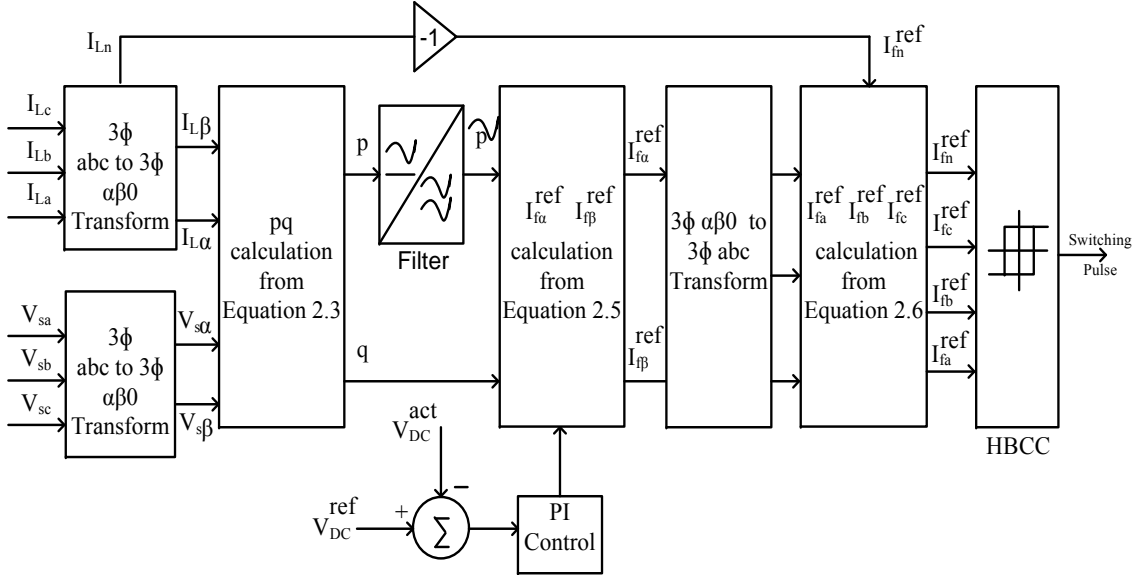


Figure 2.1: Conventional p-q load current control

The equations of  $V_{s\alpha}$ ,  $V_{s\beta}$ , and  $I_{l\alpha}$ ,  $I_{l\beta}$  are derived as:

$$\begin{bmatrix} V_{s\alpha} \\ V_{s\beta} \end{bmatrix} = \sqrt{\frac{2}{3}} \begin{bmatrix} 1 & -\frac{1}{2} & -\frac{1}{2} \\ 0 & \frac{\sqrt{3}}{2} & -\frac{\sqrt{3}}{2} \end{bmatrix} \begin{bmatrix} V_{sa} \\ V_{sb} \\ V_{sc} \end{bmatrix} \quad (2.1)$$

$$\begin{bmatrix} I_{l\alpha} \\ I_{l\beta} \end{bmatrix} = \sqrt{\frac{2}{3}} \begin{bmatrix} 1 & -\frac{1}{2} & -\frac{1}{2} \\ 0 & \frac{\sqrt{3}}{2} & -\frac{\sqrt{3}}{2} \end{bmatrix} \begin{bmatrix} I_{la} \\ I_{lb} \\ I_{lc} \end{bmatrix} \quad (2.2)$$

The instantaneous p-q equation can be written as:

$$\begin{bmatrix} p \\ q \end{bmatrix} = \begin{bmatrix} V_{s\alpha} & V_{s\beta} \\ V_{s\alpha} & -V_{s\beta} \end{bmatrix} \begin{bmatrix} I_{l\alpha} \\ I_{l\beta} \end{bmatrix} \quad (2.3)$$

With the help of the above equation (2.3), p-q can be resolved into both AC and DC values and is given by:

$$\begin{aligned} p &= \bar{p} + \tilde{p} \\ q &= \bar{q} + \tilde{q} \end{aligned} \quad (2.4)$$

The AC value of p and the entire (AC+DC) value of q must be supplied by SAPF. Hence, the reference filter currents equation in  $\alpha\beta$  co-ordinates are given by:

$$\begin{bmatrix} I_{f\alpha}^{ref} \\ I_{f\beta}^{ref} \end{bmatrix} = \begin{bmatrix} V_{s\alpha} & V_{s\beta} \\ V_{s\alpha} & -V_{s\beta} \end{bmatrix}^{-1} \begin{bmatrix} -\tilde{p} \\ -\bar{q} \end{bmatrix} \quad (2.5)$$

These filter currents are inversely transformed back to the  $3\phi$  abc co-ordinates. Thus, the generated reference filter currents are given by:

$$\begin{bmatrix} I_{fa}^{ref} \\ I_{fb}^{ref} \\ I_{fc}^{ref} \end{bmatrix} = \sqrt{\frac{2}{3}} \begin{bmatrix} 1 & 0 \\ -\frac{1}{2} & \frac{\sqrt{3}}{2} \\ -\frac{1}{2} & -\frac{\sqrt{3}}{2} \end{bmatrix} \begin{bmatrix} I_{f\alpha} \\ I_{f\beta} \end{bmatrix} \quad (2.6)$$

These reference filter currents  $I_{fa}^{ref}$ ,  $I_{fb}^{ref}$ , and  $I_{fc}^{ref}$  are compared with the measured filter currents  $I_{fa}$ ,  $I_{fb}$ , and  $I_{fc}$  to generate the switching pulses to the  $3\phi$  4-leg DC-AC interfacing converter using HBCC.

## 2.2.2 Proposed d-q Load Current Control

The proposed d-q load current control is employed for the SAPF applications to regulate the real and reactive power as well as the grid current harmonics. The control diagram of the proposed d-q load current control is shown in Figure 2.2.

The Butterworth low pass filter is used to eliminate the DC components in the load currents. The load currents are transformed from the  $3\phi$  abc frame to the  $3\phi$   $\alpha\beta 0$  and then, to the  $2\phi$  d-q synchronously revolving frame, which is considered as the DC quantities, and the compensating signals are derived. The angle  $\theta$  is determined from the  $\alpha\beta$  frame. The phasor representation of transformation of frames is shown in Figure 2.3. In the d-q frame, the d-axis current components are controlled by the PI controller, which maintains the constant voltage across the capacitor,  $C_{DC}$ .

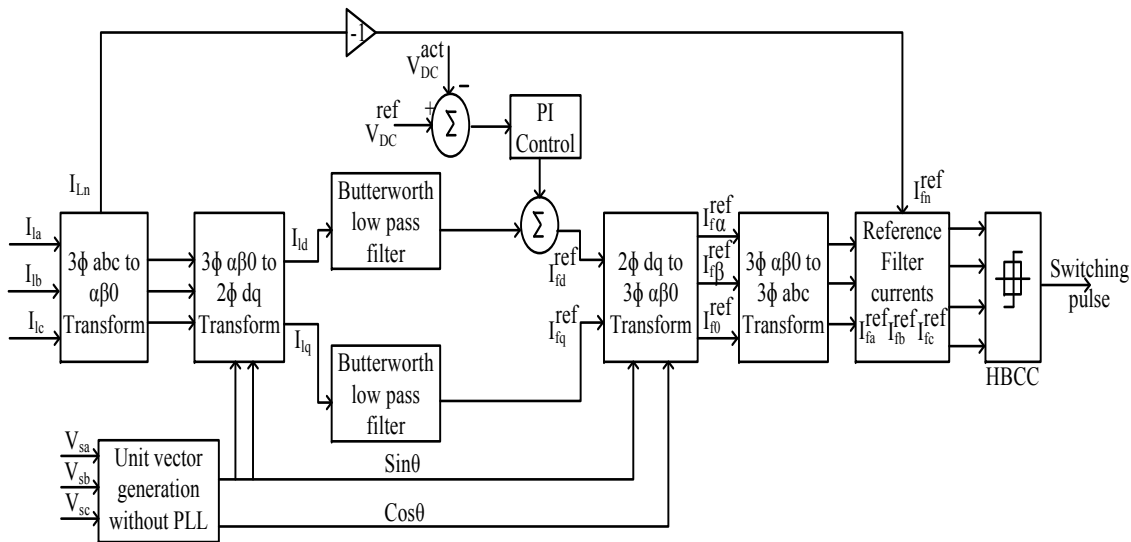


Figure 2.2: Proposed d-q load current control

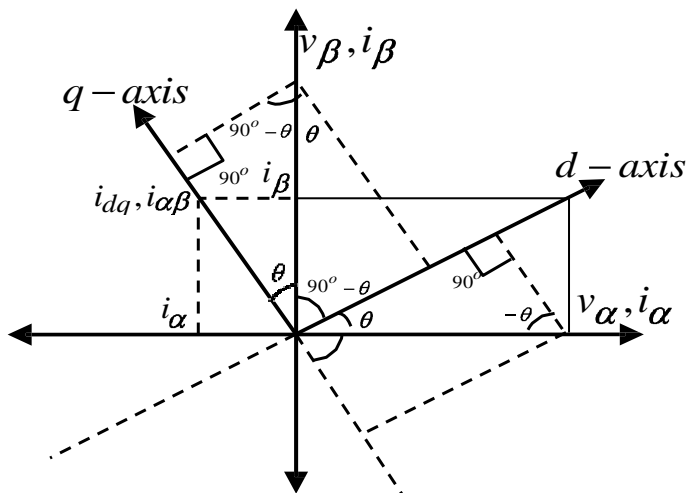


Figure 2.3: Phasor diagram of transformation of frames

The d-q load currents ( $I_{ld}$  and  $I_{lq}$ ) are derived as:

$$\begin{aligned} I_{ld} &= \cos \theta I_{l\alpha} + \sin \theta I_{l\beta} \\ I_{lq} &= -\sin \theta I_{l\alpha} + \cos \theta I_{l\beta} \end{aligned} \quad (2.7)$$

In the above equation (2.7), the currents contain the DC average value, and the AC oscillating value are given by:

$$\begin{aligned} I_{ld} &= \bar{I}_{ld} + \tilde{I}_{ld} \\ I_{lq} &= \bar{I}_{lq} + \tilde{I}_{lq} \end{aligned} \quad (2.8)$$

The reference currents are generated by transforming only the magnitude of the currents in the d-q frame, which are as follows:

$$\begin{aligned} I_{sd}^{ref} &= \bar{I}_{ld} \\ I_{sq}^{ref} &= I_{s0} = 0 \end{aligned} \quad (2.9)$$

The zero sequence current components remain unchanged when the d-axis is in the same direction as the voltage space vector. Hence,

$$\begin{aligned} I_{ld} &= \frac{1}{V_{\alpha\beta}} [V_{\alpha} I_{l\alpha} + V_{\beta} I_{l\beta}] \\ I_{lq} &= \frac{1}{V_{\alpha\beta}} [-V_{\beta} I_{l\alpha} + V_{\alpha} I_{l\beta}] \end{aligned} \quad (2.10)$$

Where,

$$P_{l\alpha\beta} = V_{\alpha} I_{l\alpha} + V_{\beta} I_{l\beta} \quad (2.11)$$

Hence, the equation of  $I_{ld}$  becomes:

$$I_{ld} = \frac{P_{l\alpha\beta}}{V_{\alpha\beta}} \quad (2.12)$$

The DC average value of above equation (2.12) is:

$$\bar{I}_{ld} = \left[ \frac{P_{l\alpha\beta}}{V_{\alpha\beta}} \right]_{DC} \quad (2.13)$$

At CCP, the reference supply current is in phase with the supply voltage, and multiplying the  $\bar{I}_{ld}$  with the unit vectors results in:

$$\begin{bmatrix} I_{f\alpha}^{ref} \\ I_{f\beta}^{ref} \\ I_{f0}^{ref} \end{bmatrix} = \begin{bmatrix} P_{l\alpha\beta} \\ V_{\alpha\beta} \end{bmatrix}_{DC} \frac{1}{V_{\alpha\beta}} \begin{bmatrix} V_{\alpha} \\ V_{\beta} \\ V_0 \end{bmatrix} \quad (2.14)$$

The above reference currents are transformed back to the  $3\phi$  abc frame. These currents  $I_{f\alpha}^{ref}$ ,  $I_{f\beta}^{ref}$ , and  $I_{f0}^{ref}$  are compared with measured filter currents  $I_{fa}$ ,  $I_{fb}$ , and  $I_{fc}$  to generate the switching pulses to the  $3\phi$  4-leg DC-AC interfacing converter using HBCC.

The advantage of the d-q load current control is that the angle  $\theta$  is computed directly from the grid voltage without PLL using the unit vector generation as shown in Figure 2.4. It is difficult to design a high-performance PLL-circuit in case of an unbalanced distorted grid voltage. The grid voltages ( $V_{sa}$ ,  $V_{sb}$ , and  $V_{sc}$ ) are trans-

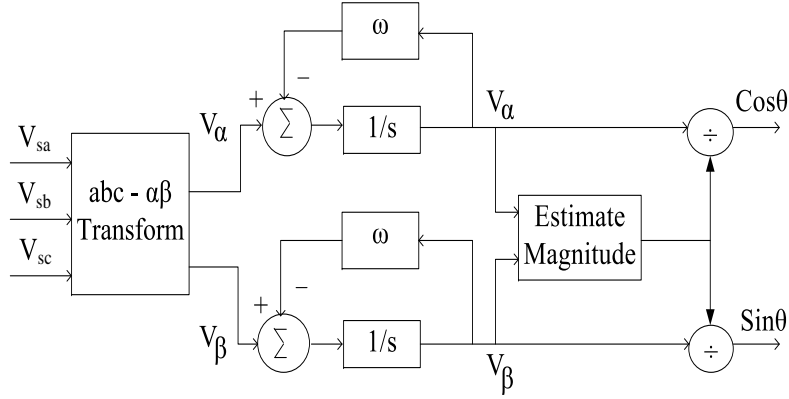


**Figure 2.4:** Unit vector generation without PLL

formed from the  $3\phi$  abc co-ordinates to the  $2\phi$   $\alpha\beta$  co-ordinates. The equations of  $V_{s\alpha}$  and  $V_{s\beta}$  are expressed as,

$$\begin{aligned} V_{s\alpha} &= 1.5V_m \sin \omega t \\ V_{s\beta} &= -1.5V_m \cos \omega t \end{aligned} \quad (2.15)$$

The  $\alpha\beta$  voltages are filtered using a digital low-pass filter with frequency  $\omega$  at first order. After filtering, the percentage of  $h^{th}$  order harmonics of the sensed supply

voltage decrease by a factor of  $\sqrt{\frac{2}{h^2-1}}$ . It eliminates supply harmonics, notches, and high-frequency noise. The estimated magnitude of the space vector is given by:

$$\vec{V} = \vec{V}_{\alpha\beta} = V_{s\alpha} + jV_{s\beta} = \sqrt{V_{s\alpha}^2 + V_{s\beta}^2} \quad (2.16)$$

It is evident from the above derived equation that unit vectors can be created by transforming the supply voltage into a  $\alpha\beta$  plane and dividing the  $\alpha\beta$  components by the space vector magnitude. Thus, the unit vector generation is described as:

$$\begin{aligned} \cos \theta &= \frac{V_{s\alpha}}{\sqrt{V_{s\alpha}^2 + V_{s\beta}^2}} = \frac{1.5V_m \sin \omega t}{1.5V_m} = \sin \omega t \\ \sin \theta &= \frac{V_{s\beta}}{\sqrt{V_{s\alpha}^2 + V_{s\beta}^2}} = -\frac{1.5V_m \cos \omega t}{1.5V_m} = -\cos \omega t \end{aligned} \quad (2.17)$$

### 2.2.3 Hysteresis Based Current Control

The HBCC technique has outstanding accuracy and fast response due to a quick change of load, and its control diagram as drawn in Figure 2.5. The reference filter neutral current,  $I_{fn}^{ref}$  of the 4th leg interfacing of the inverter is set to zero for neutral current compensation in case of unbalanced load condition. The following obtained filter current errors are given to the HBCC to generate the switching pulses (G1 to G8) for the  $3\phi$  DC-AC interfacing converter.

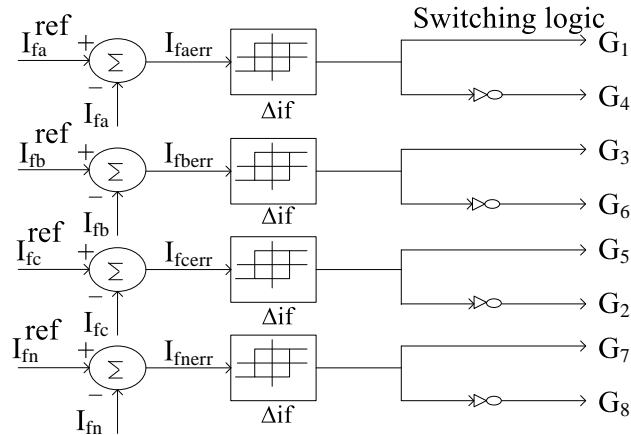


**Figure 2.5:** Hysteresis based current control

$$\begin{aligned}
I_{faerr} &= I_{fa}^{ref} - I_{fa} \\
I_{fberr} &= I_{fb}^{ref} - I_{fb} \\
I_{fcerr} &= I_{fc}^{ref} - I_{fc} \\
I_{fnerr} &= I_{fn}^{ref} - I_{fn}
\end{aligned} \tag{2.18}$$

If the current errors are above the upper bandwidth, then the upper switch of the corresponding phase leg is turned OFF, and if not, then the upper switch is turned ON and vice-versa.

## 2.2.4 Simulation Results for Proposed Controller Over the Conventional Controller

The MATLAB simulation is carried out without considering the RES for the schematic diagram shown in Figure 2.6. The performance of the proposed d-q load current control is compared with the conventional p-q load current control for different case studies. The simulation parameters of the main-grid and load are depicted in Table 2.1.

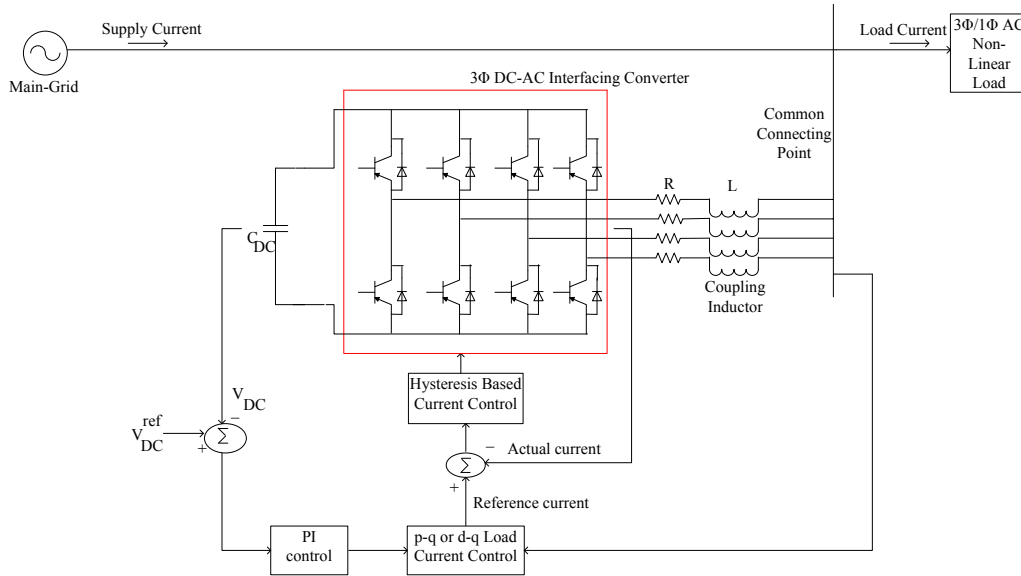


**Figure 2.6:** Schematic diagram of the p-q or d-q load current control



**Table 2.1:** Parameters of the main-grid and load

Parameters	Values
Supply voltage, $V_s$	400 V
Supply frequency, $f_s$	50 Hz
Source resistance, $R_s$	0.001 $\Omega$
Source inductance, $L_s$	0.01 mH
1-phase non-linear RL load	R = 20 $\Omega$ , L = 20 mH
3-phase non-linear RL load	R = 15 $\Omega$ , L = 60 mH
DC link capacitor voltage, $V_{DC}$	800 V
DC link capacitor, $C_{DC}$	3000 $\mu$ F
4-leg Inverter coupling inductor, L	5 mH
4-leg Inverter coupling resistance, R	0.001 $\Omega$

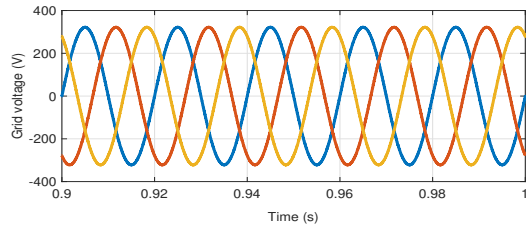
#### 2.2.4.1 Without RES – Balanced undistorted grid and balanced non-linear load conditions (BUGBNL)

When the supply voltages are balanced and sinusoidal, then both the control strategies converge to the same compensation characteristics. From Figure 2.7(i) and Figure 2.7(j), it can be observed that the grid current THD with p-q is 1.87% and the grid current THD with d-q is 0.64%. In this case, both the p-q and d-q load current control works well and are used to obtain the grid current THD within limits. Figures 2.7(a)- 2.7(h) represents the grid voltage, interfacing converter  $V_{DC}$ , grid current, and non-linear load current, respectively

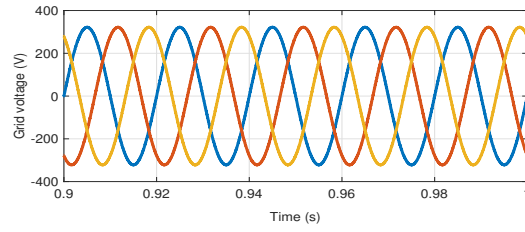
#### 2.2.4.2 Without RES – Unbalanced distorted grid and unbalanced non-linear load conditions (UDGUNL)

When the supply voltages are distorted and/or unbalanced sinusoidal, then both the control strategies result in different degrees of compensation in the harmonics. From Figure 2.8(i) and Figure 2.8(j), it can be observed that the grid current THD with p-q is 8.05% and the grid current THD with d-q is 1.34%. It is evident that the p-q control strategy is unable to yield an adequate solution when the source voltages are not ideal. On owing, the d-q method gives an outstanding performance under balanced, unbalanced, and non-sinusoidal supply conditions. Figures 2.8(a)- 2.8(h) represents the grid voltage, interfacing converter  $V_{DC}$ , grid current, and non-linear load current, respectively

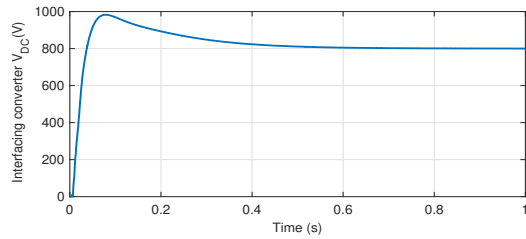
From both the cases 2.2.4.1 and 2.2.4.2, the proposed d-q load current control proves that it works quite well under unbalanced distorted grid voltage conditions. The results are tabulated in Table 2.2.



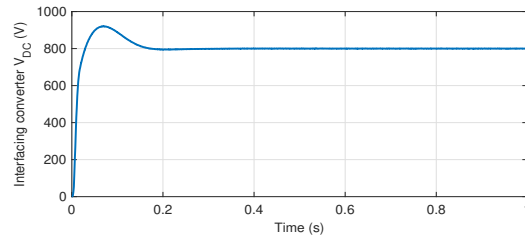
(a) Grid voltage - p-q



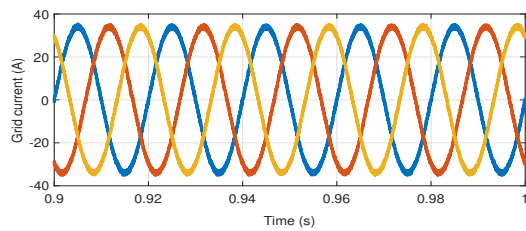
(b) Grid voltage - d-q



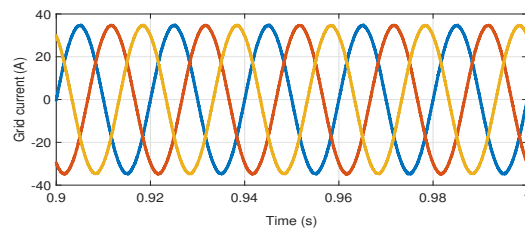
(c) Interfacing converter  $V_{DC}$  - p-q



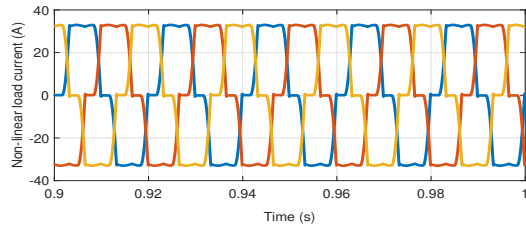
(d) Interfacing converter  $V_{DC}$  - d-q



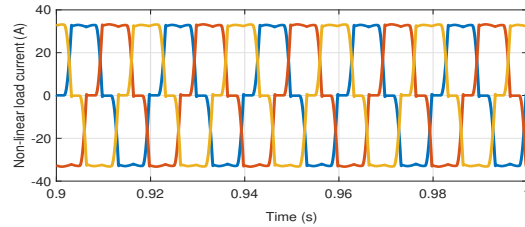
(e) Grid current - p-q



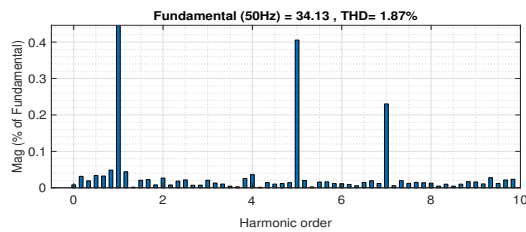
(f) Grid current - d-q



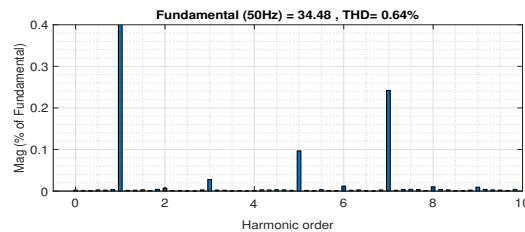
(g) Non-linear load current - p-q



(h) Non-linear load current - d-q

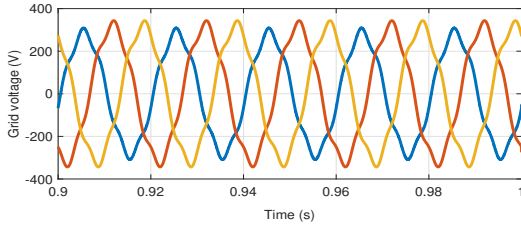


(i) Grid current THD - p-q

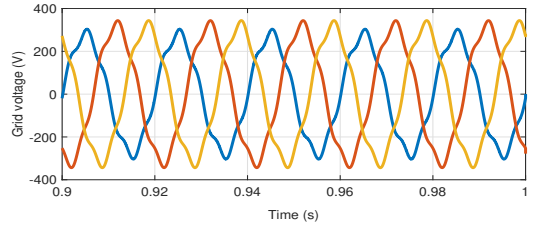


(j) Grid current THD - d-q

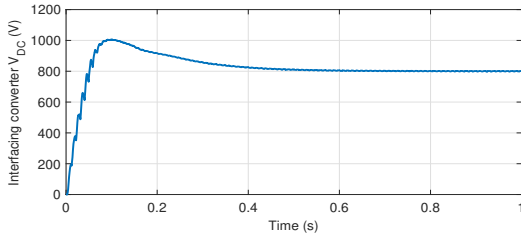
**Figure 2.7:** Comparison waveforms for p-q and d-q load current control under BUGBNL



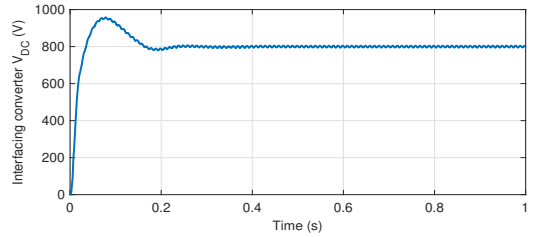
(a) Grid voltage - p-q



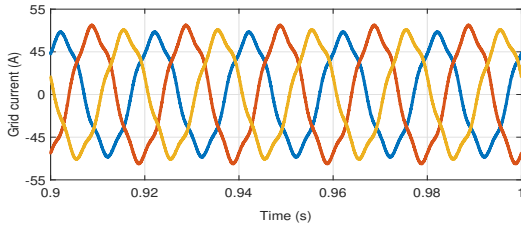
(b) Grid voltage - d-q



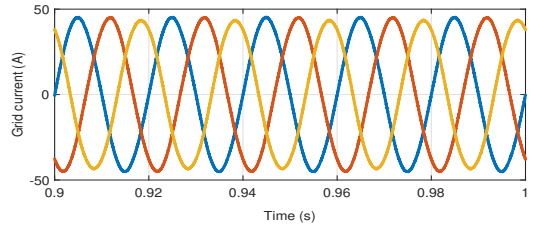
(c) Interfacing converter  $V_{DC}$  - p-q



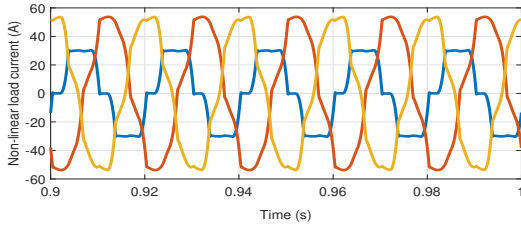
(d) Interfacing converter  $V_{DC}$  - d-q



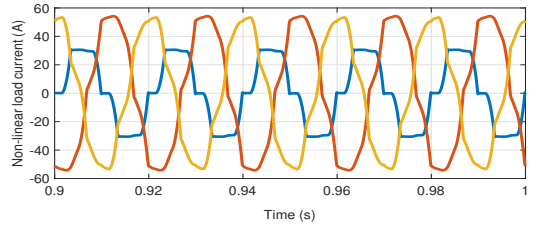
(e) Grid current - p-q



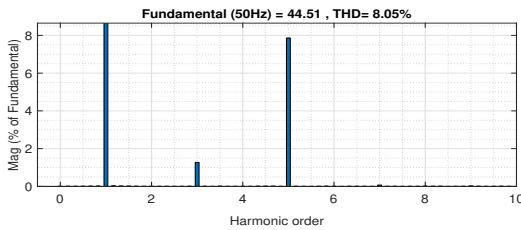
(f) Grid current - d-q



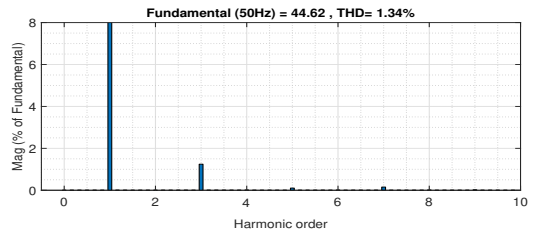
(g) Non-linear load current - p-q



(h) Non-linear load current - d-q



(i) Grid current THD - p-q



(j) Grid current THD - d-q

**Figure 2.8:** Comparison waveforms for p-q and d-q load current control under UDGUNL

**Table 2.2:** Performance of the grid current THD for proposed d-q load current control over the conventional p-q load current control

Case	Grid current THD with conventional p-q control	Grid current THD with proposed d-q control
a) Without RES under BUGBNL	1.87%	0.64%
b) Without RES under UDGUNL	8.05%	1.34%

## 2.3 Overall Control Diagram of the AC Coupled Hybrid Micro-grid System

The overall control diagram of the AC coupled hybrid micro-grid is shown in Figure 2.9. A PV array is connected to the DC sub-grid through the DC-DC boost converter, which inverts to the AC bus through the unidirectional  $3\phi$  DC-AC inverter, whereas PMSG or DFIG variable wind turbine is connected to AC bus through unidirectional  $3\phi$  AC-DC-AC back-to-back converter. The AC non-linear RL load and the DC resistive load through the AC-DC rectifier and the DC-DC boost converter are connected to the AC bus integrated with the main-grid. The  $3\phi$  DC-AC UIC has controlled the power flow transfer with harmonics current limits as per the IEEE 519 standards at the AC bus.

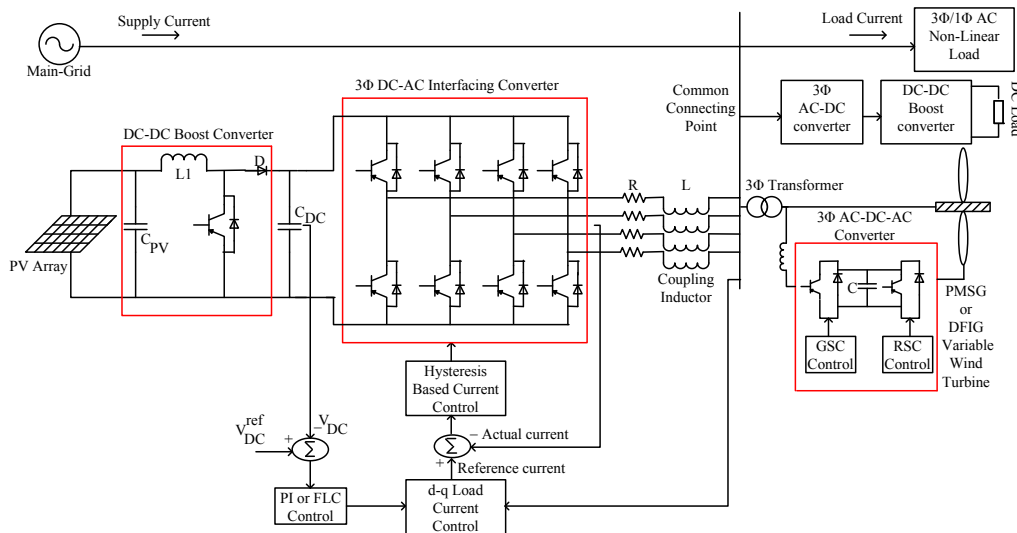


**Figure 2.9:** Overall control diagram of the AC CHM

### 2.3.1 PV Array Model

The relation between the output voltage and the current of a PV array is given below, and its simulation parameters are tabulated in Table 2.3 (Villalva et al., 2009).

**Table 2.3:** Parameters of the PV array model

Parameters	Values
Open circuit voltage, $V_{oc}$	42.1 V
Short circuit current, $I_{sc}$	3.87 A
No. of series cell, $N_s$ -cell	72
No. of parallel string panels, $N_{pp}$	20
No. of series string panels, $N_{ss}$	20
Quantum of charge, $q$	$1.602 \times 10^{-19}$ C
Diode ideality factor, $A$	1.3997
Stefan Boltzmann constant, $K_B$	$1.38 \times 10^{-23}$ J/K
Voltage temperature coefficient, $\beta_{oc}$	-0.1230 V/K
Current temperature coefficient, $\alpha_{sc}$	$3.2 \times 10^{-3}$ A/K
Actual temperature, $T_{act}$	298.15 K
Reference temperature, $T_{ref}$	298.15

$$I_m = N_{pp} \left( I_{pv} - I_0 \left[ \exp \left( \frac{V + R_s \left( \frac{N_{ss}}{N_{pp}} \right) I}{V_{th} A N_{ss}} \right) - 1 \right] \right) \quad (2.19)$$

Where the photocurrent,  $I_{pv}$  is induced by the incidence irradiation on the solar cell and is given by:

$$I_{pv} = (I_{pv_n} + \alpha_{sc} \Delta T) \frac{G}{G_{ref}} \quad (2.20)$$

The change in actual and reference temperature,  $\Delta T$  is expressed as:

$$\Delta T = (T_{act} - T_{ref}) \quad (2.21)$$

The light generated current,  $I_{pv_n}$  at actual condition is:

$$I_{pv_n} = (R_{sh} + R_s) \frac{I_{sc_n}}{R_{sh}} \quad (2.22)$$

The diode thermal voltage,  $V_{th}$  is given by:

$$V_{th} = \frac{K_B T_{act} N_{s-cell}}{q} \quad (2.23)$$

The diode reverse saturation current,  $I_0$  is given by the equation:

$$I_0 = \frac{I_{sc} + \alpha_{sc}\Delta T}{\exp\left(\frac{V_{0c_n} + \beta_{0c}}{AV_{th}}\right) - 1} \quad (2.24)$$

### 2.3.2 PMSG Variable Wind Turbine Model

The modeling parameters for variable speed PMSG wind are tabulated in Table 2.4 (Jayalakshmi et al., 2012).

**Table 2.4:** Parameters of the PMSG variable wind turbine model

Parameters	Values
Rated voltage, $V_{nom}$	400 V
Rated frequency, F	50 Hz
Rated power, $P_{nom}$	50 kW
Stator phase resistance, $R_s$	2.875 $\Omega$
d & q-axis phase inductance	8.5 mH
Torque constant	12 N-m/A peak
Inertia	$0.8 \times 10^{-03}$ kg-m <sup>2</sup>
No. of pole pairs	8
Rated DC link voltage of AC-DC-AC converter, $V_{DC}$	1050 V

The aerodynamic power obtained from a wind turbine depends on the wind speed and is expressed by:

$$P_m = 0.5\rho V_w^3 A C_p(\lambda, \beta) \quad (2.25)$$

The power coefficient,  $C_p(\alpha, \beta)$  decides the total power available from wind and is given by:

$$C_p(\alpha, \beta) = 0.5176 \left( \frac{116}{\lambda_i} - 0.4\beta - 5 \right) \exp\left(\frac{-21}{\lambda_i}\right) \quad (2.26)$$

Tip speed ratio:

$$\lambda = \frac{\omega_m R}{V_w} \quad (2.27)$$

$$\lambda_i = \left[ \frac{1}{\lambda + 0.08\beta} - \frac{0.035}{\beta^3 + 1} \right]^{-1} \quad (2.28)$$

Blade pitch angle:

$$\beta = \frac{1}{\left[ \frac{1}{\lambda + 0.08\theta} - \frac{0.035}{\theta^3 + 1} \right]} \quad (2.29)$$

The function of  $\beta$  is to control the input mechanical power of the wind turbine generator at high wind speed.

The PMSG model in the d-q frame is given by:

$$\frac{di_{ds}}{dt} = \frac{1}{L_d} \left[ -V_{ds} - R_s i_{ds} + \omega L_q i_{qs} \right] \quad (2.30)$$

$$\frac{di_{qs}}{dt} = \frac{1}{L_q} \left[ -V_{qs} - R_s i_{qs} - \omega L_d i_{ds} + \omega \phi_m \right] \quad (2.31)$$

If the rotor is cylindrical  $L_d = L_q = L_s$ , the electromagnetic torque is:

$$T_e = 1.5 P \phi_m i_{qs} \quad (2.32)$$

### 2.3.3 DFIG Variable Wind Turbine Model

The maximum power,  $P_{max}$  obtained from a wind turbine is given below, and its simulation parameters are tabulated in Table 2.5 (Liu et al., 2011).

**Table 2.5:** Parameters of the DFIG variable wind turbine model

Parameters	Values
Rated voltage, $V_{nom}$	400 V
Rated frequency, F	50 Hz
Rated power, $P_{nom}$	50 kW
Rated mechanical power, $P_m$	45 kW
Stator resistance, $R_s$	0.00706 pu
Rotor resistance, $R_r$ (referred to the stator)	0.005 pu
Stator inductance, $L_s$	0.171 pu
Rotor inductance, $L_r$ (referred to the stator)	0.156 pu
Mutual inductance, $L_m$	0.156 pu
Lumped inertia constant, J	3.1 s
No. of pole pairs, $N_p$	6
Rated DC link voltage of AC-DC-AC converter, $V_{DC_{nom}}$	800 V

$$P_{max} = \frac{1}{2} \rho \pi R^2 V^3 C_{p,max} \quad (2.33)$$

The voltage equations of an induction motor in a d-q rotating frame are:

$$\begin{aligned}
V_{ds} &= -R_s I_{ds} + P \lambda_{ds} - \omega_1 \lambda_{qs} \\
V_{qs} &= -R_s I_{qs} + P \lambda_{qs} + \omega_1 \lambda_{ds} \\
V_{dr} &= R_r I_{dr} + P \lambda_{dr} - \omega_2 \lambda_{qr} \\
V_{qr} &= R_r I_{qr} + P \lambda_{qr} + \omega_2 \lambda_{dr}
\end{aligned} \tag{2.34}$$

Where,

$$\begin{aligned}
\lambda_{ds} &= -L_s I_{ds} \\
\lambda_{qs} &= -L_s I_{qs} \\
\lambda_{dr} &= L_r I_{dr} \\
\lambda_{qr} &= L_r I_{qr}
\end{aligned} \tag{2.35}$$

The DFIG dynamic equations are as follows:

$$\frac{J}{N_p} \frac{d\omega_r}{dt} = T_m - T_{em} \tag{2.36}$$

$$T_{em} = N_p L_m (I_{qs} I_{dr} - I_{ds} I_{qr}) \tag{2.37}$$

$$\omega_2 = \omega_1 - \omega_r \tag{2.38}$$

$$\lambda_{ds} = 0; \lambda_{qs} = \lambda_s \tag{2.39}$$

From the equations (2.35) and (2.39), the equation (2.37) becomes:

$$T_{em} = -N_p \frac{L_m}{L_s} \lambda_s I_{dr} \tag{2.40}$$

Substituting equations (2.38) and (2.39) in the equation (2.34) to obtain the stator voltage oriented reference frame equations as:

$$\begin{aligned}
V_{dr} &= R_r I_{dr} + \sigma L_r \frac{dI_{dr}}{dt} - (\omega_1 - \omega_r)(L_m I_{qs} + L_r I_{qr}) \\
V_{qr} &= R_r I_{qr} + \sigma L_r \frac{dI_{qr}}{dt} + (\omega_1 - \omega_r)(L_m I_{ds} + L_r I_{dr})
\end{aligned} \tag{2.41}$$



Where,

$$\sigma = -\frac{L_s L_r - L_m^2}{L_s L_r} \quad (2.42)$$

### 2.3.4 DC Link Voltage Control of the Interfacing Converter

To regulate and maintain a constant voltage of the DC link capacitor, it is necessary to control the real power flowing into the loads through the  $3\phi$  4-leg DC-AC UIC. The selection of the DC-link voltage value,  $V_{DC}$  is always higher than the grid voltage peak value,  $V_s$ . The maximum value of the DC link voltage,  $V_{DC_{max}}$  (Biricik et al., 2016) is given by:

$$V_{DC_{max}} = 1.5\sqrt{2}V_s \quad (2.43)$$

$$\sqrt{2}V_s < V_{DC} < (1.5\sqrt{2}V_s) \quad (2.44)$$

#### 2.3.4.1 PI Controller

Firstly, the voltage is sensed across the DC link and compared with a DC link voltage reference value. Secondly, the error between the reference and the actual value is processed through the PI controller and then fed to the reference current generation. The following equations give the selection of the  $K_p$  and  $K_i$  values:

$$K_p = 2C_{DC}\omega\xi \quad (2.45)$$

$$K_i = C_{DC}\omega^2 \quad (2.46)$$

Where,  $\omega$  is supply frequency and  $C_{DC}$  is the DC link capacitor, and its value is selected by the following equation,

$$C_{DC} \geq \frac{S}{2V_{DC}\omega\Delta V_{DC}} \quad (2.47)$$

where,  $s$  is the rating capacity of the interfacing converter and  $\Delta V_{DC}$  is a ripple of the peak-to-peak DC link voltage.

The generation of real power and variations in load is highly dynamic due to the intermittency of hybrid PV/wind RES. In order to have a stable operating condition, the PI-based DC link voltage control can be calibrated for a certain stable-state range. Nevertheless, they cannot guarantee stability to a wide variety of dynamic conditions.

### 2.3.4.2 Fuzzy logic Controller

The intelligent controller, like FLC-based DC link voltage, is designed with equilateral triangular membership function (ETMF) to optimize the voltage error efficiently and gives the best results regarding current harmonic filtering. Figure 2.10 represents a process involved in DC link voltage regulation using FLC. It mainly comprises of three blocks, which are fuzzification using ‘continuous universe of discourse’, inference system based on fuzzy implication using ‘Mamdani’s operator’, and de-fuzzification using ‘centre of gravity method’.

The development of an FLC-based DC link voltage algorithm with two inputs and one output having ‘seven fuzzy sets’ comprises of 49 linguistic variables. The input DC link voltage error ‘e’ and the change in DC link voltage error ‘ce’ are given as input variables to the FLC, as shown in Figure 2.11(a) and Figure 2.11(b). The output variable of the FLC is the current signal, which is required for the current control, as shown in Figure 2.11(c). The fuzzy rule mechanism is shown in Table 2.6 (Ouchen et al., 2016).

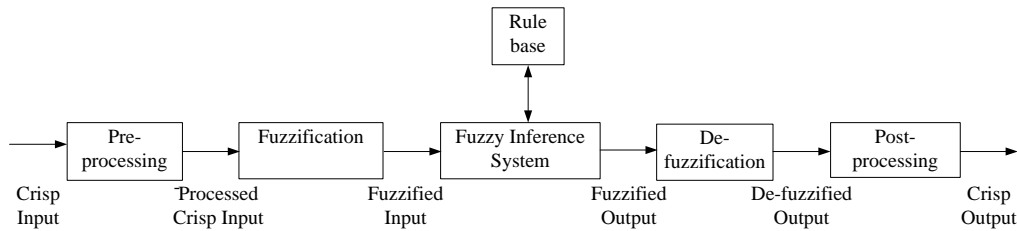


**Figure 2.10:** DC voltage regulation using FLC

**Table 2.6:** Fuzzy rule mechanism

e ce	NL	NM	NS	Z	PS	PM	PL
NL	NL	NL	NL	NL	NM	NS	Z
NM	NL	NL	NL	NM	NS	Z	PS
NS	NL	NL	NM	NS	Z	PS	PM
Z	NL	NM	NS	Z	PS	PM	PL
PS	NM	NS	Z	PS	PM	PL	PL
PM	NS	Z	PS	PM	PL	PL	PL
PL	Z	PS	PM	PL	PL	PL	PL

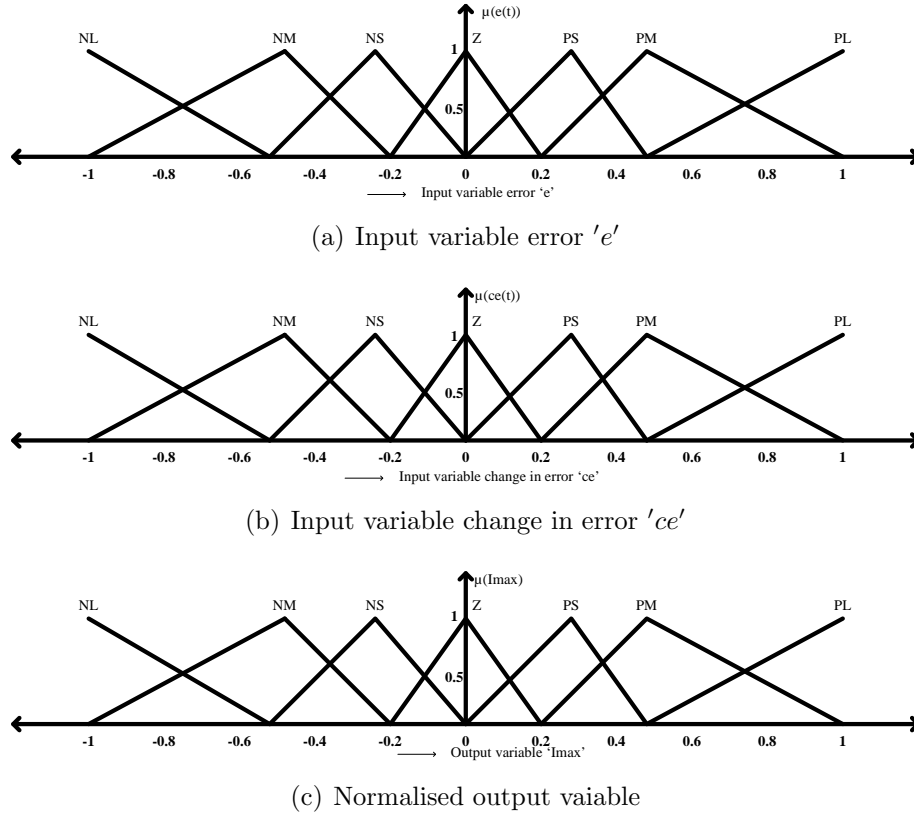


**Figure 2.11:** Input and output variables of the ETMF

### 2.3.5 DC-DC Boost Converter

As the PV array produces variable DC power output, the variable DC output voltage must be converted to constant using the DC-DC boost converter at the DC bus. At the AC bus, the  $3\phi$  AC voltage is converted to DC voltage through an uncontrolled rectifier. This DC voltage maintains an appropriate constant voltage using the DC-DC boost converter to supply the DC resistive load. The design equations for the boost converter (Krithiga and Gounden, 2014) are shown below:

$$L_b = \frac{V_i D}{2\Delta I_i f_{sw}} \quad (2.48)$$

$$C_b = \frac{I_0 D^2}{(\Delta V_0 / V_0)(1 - D)V_0 f_{sw}} \quad (2.49)$$

Where,  $V_i$  and  $I_i$  are the output voltage and current from the PV array.  $I_i$  is the input current ripple of the boost converter,  $V_0$  and  $I_0$  are the output voltage and current

of the boost converter respectively,  $f_{sw}$  is the switching frequency, and  $D$  is the duty ratio of the boost converter switch.

$$D = 1 - \left( \frac{V_i}{V_0} \right) \quad (2.50)$$

### 2.3.6 Coupling Inductive Filter of the Interfacing Converter

The filter inductance can be calculated using equation (2.51), where 'h' is the hysteresis band, usually taken as 5% of the compensation current,  $f_{sw_{max}}$  is the maximum switching frequency, and  $V_{DC}$  is the DC-link voltage.

$$L_f = \frac{V_{DC}}{6hf_{sw_{max}}} \quad (2.51)$$

## 2.4 Simulation Results for AC CHM System

The MATLAB simulation is carried out for the AC coupled hybrid micro-grid system as shown in Figure 2.9. The performance of the proposed d-q load current technique based PI and FLC is analyzed and validated for different grid and load case studies with a variation of the RES. The simulation parameters of the UIC, DC-DC boost converter, and the main-grid are tabulated in Table 2.7.

**Table 2.7:** Parameters of the UIC, DC-DC boost converter, and main-grid

Parameters	Values
Main-grid supply voltage, $V_s$	400 V
Main-grid supply frequency, $f$	50 Hz
UIC power rating, $P_{conv}$	100 kVA
PV array capacitor, $C_{pv}$	110 $\mu$ F
Boost converter inductor, $L_1$	7.45 mH
Boost converter switching frequency, $f_{sw}$	20 kHz
DC link capacitor, $C_{DC}$	7000 $\mu$ F
DC link capacitor voltage, $V_{DC}$	800 V
UIC coupling inductor, $L$	5 mH
UIC coupling resistance, $R$	0.001 $\Omega$

## 2.4.1 AC CHM (PMSG+PV) – Balanced undistorted grid and balanced non-linear load conditions

The  $P_{acnon-linearload}$  of 17 kW and  $P_{dload}$  of 40 kW demands are more than the  $P_{pv}$  generation of 3 kW at irradiation of  $100 \text{ W/m}^2$  and  $P_{wind}$  generation of 30 kW at wind speed of 7 m/s as shown in Figures 2.12(a)–2.12(d) . Hence, the required deficit power of 24 kW is supplied by the  $P_{grid}$  to meet the load demands as shown in Figure 2.12(e). In order to supply power to the  $P_{dload}$  and  $P_{acnon-linearload}$ , both the UICs should operate in the inverter mode as shown in Figure 2.12(f).

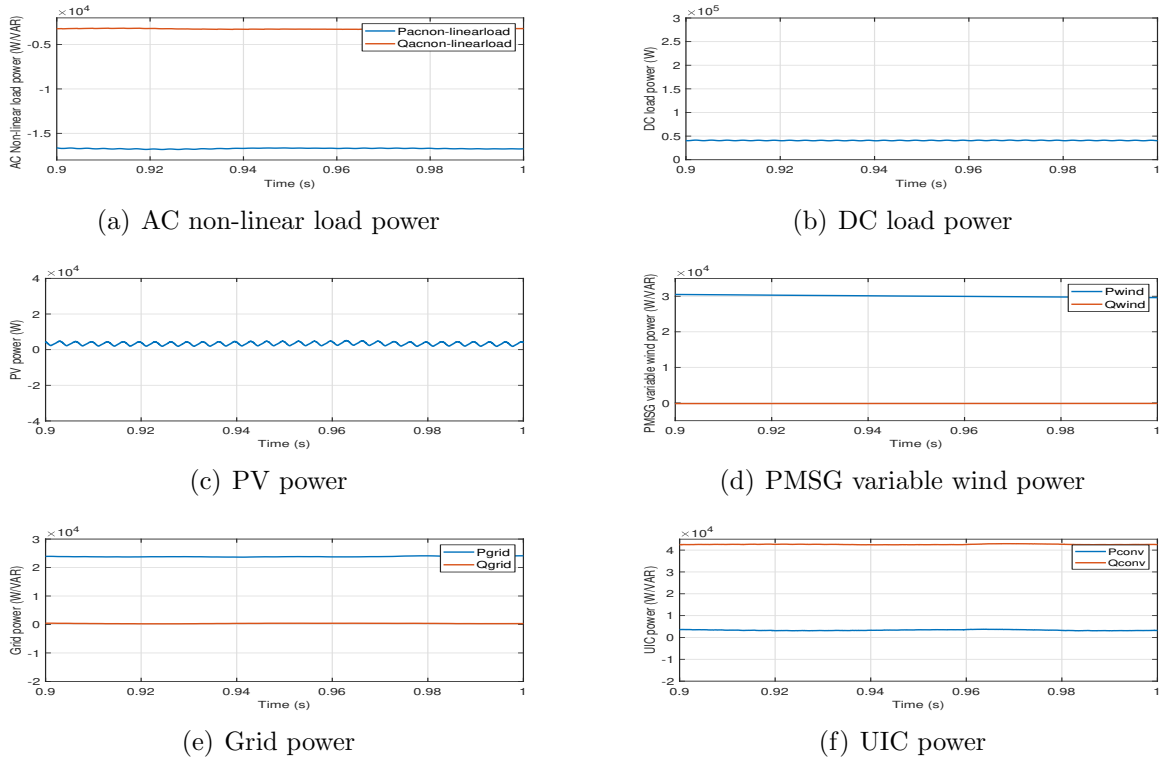
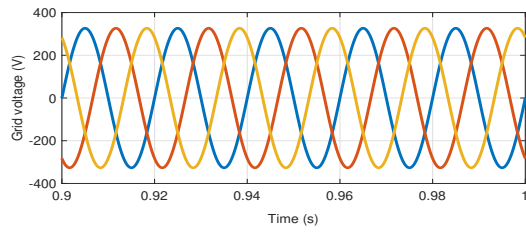
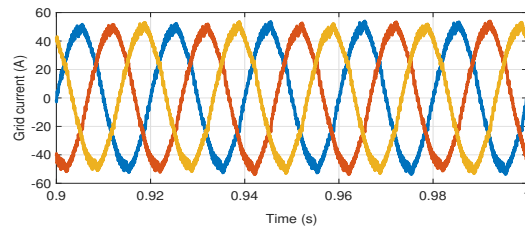


**Figure 2.12:** Power flow analysis of AC CHM with PMSG+PV under BUGBNL

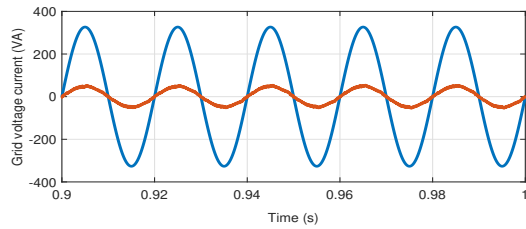
Figures 2.13(a)–2.13(g) represents the grid voltage, grid current, grid voltage current, grid power factor, UIC DC link voltage, filter current, and non-linear load current, respectively. From Figure 2.13(h), it can be observed that the grid current THD before compensation is 19.54%. After compensation, the grid current THD improved with the FLC over the PI. It is evident from Figure 2.13(i) and Figure 2.13(j) that the grid current THD is 4.68% with PI and 2.87% with FLC, which is well within the IEEE standard limits.



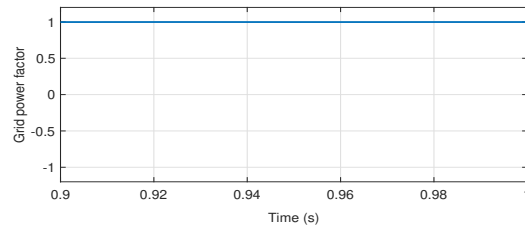
(a) Grid voltage



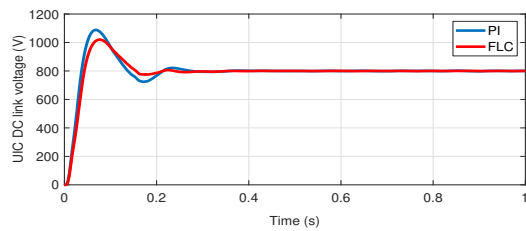
(b) Grid current



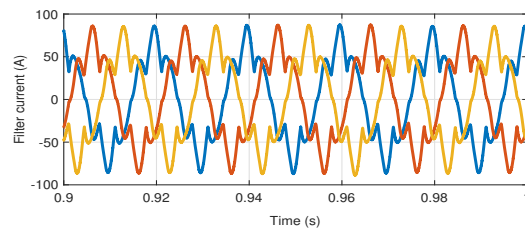
(c) Grid voltage current



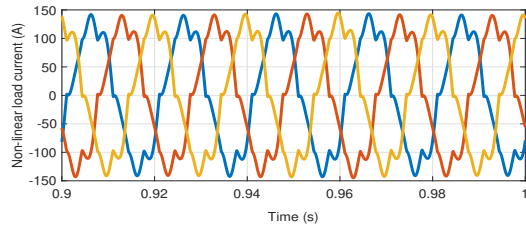
(d) Grid power factor



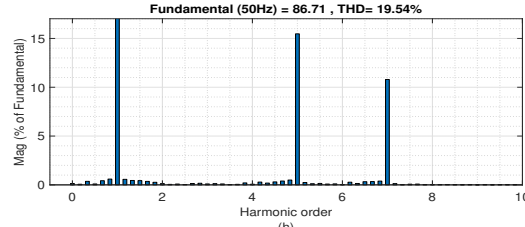
(e) UIC DC link voltage



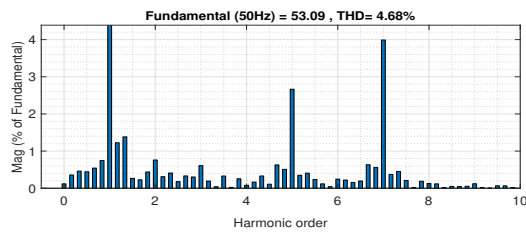
(f) Filter current



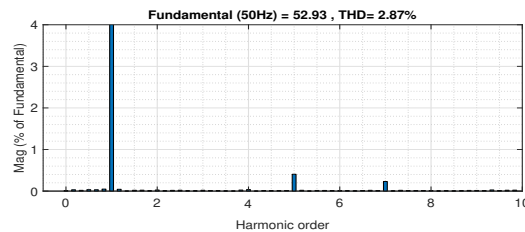
(g) Non-linear load current



(h) Grid current THD before filtering



(i) Grid current THD after filtering - PI



(j) Grid current THD after filtering - FLC

**Figure 2.13:** Harmonic analysis of AC CHM with PMSG+PV under BUGBNL

## 2.4.2 AC CHM (PMSG+PV) – Unbalanced distorted grid and unbalanced non-linear load conditions

The  $P_{acnon-linearload}$  of 14 kW and  $P_{dcload}$  of 20 kW demands are less than the  $P_{wind}$  generation of 34 kW at wind speed of 8 m/s and the  $P_{pv}$  generation of 24 kW at irradiation of 600 W/m<sup>2</sup> as shown in Figures 2.14(a)–2.14(d). Hence, the surplus power of 24 kW of both the  $P_{pv}$  and  $P_{wind}$  is injected into the  $P_{grid}$  as shown in Figure 2.14(e). In order to inject the surplus power to the  $P_{grid}$ , both the UICs should operate in the inverter mode as shown in Figure 2.14(f).

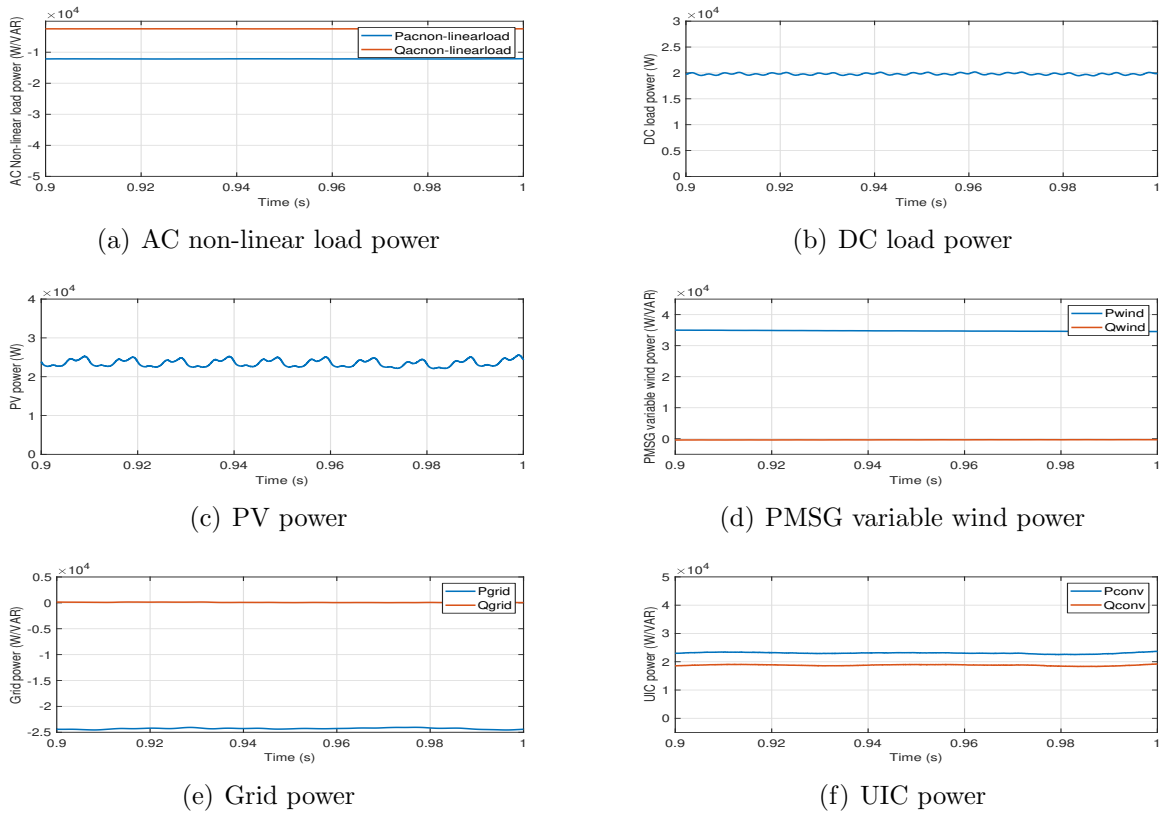
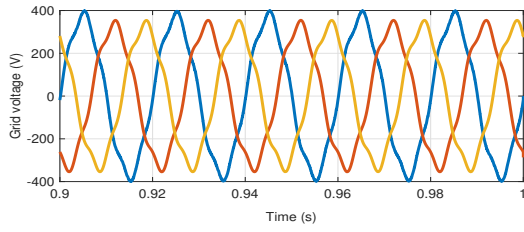
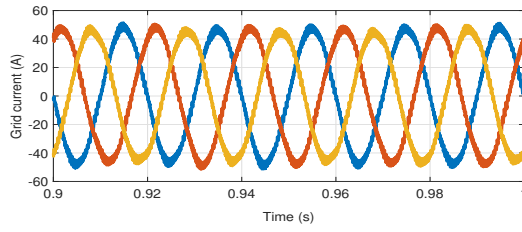


**Figure 2.14:** Power flow analysis of AC CHM with PMSG+PV under UDGUNL

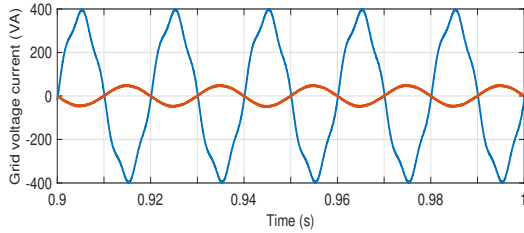
Figures 2.15(a)–2.15(g) represents the grid voltage, grid current, grid voltage current, grid power factor, UIC DC link voltage, filter current, and nonlinear load current, respectively. In Figure 2.15(h), the observation of the grid current THD before compensation is 46.22%. After compensation, the grid current THD improved with the FLC (2.34%) over the PI (4.41%) as shown in Figure 2.15(i) and Figure 2.15(j), respectively. The obtained grid current THD values are within the harmonic limits.



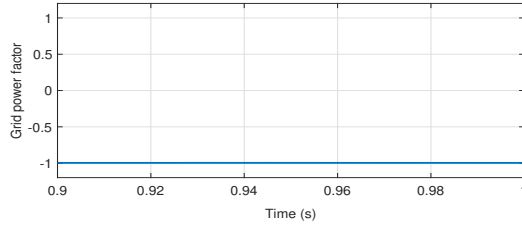
(a) Grid voltage



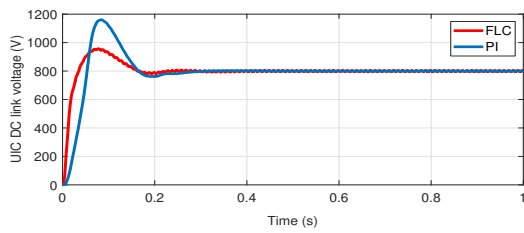
(b) Grid current



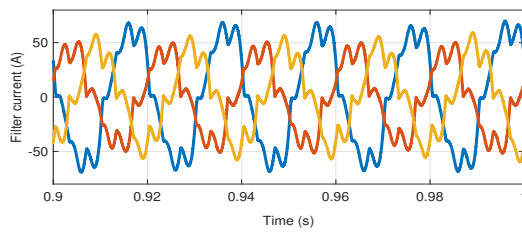
(c) Grid voltage current



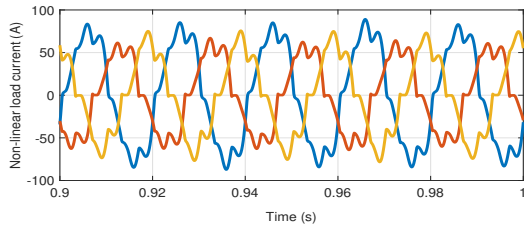
(d) Grid power factor



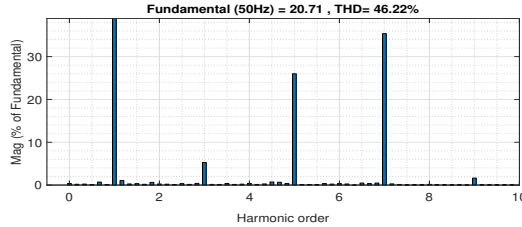
(e) UIC DC link voltage



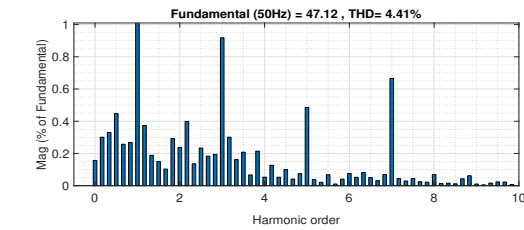
(f) Filter current



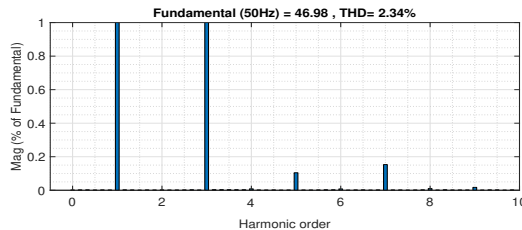
(g) Non-linear load current



(h) Grid current THD before filtering



(i) Grid current THD after filtering - PI



(j) Grid current THD after filtering - FLC

**Figure 2.15:** Harmonic analysis of AC CHM with PMSG+PV under UDGUNL



### 2.4.3 AC CHM (DFIG+PV) – Balanced undistorted grid and balanced non-linear load conditions

The  $P_{dload}$  of 25 kW,  $P_{aclinearload}$  of 25 kW, and  $P_{acnon-linearload}$  of 15 kW demands are more than the  $P_{pv}$  generation of 3 kW at irradiation of 100 W/m<sup>2</sup> and the  $P_{wind}$  generation of 30 kW at wind speed of 7 m/s as shown in Figures 2.16(a)–2.16(d). Hence, the  $P_{grid}$  supplies the remaining deficit power of 32 kW to both the AC-DC linear and non-linear loads as shown in Figure 2.16(e). In order to supply power to both the  $P_{dload}$  and  $P_{acnon-linearload}$ , both the UICs should operate in the inverter mode as shown in Figure 2.16(f).

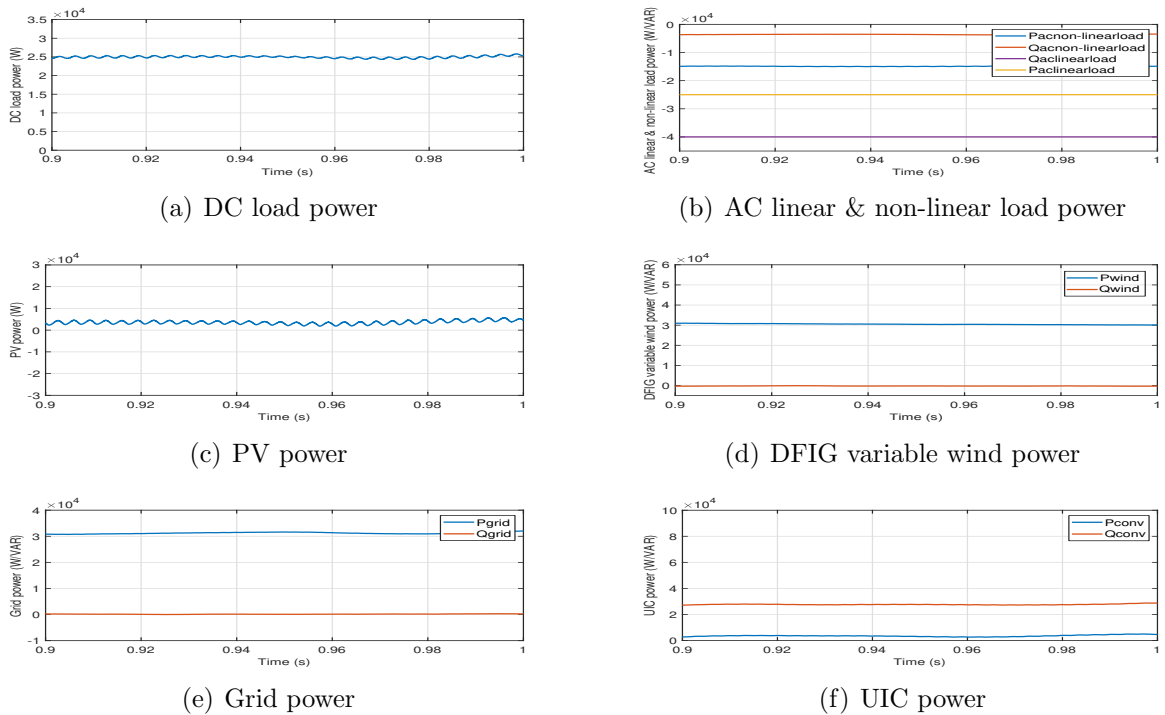
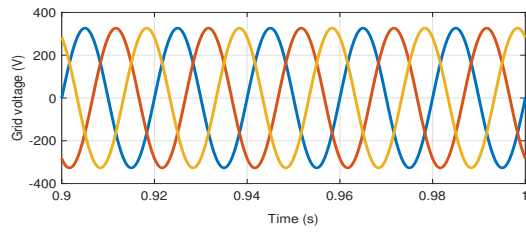
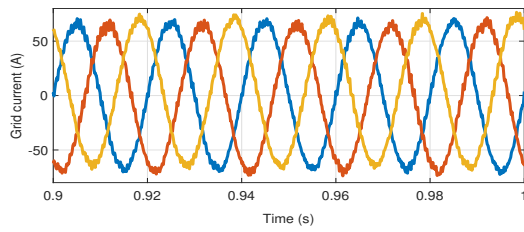


**Figure 2.16:** Power flow analysis of AC CHM with DFIG+PV under BUGBNL

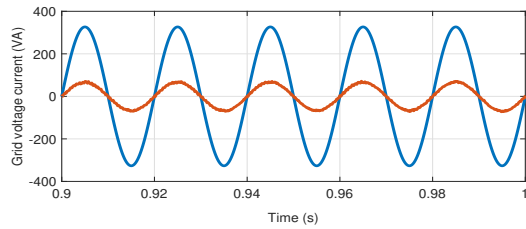
Figures 2.17(a)–2.17(g) shows the grid voltage, grid current, grid voltage current, grid power factor, UIC DC link voltage, filter current, and nonlinear load current, respectively. From Figure 2.17(h), it can be observed that the grid current THD before compensation is 21.49%. After compensation, the grid current THD improved with the FLC over the PI. It is evident from Figure 2.17(i) and Figure 2.17(j) that the grid current THD is 4.92% with PI and 2.78% with FLC, which is well within the IEEE standard limits.



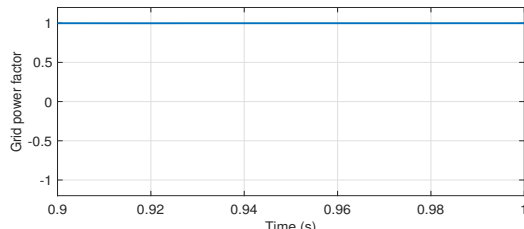
(a) Grid voltage



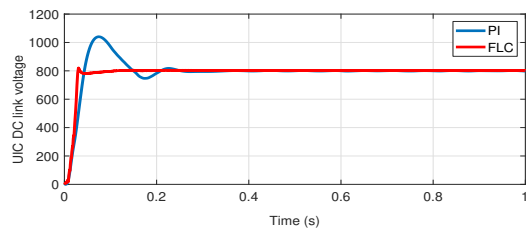
(b) Grid current



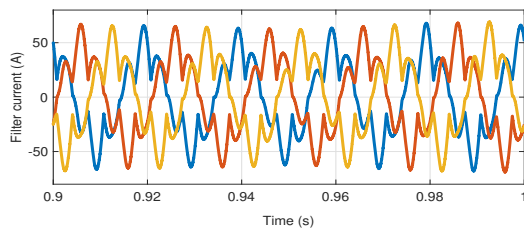
(c) Grid voltage current



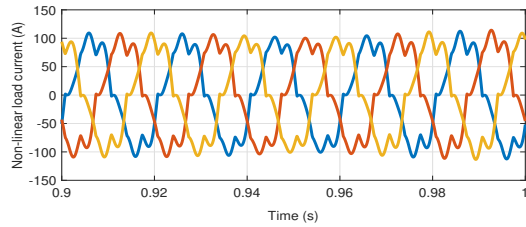
(d) Grid power factor



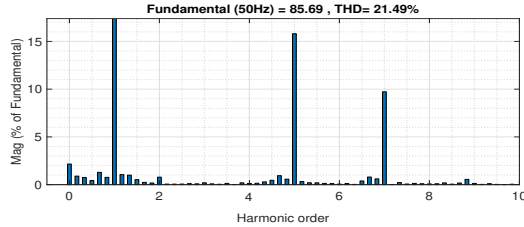
(e) UIC DC link voltage



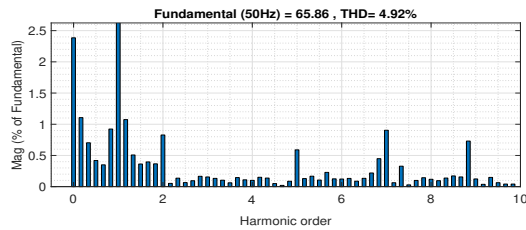
(f) Filter current



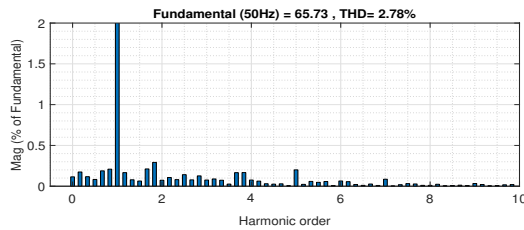
(g) Non-linear load current



(h) Grid current THD before filtering



(i) Grid current THD after filtering - PI



(j) Grid current THD after filtering - FLC

**Figure 2.17:** Harmonic analysis of AC CHM with DFIG+PV under BUGBNL

## 2.4.4 AC CHM (DFIG+PV) – Unbalanced distorted grid and unbalanced non-linear load conditions

The  $P_{aclinearload}$  of 22 kW,  $P_{acnon-linearload}$  of 11 kW, and  $P_{dclload}$  of 20 kW demands are less than the  $P_{wind}$  generation of 42 kW at wind speed of 12m/s and  $P_{pv}$  generation of 32 kW at irradiation of  $800W/m^2$  as shown in Figures 2.18(a)–2.18(d). Hence, the surplus power of 21 kW of both the  $P_{pv}$  and  $P_{wind}$  is injected into the  $P_{grid}$  as shown in Figure 2.18(e). In order to inject the surplus power into the  $P_{grid}$ , both the UICs should operate in the inverter mode as shown in Figure 2.18(f).

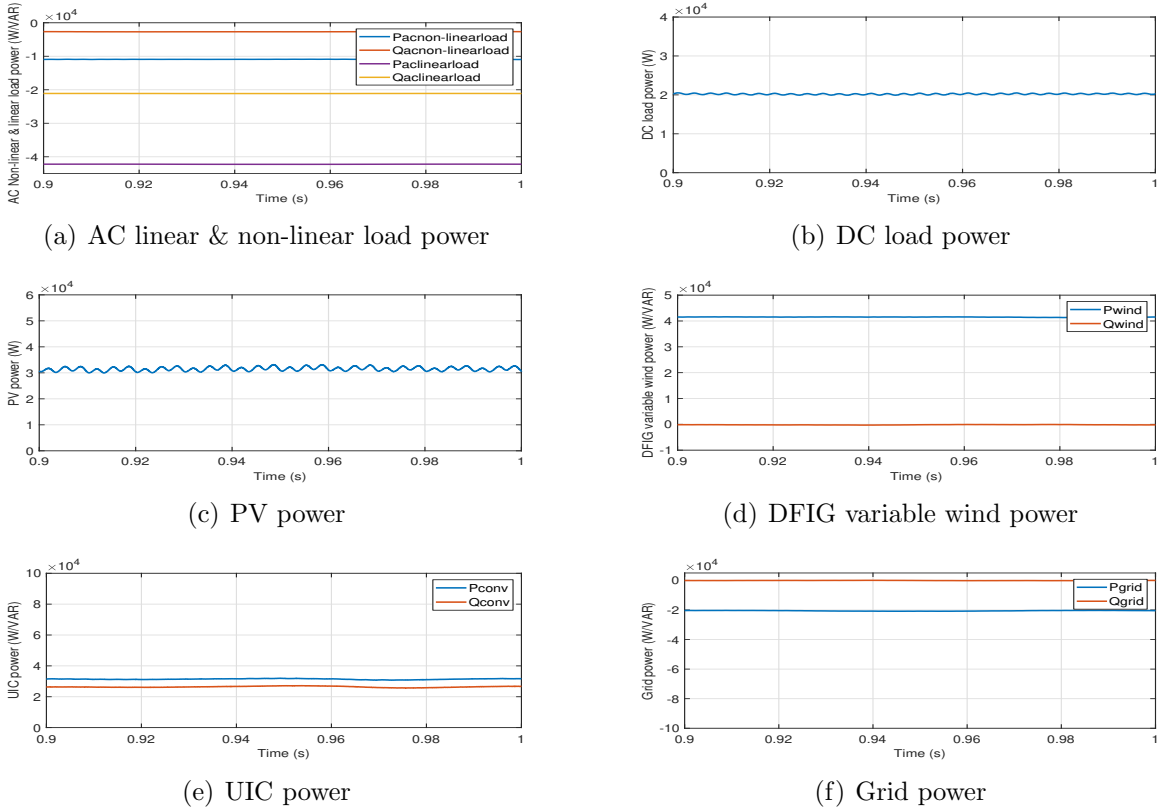
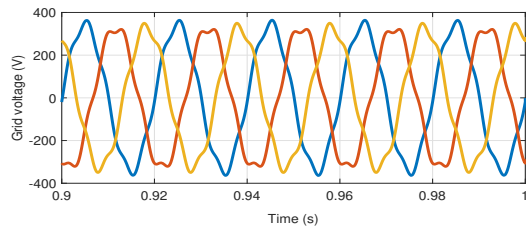
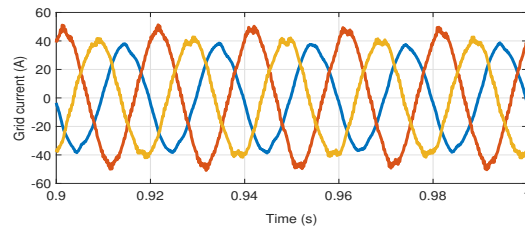


**Figure 2.18:** Power flow analysis of AC CHM with DFIG+PV under UDGUNL

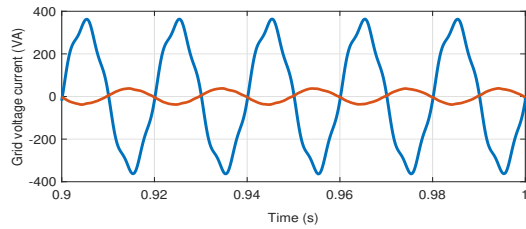
Figures 2.19(a)–2.19(g) represents the grid voltage, grid current, grid voltage current, grid power factor, UIC DC link voltage, filter current, and nonlinear load current, respectively. In Figure 2.19(h), the observation of the grid current THD before compensation is 44.27%. After compensation, the grid current THD improved with the FLC (2.91%) over the PI (4.30%) as shown in Figure 2.19(i) and Figure 2.19(j), respectively. The obtained grid current THD values are within the harmonic limits.



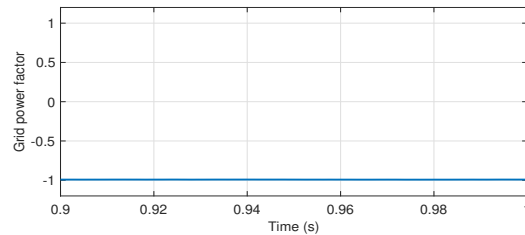
(a) Grid voltage



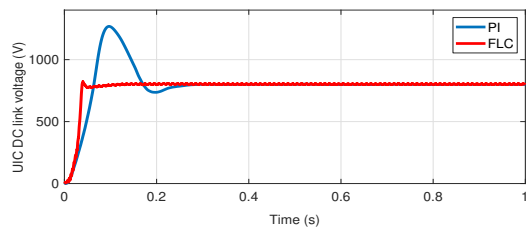
(b) Grid current



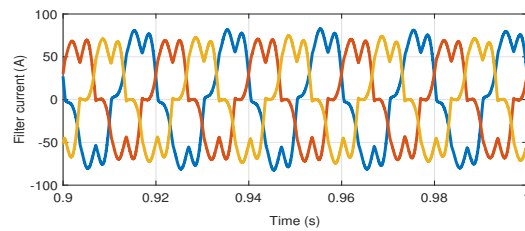
(c) Grid voltage current



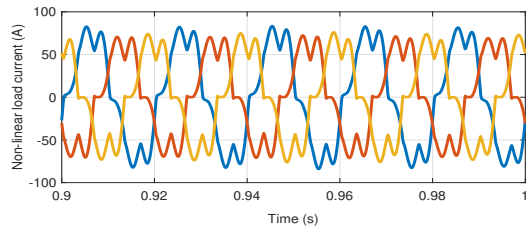
(d) Grid power factor



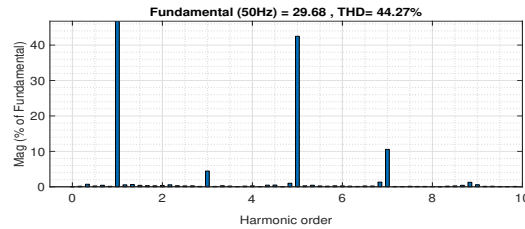
(e) UIC DC link voltage



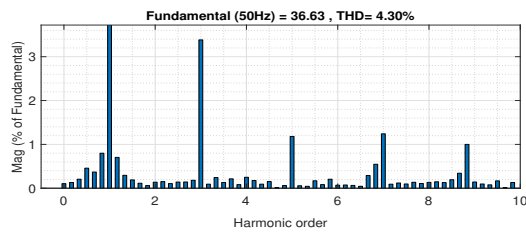
(f) Filter current



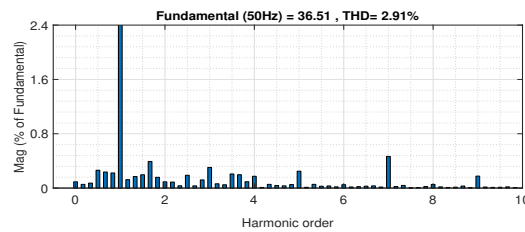
(g) Non-linear load current



(h) Grid current THD before filtering



(i) Grid current THD after filtering - PI



(j) Grid current THD after filtering - FLC

**Figure 2.19:** Harmonic analysis of AC CHM with DFIG+PV under UDGUNL

In case of unbalanced non-linear load on the AC grid side, the filter current flows to the CCP through the 4<sup>th</sup> leg of the UIC to compensate the neutral current as depicted in Figure 2.20.

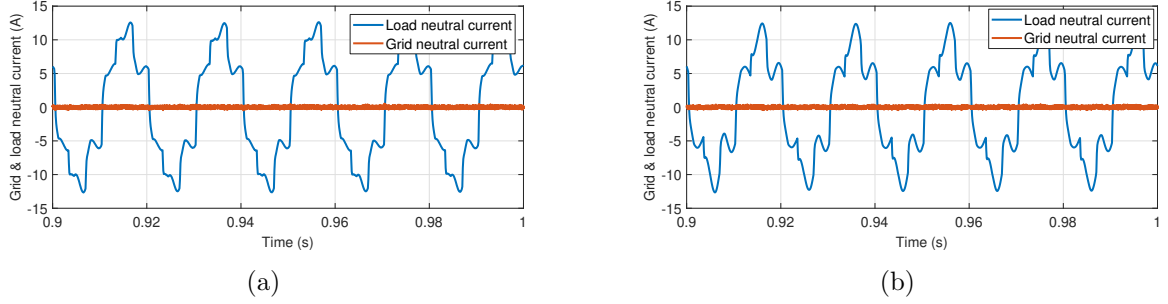


**Figure 2.20:** Grid and load neutral current of AC CHM under UDGUNL with a) PMSG+PV b) DFIG+PV

## 2.5 Summary

The MATLAB simulation was carried out by considering the variation of: a) PV array and PMSG variable wind turbine RES, and b) PV array and DFIG variable wind turbine RES under different grid and load scenarios. As discussed in Sections 2.4.1, 2.4.2, 2.4.3, and 2.4.4:

- The d-q load current control based FLC and PI perform the real power transfer to the various loads at the AC bus efficiently. The power flow equations for all the case studies were shown below,

- (a) In Section 2.4.1 with (PMSG+PV) RES, the UIC acted as an inverter mode. Thus, the power flow equation is:

$$P_{pv} + P_{wind} + P_{grid} = P_{acnon-linearload} + P_{dload}$$

- (b) In Section 2.4.2 with (PMSG+PV) RES, the UIC acted as an inverter mode. Thus, the power flow equation is:

$$P_{pv} + P_{wind} = P_{grid} + P_{acnon-linearload} + P_{dload}$$

- (c) In Section 2.4.3 with (DFIG+PV) RES, the UIC acted as an inverter mode. Thus, the power flow equation is:

$$P_{pv} + P_{wind} + P_{grid} = P_{aclinearload} + P_{acnon-linearload} + P_{dload}$$

- (d) In Section 2.4.4 with (DFIG+PV) RES, the UIC acted as an inverter mode. Thus, the power flow equation is:

$$P_{pv} + P_{wind} = P_{grid} + P_{aclinearload} + P_{acnon-linearload} + P_{dload}$$

- Further, the improved grid current THD holds good using the d-q load current control based FLC compared with the d-q load current control based PI and is summarized in Table 2.8.

**Table 2.8:** Performance of the grid current THD for AC CHM system

Case	Grid current THD before filtering	Grid current THD after filtering	
		PI	FLC
a) PMSG+PV RES under BUGBNL	19.54%	4.68%	2.87%
b) PMSG+PV RES under UDGUNL	46.22%	4.41%	2.34%
c) DFIG+PV RES under BUGBNL	21.49%	4.92%	2.78%
d) DFIG+PV RES under UDGUNL	44.27%	4.30%	2.91%

# Chapter 3

## Performance Analysis of DC Coupled Hybrid Micro-grid System

### 3.1 Introduction

If DC renewable energy sources such as PV, fuel cell, etc. are significant sources of power in the micro-grid, then the DC coupled micro-grid system is preferable. The DC coupled micro-grid system has its advantages over the AC coupled micro-grid system. Since there is no reactive power, there are several benefits of the DC coupled micro-grid system, such as voltage fall, reduction of power losses, etc. Therefore, it is simpler to plan, implement, and operate. Further, there is no need for synchronization to incorporate the various sources of energy. Hence, the DC coupled micro-grid system is about twice as reliable as the AC coupled micro-grid system (Planas et al., 2015). The available RES and DC loads are connected to the DC bus through various converters. If the DC coupled micro-grid system is connected to main-grid, then an appropriate controller is required for the BIC to synchronize with it. The AC non-linear loads are connected at the AC bus or the CCP. The bi-directional controller regulates the real power flow between the AC and the DC bus along with harmonic current mitigation at the CCP. These issues have to be taken into consideration to develop an appropriate bi-directional controller.

This chapter deals with firstly, the overall control of the DC coupled hybrid micro-grid system. Secondly, the simulation results of the DC coupled hybrid micro-grid system are discussed through a comparative study.

## 3.2 Overall Control Diagram of the DC Coupled Hybrid Micro-grid System

The overall control diagram of the DC coupled hybrid micro-grid is shown in Figure 3.1. A PV array is connected to the DC bus through the DC-DC boost converter, whereas the PMSG wind is connected to the DC bus through the AC-DC rectifier and the DC-DC boost converter. The DC resistive load is connected to the DC bus. Further, both the PV array and the PMSG wind are connected to the AC bus through a common BIC (which acts as rectifier or inverter). The AC non-linear RL load connected to the AC bus is integrated with the main-grid. The BIC controls the power flow exchange between the AC bus and the DC bus with harmonic current limits as per the IEEE 519 standards at the AC bus.

In Chapter 2, Sections 2.3.1 and 2.3.2, the modeling of the PV array and PMSG variable wind turbine RES was studied. The variable output DC voltage obtained from both the RES is given to the DC-DC boost converter to maintain the DC voltage constant at the DC bus. The BIC has been controlled by the d-q load current control based-PI and FLC as discussed in the Chapter 2, Section 2.2.2.

This d-q load current control based-PI and FLC performs active power flow with the current harmonics mitigation efficiently:

- a) If the DC load demand is greater than the generation of PV array and PMSG variable wind turbine RES, then the BIC acts as a rectifier.

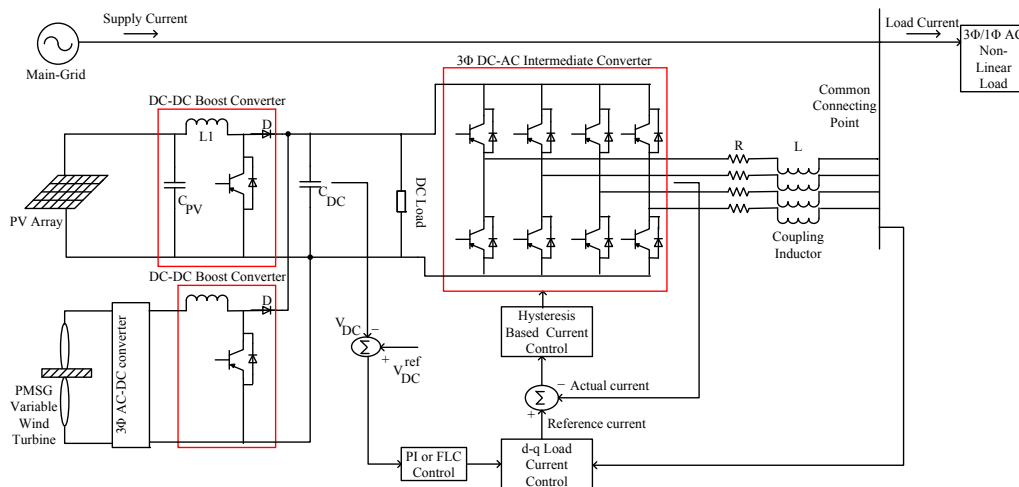


**Figure 3.1:** Overall control diagram of DC CHM



b) If the DC load demand is lesser than the generation of PV array and PMSG variable wind turbine RES, then the BIC acts as an inverter.

### 3.3 Simulation Results for DC CHM System

The MATLAB simulation is carried out for the DC coupled hybrid micro-grid system as shown in Figure 3.1. The performance of the proposed system is analyzed using the d-q load current technique based-fuzzy logic and PI controller. To validate the proposed control technique, different case studies are performed by considering balanced and unbalanced grid and load conditions with variation in RES. The simulation parameters for PV array, BIC, PV boost converter, and main-grid were used the same as in Chapter 2, Sections 2.3.1, and 2.4. The simulation parameters of the PMSG and its boost converter are shown in Table 3.1 (Jayalakshmi et al., 2012).

**Table 3.1:** Parameters of the PMSG variable wind turbine model

Parameters	Values
DC link voltage, $V_{DC}$	800 V
DC link capacitor, $C_{DC}$	7000 $\mu$ F
Rated power, $P_{nom}$	50 kW
Stator phase resistance, $R_s$	2.875 $\Omega$
d & q-axis phase inductance	8.5 mH
Torque constant	12 N-m/A peak
Inertia	$0.8 \times 10^{-03}$ kg-m <sup>2</sup>
No. of pole pairs	8
Boost converter inductor, $L_1$	0.2 mH

#### 3.3.1 DC CHM (PMSG+PV) – Balanced undistorted grid and balanced non-linear load conditions

In this case, the performance of the overall system is analyzed with a balanced, undistorted grid and balanced non-linear load conditions. The power generated by the PMSG wind,  $P_{wind}$  of 30 kW at 7 m/s and PV array,  $P_{pv}$  of 39 kW at 1000 W/m<sup>2</sup> are shown in Figure 3.2(a) and Figure 3.2(b). At the DC grid side, the hybrid solar-wind energy sources (HSWES) are generating 69 kW power more than the  $P_{dload}$  demand of 20 kW as shown in Figure 3.2(c). The  $P_{acloadnon-linear}$  demand of 10 KW is met by the HSWES through the BIC,  $P_{conv}$  of 49 kW as shown in Figure 3.2(d)

and Figure 3.2(e). Now, the BIC operates in inverter mode. Further, the remaining surplus power of 39 kW is transferred to the main-grid as shown in Figure 3.2(f).

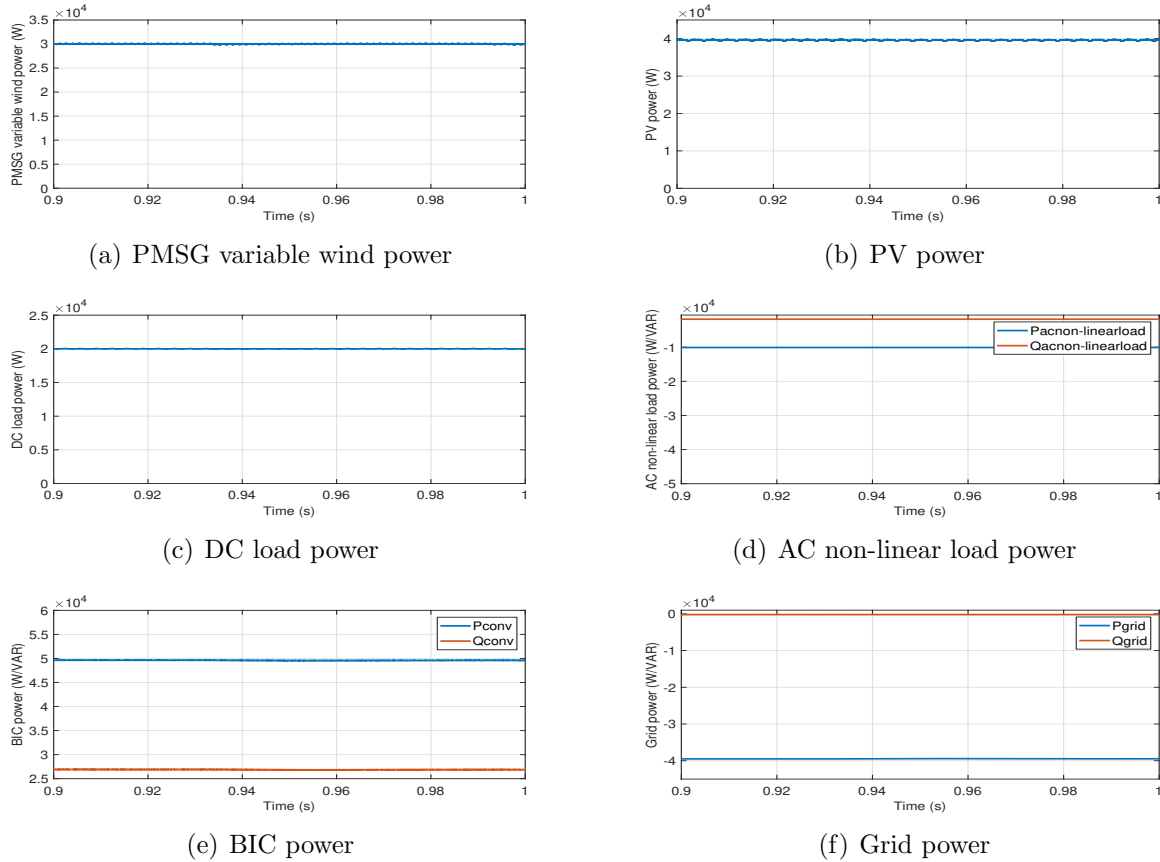
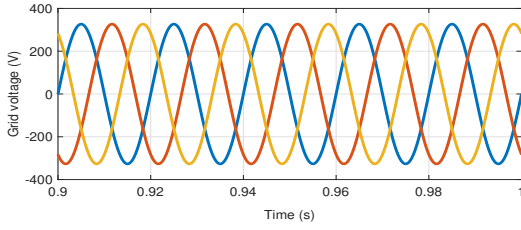
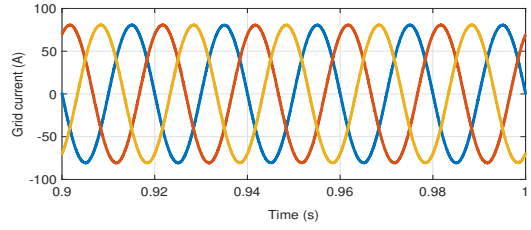


**Figure 3.2:** Power flow analysis of DC CHM with PMSG+PV under BUGBNL

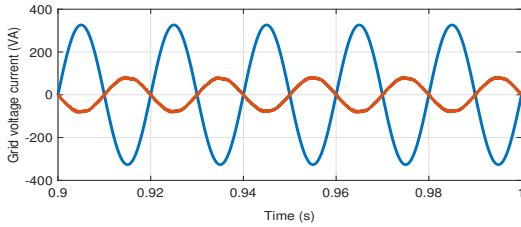
Initially, before applying the d-q load current control to the BIC, the grid current is similar to the load current as depicted in Figure 3.3(g). After applying the d-q load current control to the BIC, the extraction of reference filter currents is compared with the actual filter currents by the HBCC as shown in Figure 3.3(f). Figure 3.3(e) shows that the DC link voltage is regulated to play the main role in transferring the power between the AC-DC buses. Further, the polluted grid current starts to filter out to become almost sinusoidal as shown in Figure 3.3(b). The grid current THD before compensation is 23.58%, and after compensation with PI is 2.51%, and with FLC is 0.32% as shown in the Figures 3.3(h)–3.3(j). Figure 3.3(a), Figure 3.3(c), and Figure 3.3(d) represents the grid voltage, grid voltage current, and grid power factor, respectively.



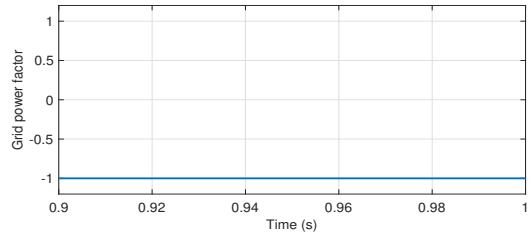
(a) Grid voltage



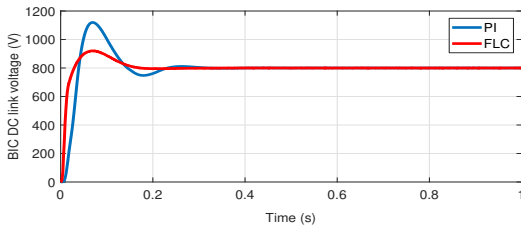
(b) Grid current



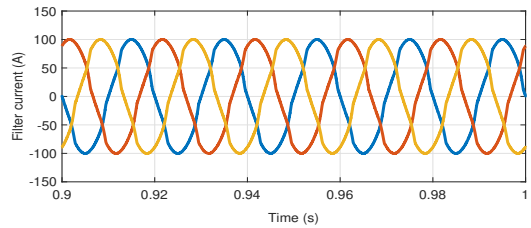
(c) Grid voltage current



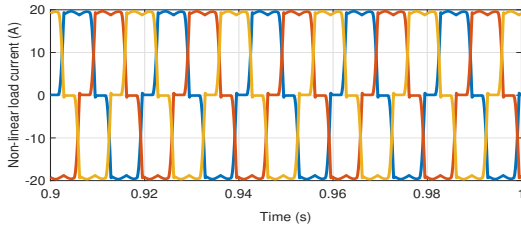
(d) Grid power factor



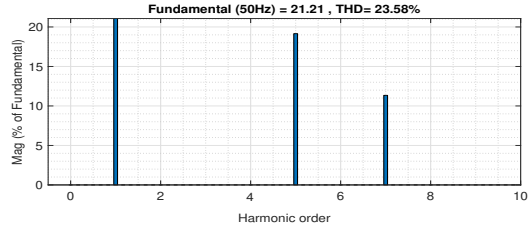
(e) BIC DC link voltage



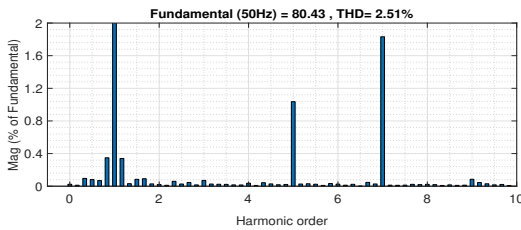
(f) Filter current



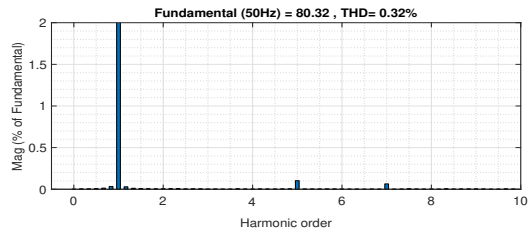
(g) Non-linear load current



(h) Grid current THD before filtering



(i) Grid current THD after filtering - PI



(j) Grid current THD after filtering - FLC

**Figure 3.3:** Harmonic analysis of DC CHM with PMSG+PV under BUGBNL

### 3.3.2 DC CHM (PMSG+PV) – Unbalanced distorted grid and unbalanced non-linear load conditions

In this case, the overall system performance is analyzed with unbalanced distorted grid and unbalanced non-linear load conditions. The power generated by the PMSG wind,  $P_{wind}$  of 24 kW at 6 m/s and PV array,  $P_{pv}$  of 24 kW at 600 W/m<sup>2</sup> is illustrated in Figure 3.4(a) and Figure 3.4(b). The HSUES generation of 48 kW is less than the DC load demand,  $P_{dload}$  of 50 kW as shown in Figure 3.4(c). The remaining deficit power of 24 kW drawn from the main-grid,  $P_{grid}$  as shown in Figure 3.4(d). To satisfy the DC load demand on the DC grid side, BIC,  $P_{conv}$  of 2 kW acts as a rectifier as shown in Figure 3.4(e). On the AC grid side, the AC load,  $P_{acnon-linearload}$  of 22 kW have been drawn the power from only main-grid,  $P_{grid}$  as shown in Figure 3.4(f).

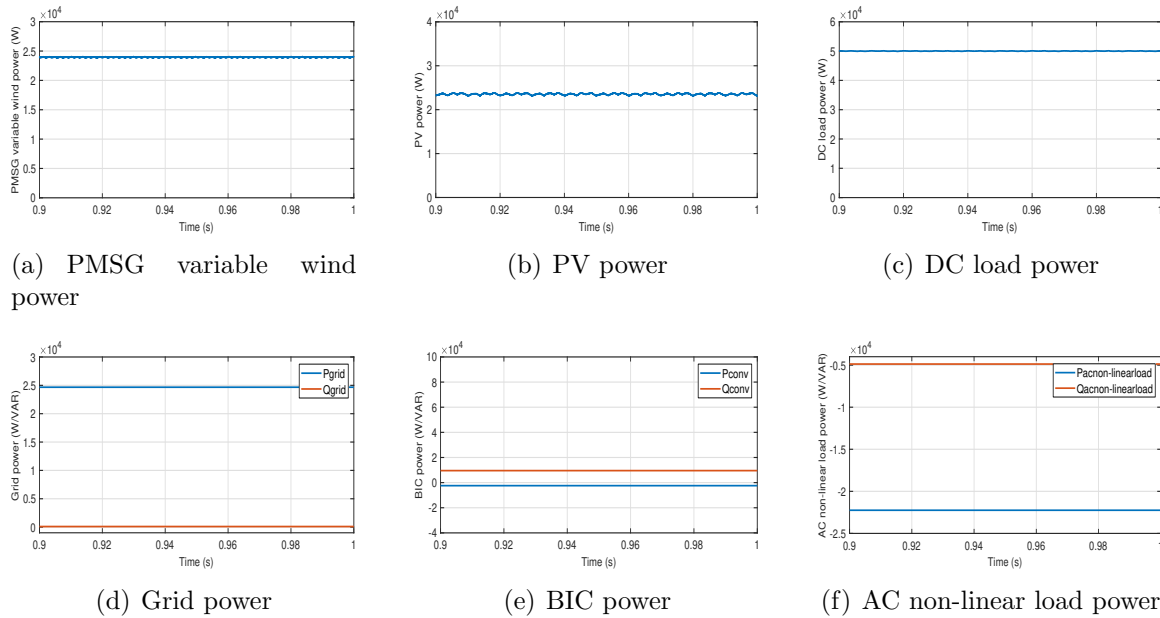


**Figure 3.4:** Power flow analysis of DC CHM with PMSG+PV under UDGUNL

Initially, before connecting the BIC to the network, the grid current is similar to the load current as shown in Figure 3.5(g). After connecting the BIC to the network, the reference filter currents extract from the d-q method, and these currents are compared with the actual filter currents by the HBCC as shown in Figure 3.5(f). Figure 3.5(e) shows that the DC link voltage is regulated to play the main role in transferring the power between the AC-DC buses. Further, the polluted grid current starts to filter out to become almost sinusoidal as shown in Figure 3.5(b). The

grid current THD before compensation is 14.58% and after compensation with PI is 3.11% and with FLC is 0.43% as shown in the Figures 3.5(h)–3.5(j). Figure 3.5(a), Figure 3.5(c), and Figure 3.5(d) represents the grid voltage, grid voltage current, and grid power factor, respectively.

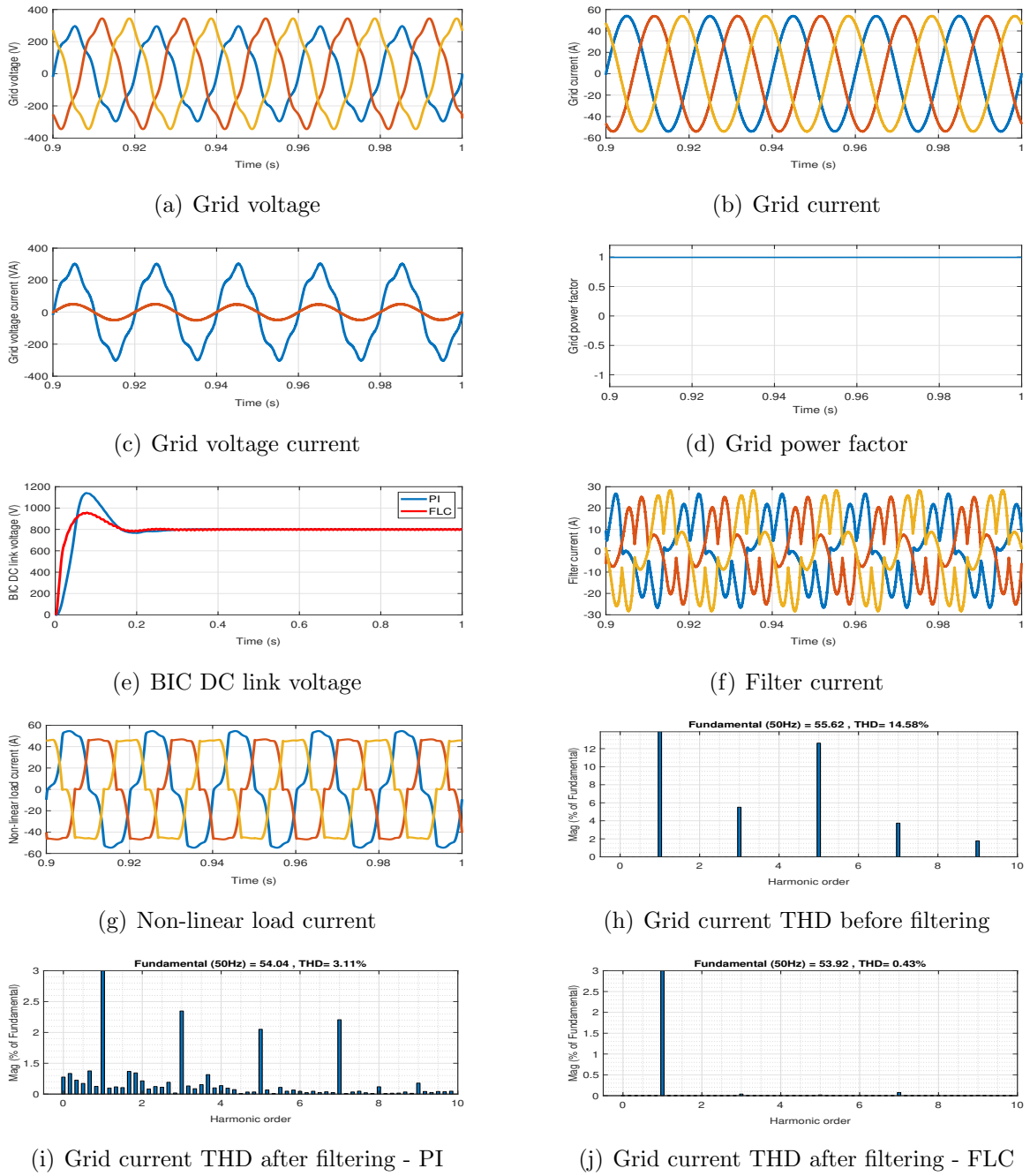


**Figure 3.5:** Harmonic analysis of DC CHM with PMSG+PV under UDGUNL

In case of unbalanced non-linear load on the AC grid side, the filter current flows to the CCP through the 4<sup>th</sup> leg of the BIC to compensate the neutral current as depicted in Figure 3.6.

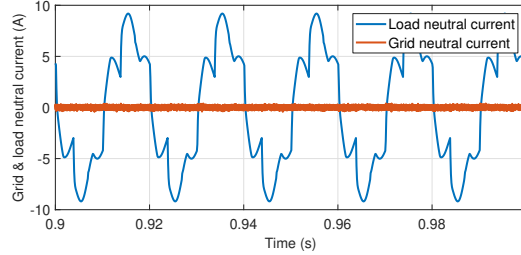


**Figure 3.6:** Grid and load neutral current of AC CHM with PMSG+PV under UDGUNL

### 3.4 Summary

The MATLAB simulation was carried out considering the variation of the PV array and the PMSG variable wind turbine RES under different grid and load scenarios. As discussed in Sections 3.3.1 and 3.3.2:

- The d-q load current control based FLC and PI performed the real power exchange between the AC and DC bus to supply the AC and DC loads effectively. The power flow equations for all the case studies were shown below,

- (a) In Section 3.3.1 with (PMSG+PV) RES, the BIC acted as an inverter. Therefore, the power flow equations at the DC grid side and the AC grid side are:

$$P_{pv} + P_{wind} = P_{dcload}$$

$$P_{conv} = P_{grid} + P_{acnon-linearload}$$

- (b) In Section 3.3.2 with (PMSG+PV) RES, the BIC acted as a rectifier. Therefore, the power flow equations at the DC grid side and the AC grid side are:

$$P_{pv} + P_{wind} + P_{conv} = P_{dcload}$$

$$P_{grid} = P_{acnon-linearload}$$

- Further, the grid current THD was improved using the d-q load current control based FLC compared with the d-q load current control based PI and is summarized in Table 3.2.

**Table 3.2:** Performance of the grid current THD for DC CHM system

Case	Grid current THD before filtering	Grid current THD after filtering	
		PI	FLC
a) PMSG+PV RES under BUGBNL	23.58%	2.51%	0.32%
b) PMSG+PV RES under UDGUNL	14.58%	3.11%	0.43%





# Chapter 4

## Performance Analysis of AC-DC Coupled Hybrid Micro-grid System

### 4.1 Introduction

The most used topology is the AC coupled microgrid, which offers a simple way to integrate DGs or RES into the existing power distribution system. However, it has a few drawbacks such as DGs or RES synchronization with the main-grid, as the reactive power flow management increases the power losses in the system. Therefore, the AC coupled micro-grid topology is switched over to the DC coupled micro-grid topology, as there is an absence of synchronization of the RES or DG's and the reactive power flow control. This topology needs to restructure the current distribution system, and consequently, the cost increases drastically. Also, the DC protection system is more challenging than the AC protection system. The AC-DC coupled hybrid micro-grid topology is causing great interest due to the pros and cons of the AC and DC coupled micro-grid topologies. This topology consists of AC renewable sources and the AC loads are connected to the AC bus, and DC renewable sources and the DC loads are connected to the DC bus. Hence, the efficiency of this system is improved with reduced power conversion stages. This topology requires proper co-ordination control to regulate the real power exchange between the AC and DC bus, as well as current harmonics compensation (Sahoo et al., 2017, Unamuno and Barrena, 2015a).

In this chapter: i) The overall control of the AC-DC coupled hybrid micro-grid system is presented, and ii) Simulation results of this system for different case studies.

## 4.2 Overall Control Diagram of the AC-DC Coupled Hybrid Micro-grid System

The overall control diagram of the AC-DC coupled hybrid micro-grid is shown in Figure 4.1. The PV array and DC resistive load are connected to the DC bus through the DC-DC boost converter, and it inverts to the AC bus through a bi-directional intermediate converter (inverter or rectifier). The PMSG or DFIG variable wind turbine through the AC-DC-AC back-to-back converter and the AC non-linear RL load is connected to the AC bus integrated with the main-grid. Thus, the AC-DC-AC/DC-AC-DC power conversion stages and losses are reduced.

In Chapter 2, Sections 2.3.1 and 2.3.2 or 2.3.3, the modeling of the PV array and PMSG or DFIG variable wind turbine RES was studied. The variable output DC voltage obtained from the PV array is given to the DC-DC boost converter to maintain the DC voltage constant at the DC bus. From the DFIG variable wind turbine, the real and reactive power output is controlled by the rotor side converter (RSC), whereas the DC link voltage is regulated to maintain constant voltage using a grid side converter (GSC). The BIC is controlled by the d-q load current control based-PI and FLC discussed in Chapter 2, Section 2.2.2. This d-q load current control based-PI and FLC performs active power flow with current harmonics mitigation efficiently as: a) If the generation of the PV array is more than the DC load demand, the BIC acts as an inverter, and b) If the generation of the PV array is less than the DC load demand, the BIC acts as a rectifier.

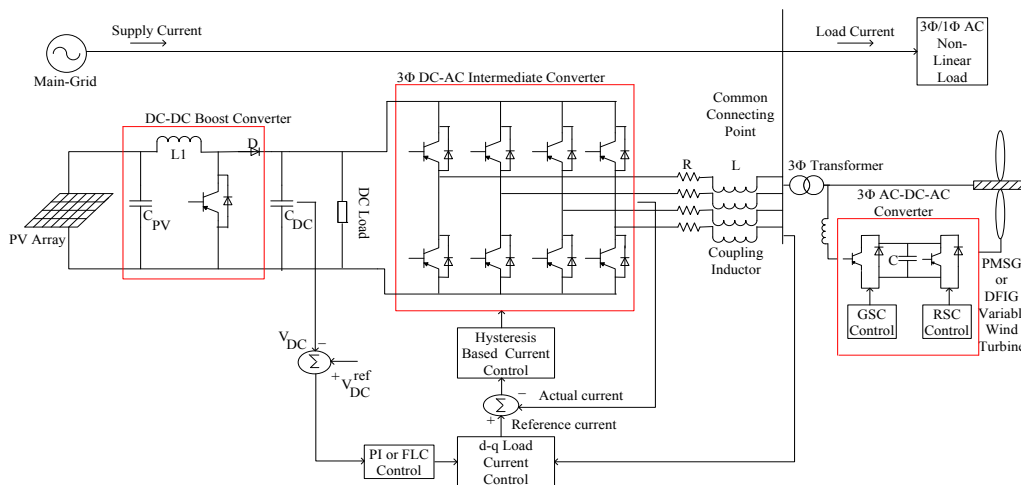


**Figure 4.1:** Overall control diagram of AC-DC CHM

### 4.3 Simulation Results for AC-DC CHM System

The MATLAB simulation is carried out for the AC-DC coupled hybrid micro-grid system as shown in Figure 4.1. The performance of the proposed d-q load current control based-FLC and PI controller is analyzed and validated for different case studies. The simulation parameters of the PV array, PMSG or DFIG variable wind turbine, and main-grid were used the same as in Chapter 2, Sections 2.3.1, 2.3.2 or 2.3.3, and 2.4.

#### 4.3.1 AC-DC CHM (PMSG+PV) – Balanced undistorted grid and balanced non-linear load conditions

The  $P_{acnon-linearload}$  of 10 kW and  $P_{dcload}$  of 20 kW demands are less than the  $P_{wind}$  generation of 30 kW at wind speed of 7 m/s and the  $P_{pv}$  generation of 39 kW at irradiation of 1000 W/m<sup>2</sup> as shown in Figures 4.2(a)–4.2(d). Hence, the surplus power of 39 kW of both the  $P_{pv}$  and  $P_{wind}$  is injected into the  $P_{grid}$  as shown in Figure 4.2(e). In order to inject the surplus power into the  $P_{grid}$ , the BIC should operate in inverter mode as shown in Figure 4.2(f).

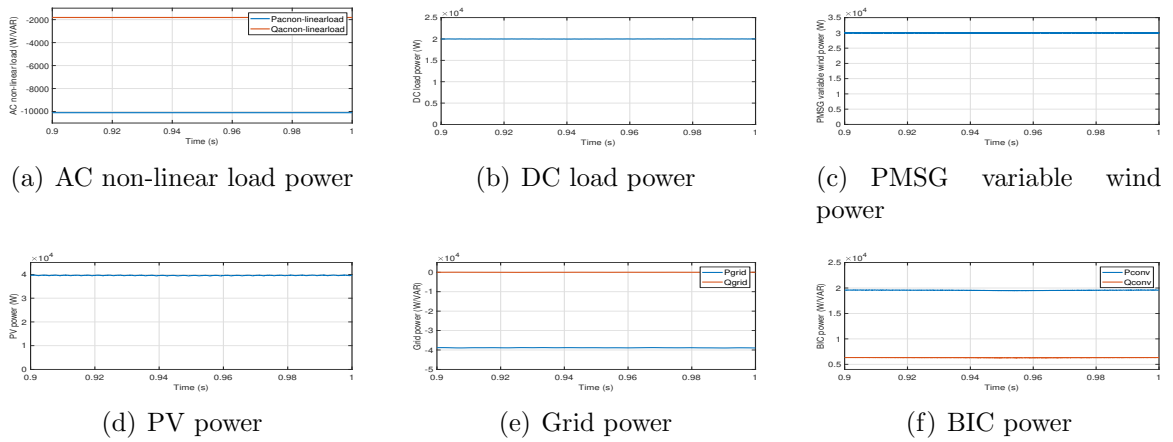
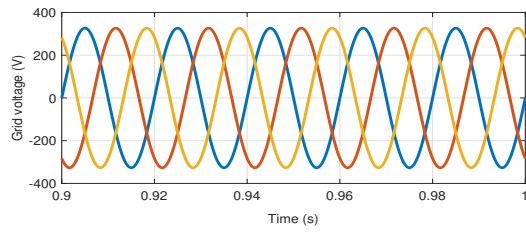
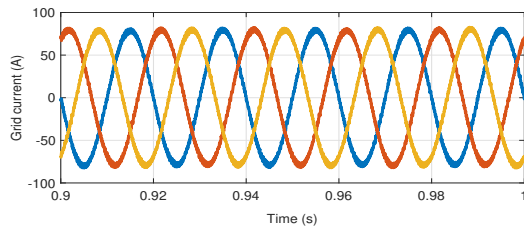


**Figure 4.2:** Power flow analysis of AC-DC CHM with PMSG+PV under BUGBNL

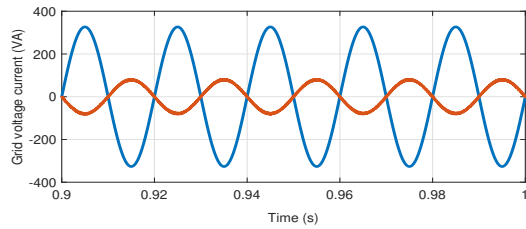
Figures 4.3(a)–4.3(g) represents the grid voltage, grid current, grid voltage current, grid power factor, BIC DC link voltage, filter current, and non-linear load current, respectively. In Figure 4.3(h), the observation of the grid current THD before compensation is 13.49%. After compensation, the grid current THD is improved with the FLC (2.46%) over the PI (4.18%) as shown in Figure 4.3(i) and Figure 4.3(j), respectively. The obtained grid current THD values are within the harmonic limits.



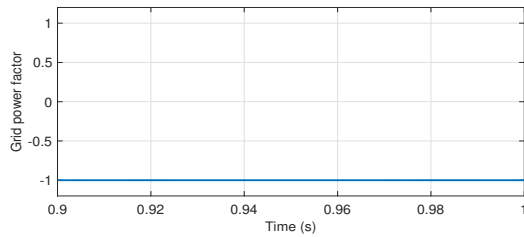
(a) Grid voltage



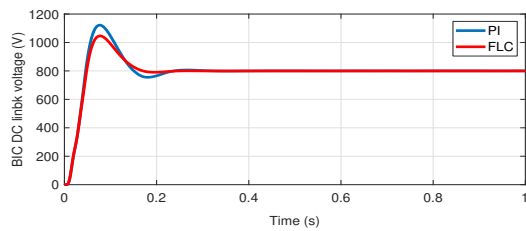
(b) Grid current



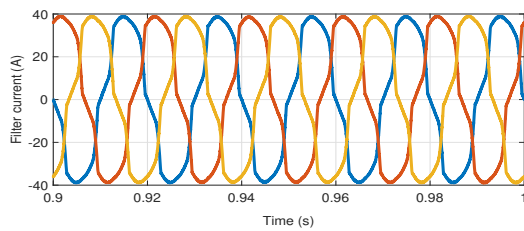
(c) Grid voltage current



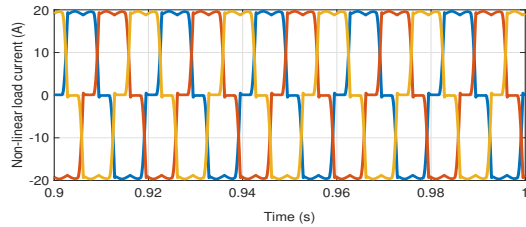
(d) Grid power factor



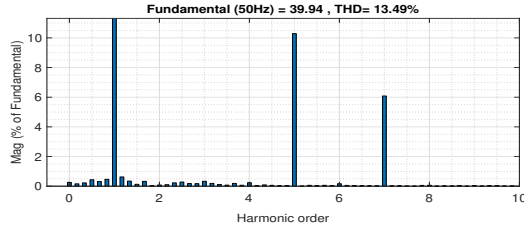
(e) BIC DC link voltage



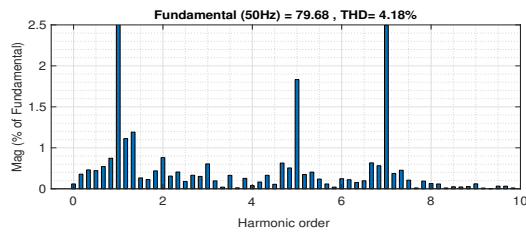
(f) Filter current



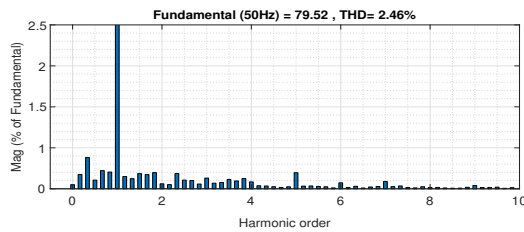
(g) Non-linear load current



(h) Grid current THD before filtering



(i) Grid current THD after filtering - PI



(j) Grid current THD after filtering - FLC

**Figure 4.3:** Harmonic analysis of AC-DC CHM with PMSG+PV under BUGBNL

### 4.3.2 AC-DC CHM (PMSG+PV) – Balanced undistorted grid and unbalanced non-linear load conditions

The  $P_{dload}$  of 20 kW demand is equal to the  $P_{pv}$  generation of 20 kW at irradiation of  $500 \text{ W/m}^2$  as shown in Figure 4.4(a) and Figure 4.4(b). The  $P_{acnon-linearload}$  of 19 kW demand is less than the  $P_{wind}$  generation of 38 kW at a wind speed of 9 m/s are shown in Figure 4.4(c) and Figure 4.4(d). Hence, there is no action of the BIC,  $P_{conv}$  that means BIC is in rest or idle mode as shown in Figure 4.4(e). The surplus power of 19 kW from  $P_{wind}$  is injected into the  $P_{grid}$  as shown in Figure 4.4(f).

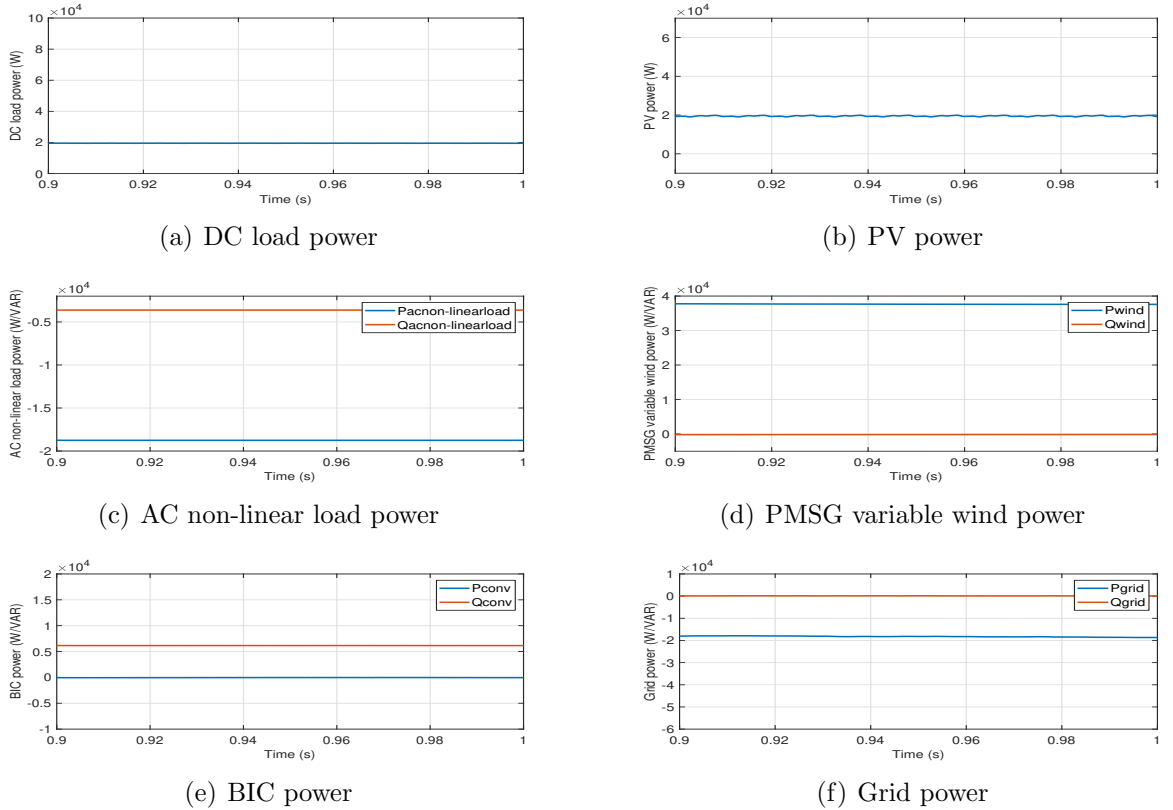
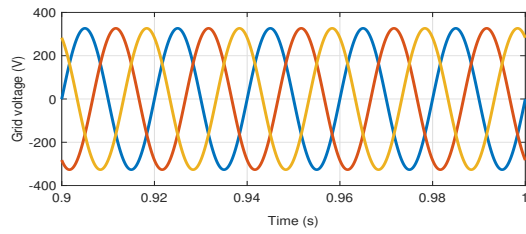
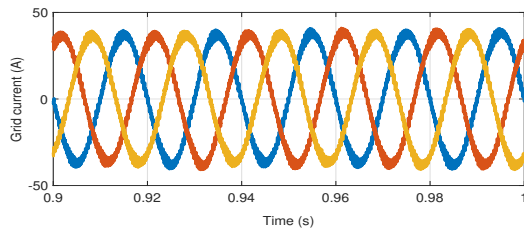


**Figure 4.4:** Power flow analysis of AC-DC CHM with PMSG+PV under BUGUNL

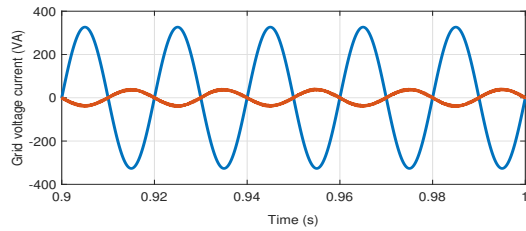
Figures 4.5(a)–4.5(g) represents the grid voltage, grid current, grid voltage current, grid power factor, BIC DC link voltage, filter current, and non-linear load current, respectively. In Figure 4.5(h), the observation of the grid current THD before compensation is 23.99%. After compensation, the grid current THD is improved with the FLC (2.35%) over the PI (4.44%) as shown in Figure 4.5(i) and Figure 4.5(j), respectively. The obtained grid current THD values are within the harmonic limits.



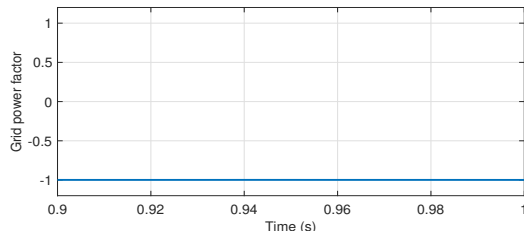
(a) Grid voltage



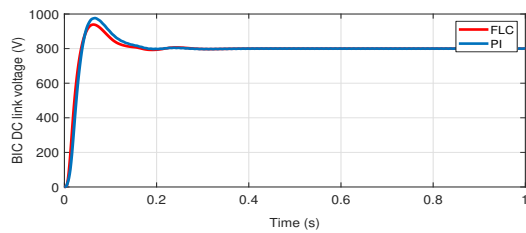
(b) Grid current



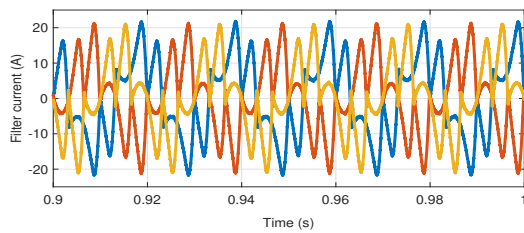
(c) Grid voltage current



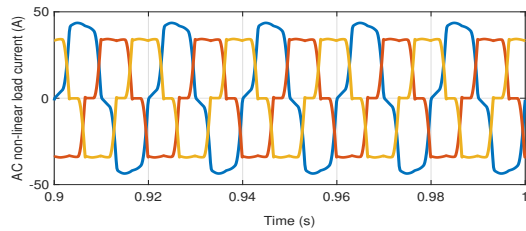
(d) Grid power factor



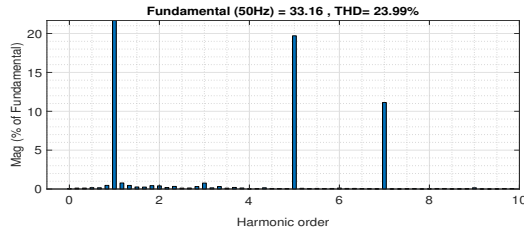
(e) BIC DC link voltage



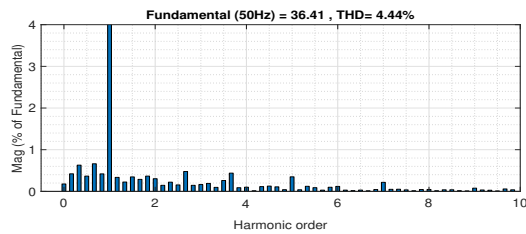
(f) Filter current



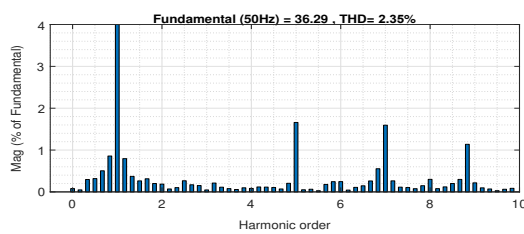
(g) Non-linear load current



(h) Grid current THD before filtering



(i) Grid current THD after filtering - PI



(j) Grid current THD after filtering - FLC

**Figure 4.5:** Harmonic analysis of AC-DC CHM with PMSG+PV under BUGUNL

### 4.3.3 AC-DC CHM (PMSG+PV) – Unbalanced distorted grid and unbalanced non-linear load conditions

The  $P_{acnon-linearload}$  of 37 kW and  $P_{dcload}$  of 50 kW demands are more than the  $P_{pv}$  generation of 31kW at irradiation of 800 W/m<sup>2</sup> and the  $P_{wind}$  generation of 34 kW at a wind speed of 8 m/s as shown in Figures 4.6(a)–4.6(d). Hence, the required deficit power of 22 kW is supplied by the  $P_{grid}$  to meet the load demands as shown in Figure 4.6(e). In order to supply power to the  $P_{dcload}$  and  $P_{acnon-linearload}$ , the BIC should operate in rectifier mode as shown in Figure 4.6(f).

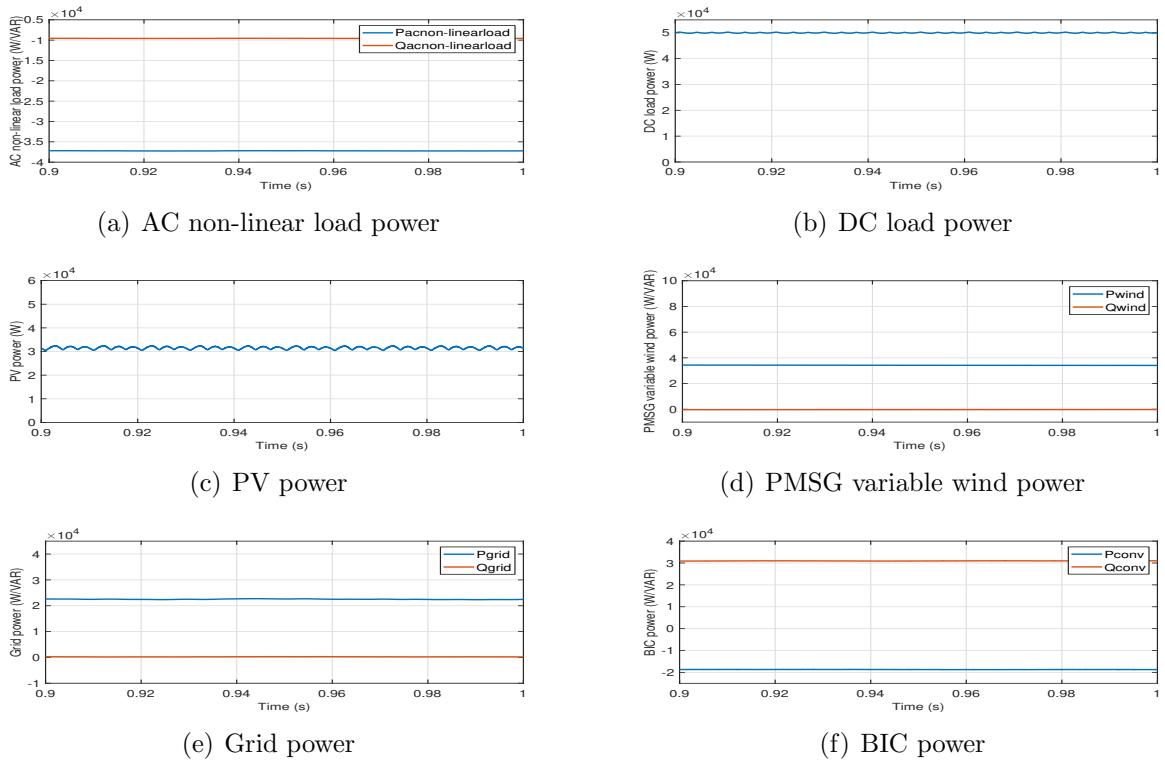
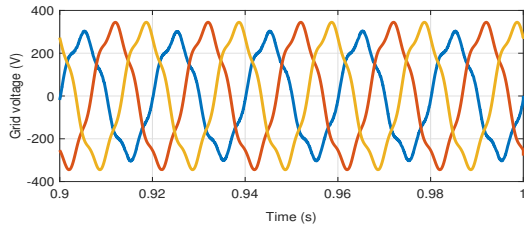
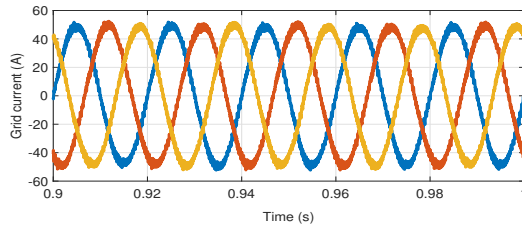


**Figure 4.6:** Power flow analysis of AC-DC CHM with PMSG+PV under UDGUNL

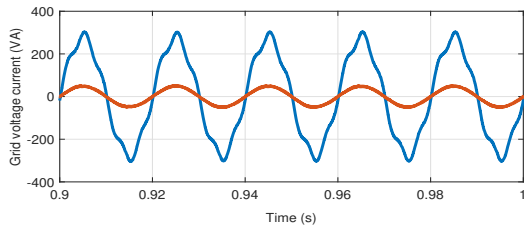
Figures 4.7(a)–4.7(g) represents the grid voltage, grid current, grid voltage current, grid power factor, BIC DC link voltage, filter current, and non-linear load current, respectively. From Figure 4.7(h), it can be observed that the grid current THD before compensation is 21.28%. After compensation, the grid current THD improved with the FLC over the PI. It is evident from Figure 4.7(i) and Figure 4.7(j) that the grid current THD is 4.00% with PI and 2.90% with FLC, which is well within the IEEE standard limits.



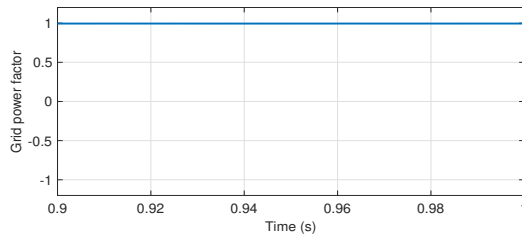
(a) Grid voltage



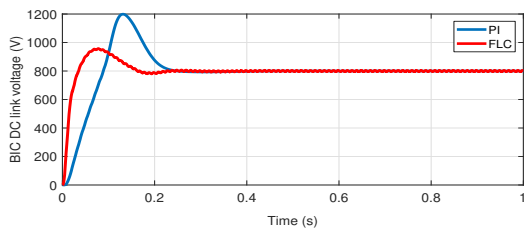
(b) Grid current



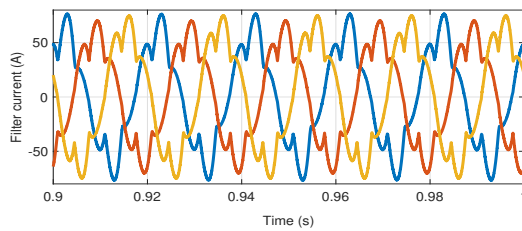
(c) Grid voltage current



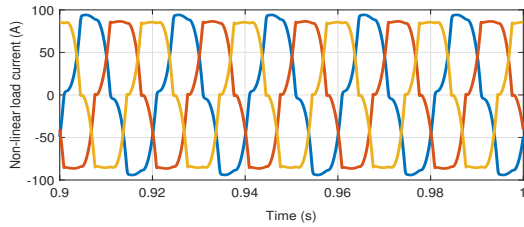
(d) Grid power factor



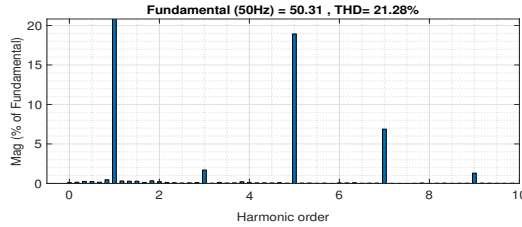
(e) BIC DC link voltage



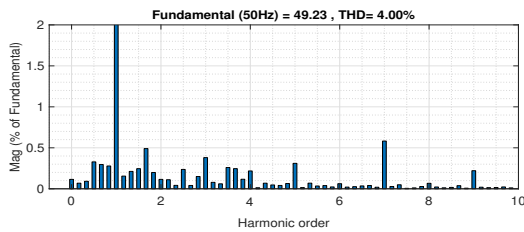
(f) Filter current



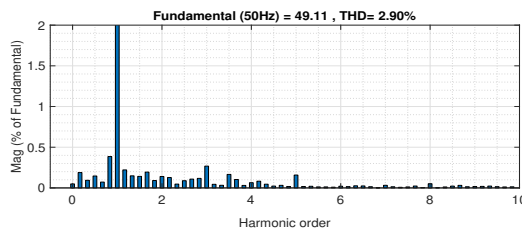
(g) Non-linear load current



(h) Grid current THD before filtering



(i) Grid current THD after filtering - PI



(j) Grid current THD after filtering - FLC

**Figure 4.7:** Harmonic analysis of AC-DC CHM with PMSG+PV under UDGUNL



### 4.3.4 AC-DC CHM (DFIG+PV) – Balanced undistorted grid and balanced non-linear load conditions

The  $P_{aclinearload}$  of 25 kW,  $P_{acnon-linearload}$  of 15 kW, and  $P_{dcload}$  of 25 kW demands are more than the  $P_{pv}$  generation of 3 kW at irradiation of  $100 \text{ W/m}^2$  and  $P_{wind}$  generation of 30 kW at wind speed of 7 m/s as shown in Figures 4.8(a)–4.8(d). Hence, the required deficit power of 32 kW is supplied by  $P_{grid}$  to meet the load demands as shown in Figure 4.8(e). In order to supply power to the  $P_{dcload}$ ,  $P_{aclinearload}$ , and  $P_{acnon-linearload}$ , the BIC should operate in rectifier mode as shown in Figure 4.8(f).

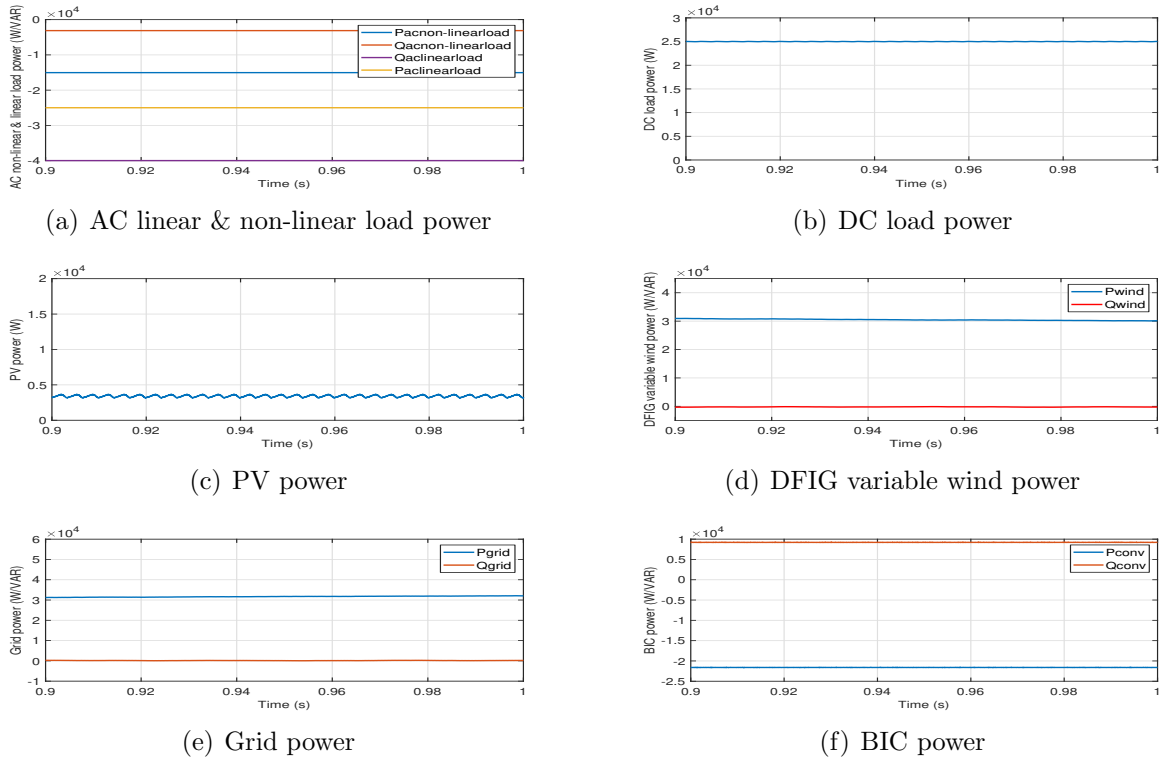
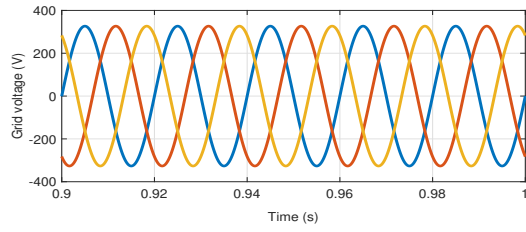
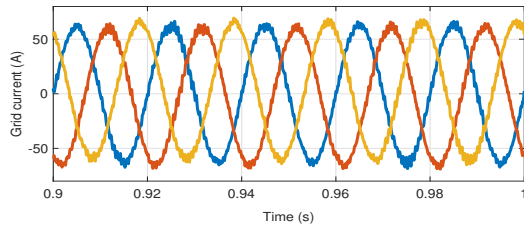


**Figure 4.8:** Power flow analysis of AC-DC CHM with DFIG+PV under BUGBNL

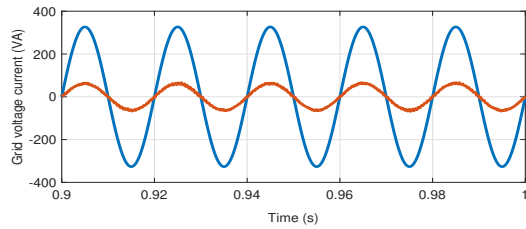
Figures 4.9(a)–4.9(g) represents the grid voltage, grid current, grid voltage current, grid power factor, BIC DC link voltage, filter current, and non-linear load current, respectively. From Figure 4.9(h), it can be observed that the grid current THD before compensation is 37.31%. After compensation, the grid current THD improved with the FLC over the PI as shown in Figure 4.9(i) and Figure 4.9(j). It is evident from these figures that the grid current THD is 4.47% with PI and 2.47% with FLC, which is well within the IEEE standard limits.



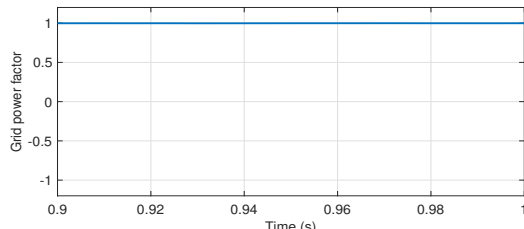
(a) Grid voltage



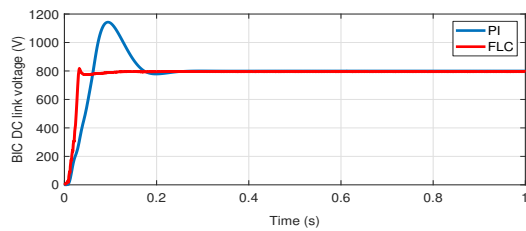
(b) Grid current



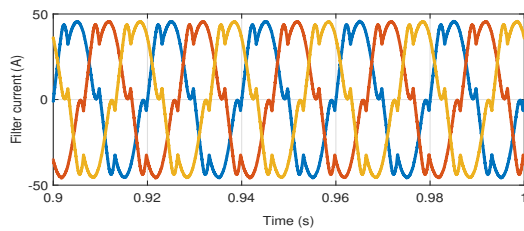
(c) Grid voltage current



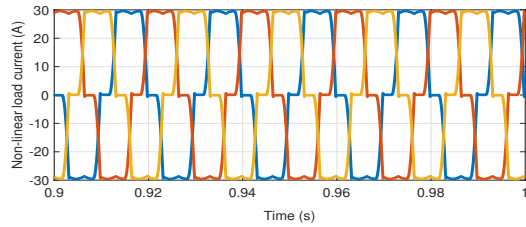
(d) Grid power factor



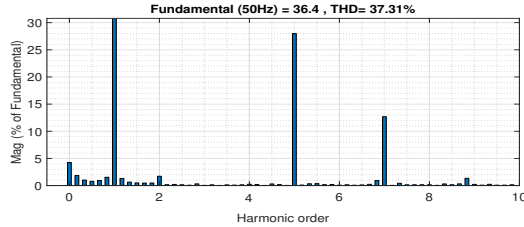
(e) BIC DC link voltage



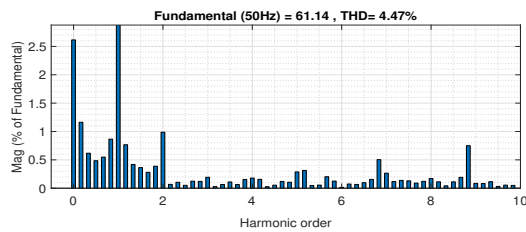
(f) Filter current



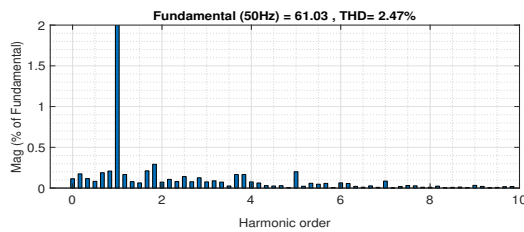
(g) Non-linear load current



(h) Grid current THD before filtering



(i) Grid current THD after filtering - PI



(j) Grid current THD after filtering - FLC

**Figure 4.9:** Harmonic analysis of AC-DC CHM with DFIG+PV under BUGBNL

### 4.3.5 AC-DC CHM (DFIG+PV) – Balanced undistorted grid and unbalanced non-linear load conditions

The  $P_{dload}$  of 16 kW demand is equal to the  $P_{pv}$  generation of 16 kW at irradiation of  $400 \text{ W/m}^2$  as shown in Figure 4.10(a) and Figure 4.10(b). The  $P_{acnon-linearload}$  of 27 kW and  $P_{aclinearload}$  of 35 kW demands are more than the  $P_{wind}$  generation of 34 kW at wind speed of 8 m/s as shown in Figure 4.10(c) and Figure 4.10(d). Hence, there is no action of the BIC,  $P_{conv}$  that means BIC is in rest or idle mode as shown in Figure 4.10(e). The required deficit power of 28 kW is drawn from the  $P_{grid}$  as shown in Figure 4.10(f).

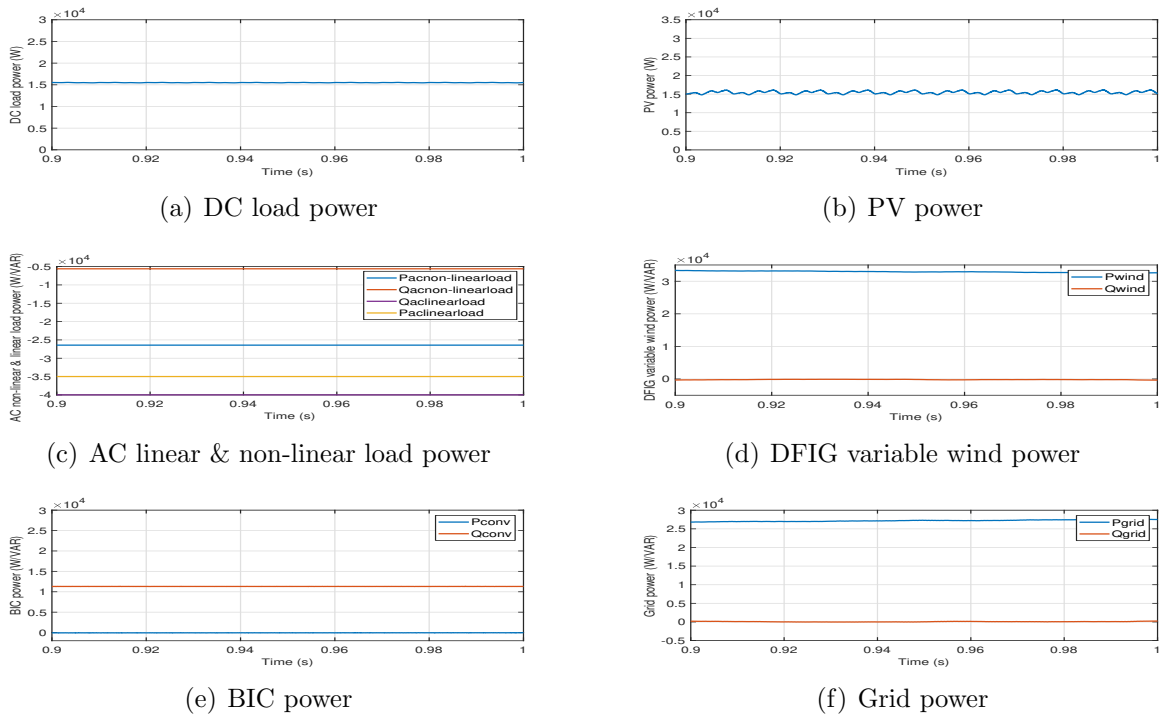
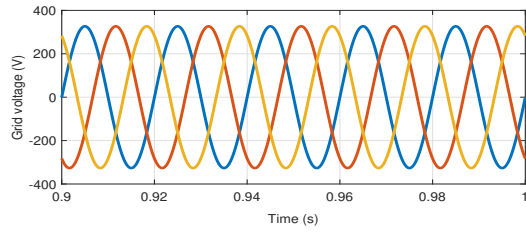
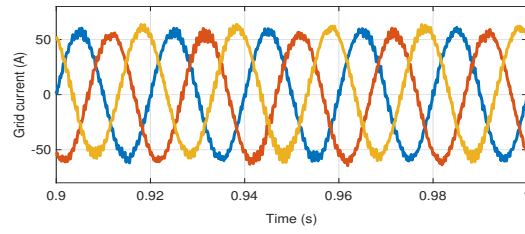


**Figure 4.10:** Power flow analysis of AC-DC CHM with DFIG+PV under BUGUNL

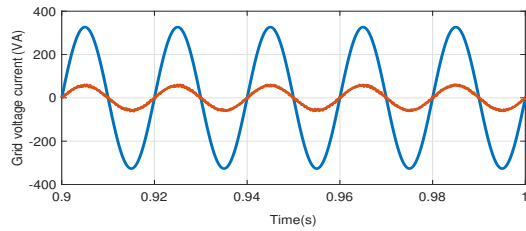
Figures 4.11(a)–4.11(g) represents the grid voltage, grid current, grid voltage current, grid power factor, BIC DC link voltage, filter current, and nonlinear load current, respectively. In Figure 4.11(h), the observation of the grid current THD before compensation is 42.53%. After compensation, the grid current THD is improved with the FLC (2.95%) over the PI (4.77%) as shown in Figure 4.11(i) and Figure 4.11(j), respectively. The obtained grid current THD values are within the IEEE standard harmonic limits.



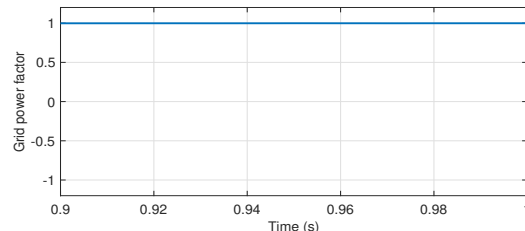
(a) Grid voltage



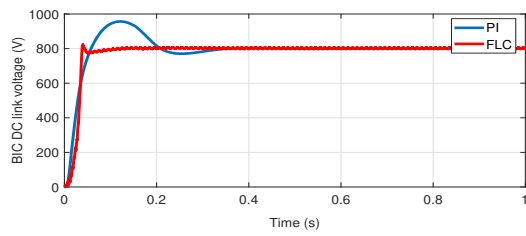
(b) Grid current



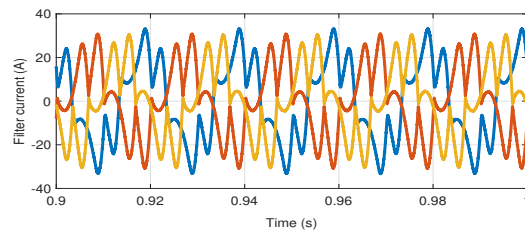
(c) Grid voltage current



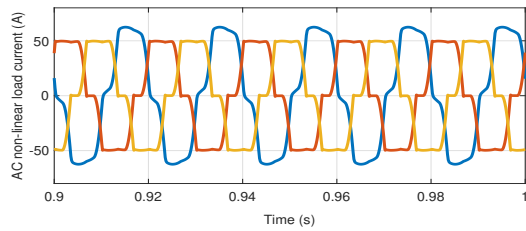
(d) Grid power factor



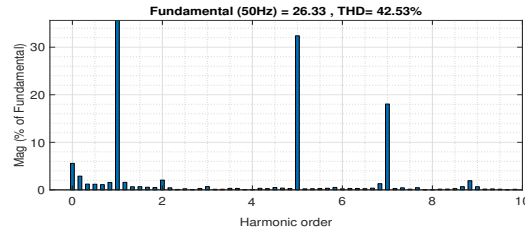
(e) BIC DC link voltage



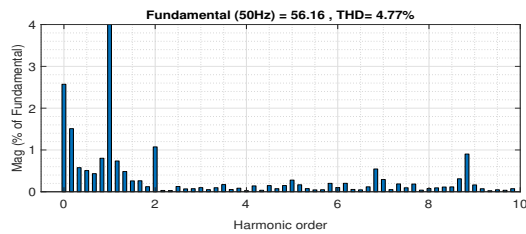
(f) Filter current



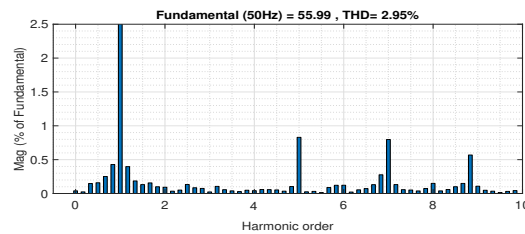
(g) Non-linear load current



(h) Grid current THD before filtering



(i) Grid current THD after filtering - PI



(j) Grid current THD after filtering - FLC

**Figure 4.11:** Harmonic analysis of AC-DC CHM with DFIG+PV under BUGUNL

### 4.3.6 AC-DC CHM (DFIG+PV) – Unbalanced distorted grid and unbalanced non-linear load conditions

The  $P_{aclinearload}$  of 20 kW,  $P_{acnon-linearload}$  of 13 kW, and  $P_{dcload}$  of 20 kW demands are less than the  $P_{wind}$  generation of 42 kW at wind speed of 12 m/s and  $P_{pv}$  generation of 32 kW at irradiation of  $800 \text{ W/m}^2$  as shown in Figures 4.12(a)–4.12(d). Hence, the surplus power of 21 kW of both  $P_{pv}$  and  $P_{wind}$  is injected into the  $P_{grid}$  as shown in Figure 4.12(e). In order to inject the surplus power into the  $P_{grid}$ , the BIC should operate in inverter mode as shown in Figure 4.12(f).

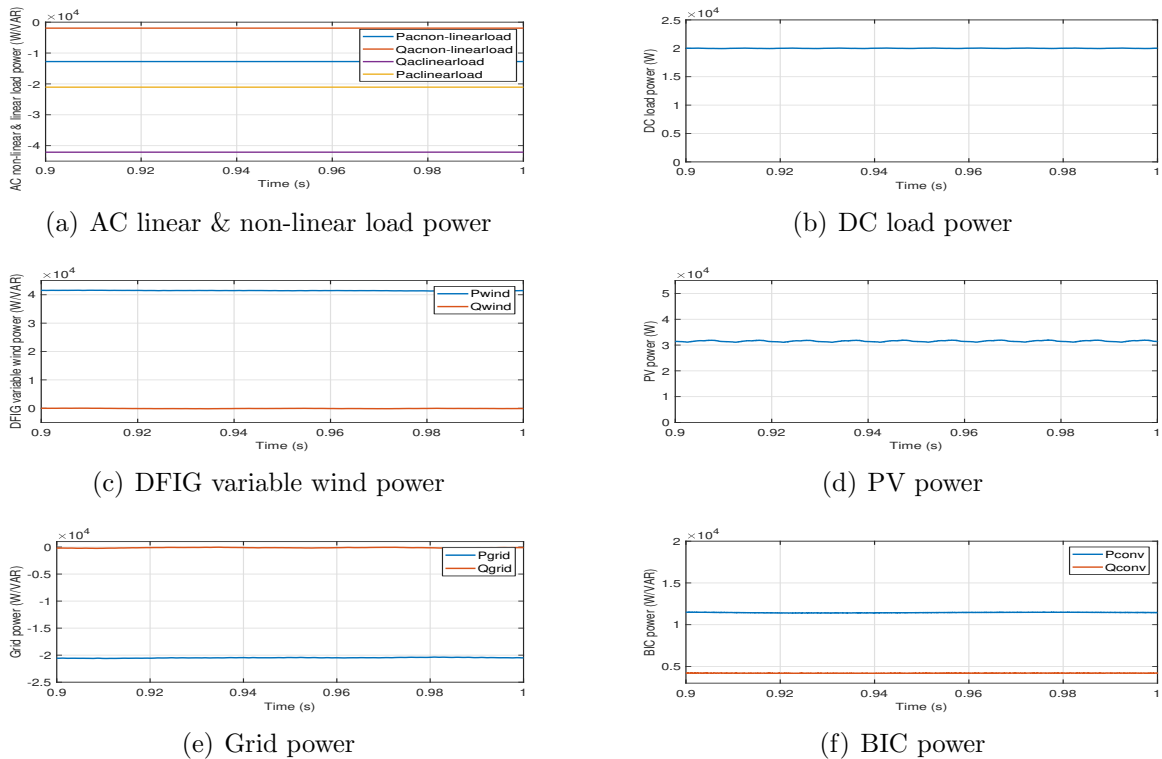
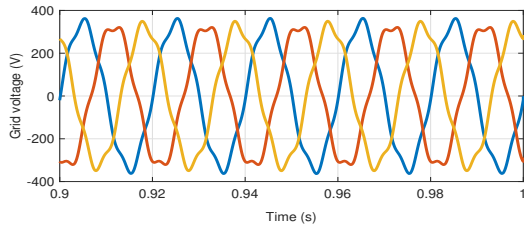
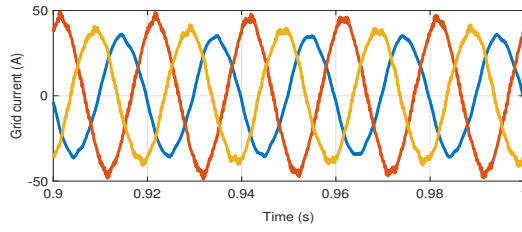


**Figure 4.12:** Power flow analysis of AC-DC CHM with DFIG+PV under UDGUNL

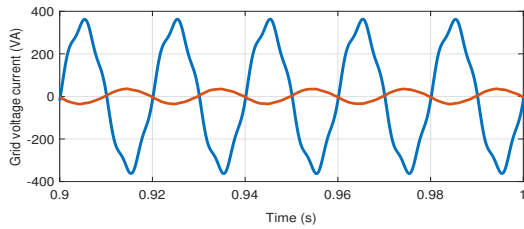
Figures 4.13(a)–4.13(g) represents the grid voltage, grid current, grid voltage current, grid power factor, BIC DC link voltage, filter current, and non-linear load current, respectively. In Figure 4.13(h), the observation of the grid current THD before compensation is 34.14%. After compensation, the grid current THD is improved with the FLC (2.27%) over the PI (3.89%) as shown in Figure 4.13(i) and Figure 4.13(j), respectively. The obtained grid current THD values are within the harmonic limits.



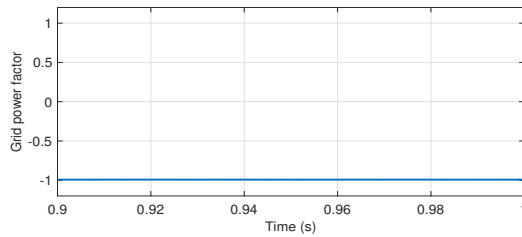
(a) Grid voltage



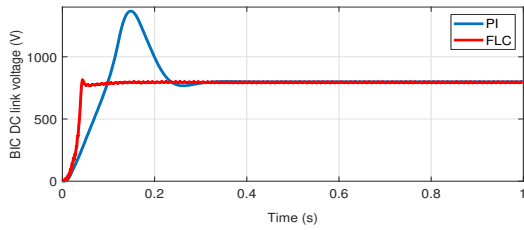
(b) Grid current



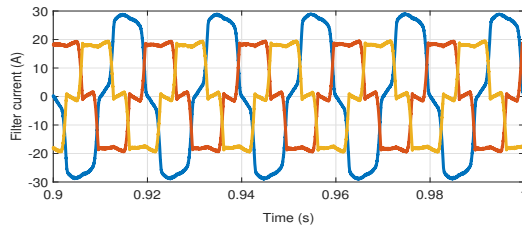
(c) Grid voltage current



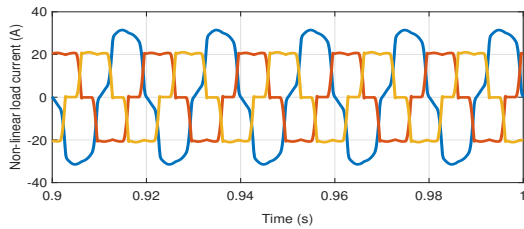
(d) Grid power factor



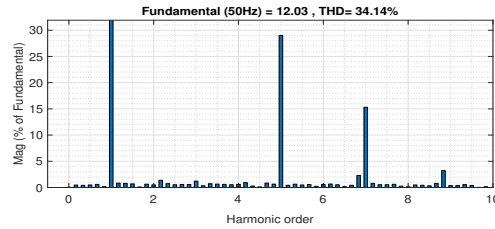
(e) BIC DC link voltage



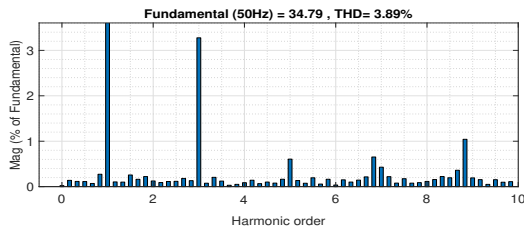
(f) Filter current



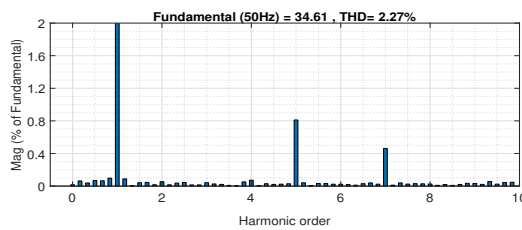
(g) Non-linear load current



(h) Grid current THD before filtering



(i) Grid current THD after filtering - PI



(j) Grid current THD after filtering - FLC

**Figure 4.13:** Harmonic analysis of AC-DC CHM with DFIG+PV under UDGUNL

In case of unbalanced non-linear load on the AC grid side, the filter current flows to the CCP through the 4<sup>th</sup> leg of the BIC to compensate the neutral current as depicted in Figure 4.14.

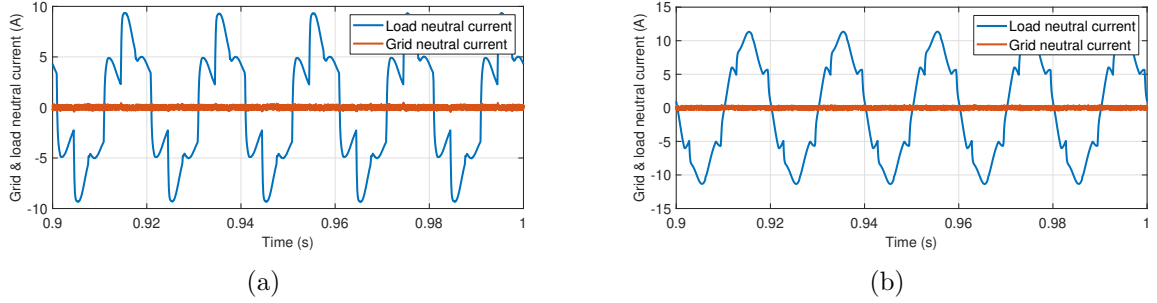


**Figure 4.14:** Grid and load neutral current of AC-DC CHM under UDGUNL with a) PMSG+PV b) DFIG+PV

## 4.4 Summary

The MATLAB simulation was carried out by considering the variation of: a) PV array and PMSG variable wind turbine RES, and b) PV array and DFIG variable wind turbine RES under different grid and load scenarios. As discussed in Sections 4.3.1– 4.3.6:

- The d-q load current control based FLC and PI perform the real power exchange between the AC and DC bus to supply the various loads efficiently. The power flow equations for all the case studies were shown below,

- (a) In Section 4.3.1 with (PMSG+PV) RES, the BIC acted as an inverter. Therefore, the power flow equations at the DC bus and the AC bus are:

$$P_{pv} = P_{dload}$$

$$P_{conv} + P_{wind} = P_{grid} + P_{acnon-linearload}$$

- (b) In Section 4.3.2 with (PMSG+PV) RES, the BIC was in rest mode. Therefore, the power flow equations at the DC bus and the AC bus are:

$$P_{pv} = P_{dload}$$

$$P_{wind} = P_{grid} + P_{acnon-linearload}$$

- (c) In Section 4.3.3 with (PMSG+PV) RES, the BIC acted as a rectifier. Therefore, the power flow equations at the DC bus and the AC bus are:

$$P_{pv} + P_{conv} = P_{dcload}$$

$$P_{wind} + P_{grid} = P_{acnon-linearload}$$

- (d) In Section 4.3.4 with (DFIG+PV) RES, the BIC acted as a rectifier. Therefore, the power flow equations at the DC bus and the AC bus are:

$$P_{pv} + P_{conv} = P_{dcload}$$

$$P_{wind} + P_{grid} = P_{aclinearload} + P_{acnon-linearload}$$

- (e) In Section 4.3.5 with (DFIG+PV) RES, the BIC was in rest mode. Therefore, the power flow equations at the DC bus and the AC bus are:

$$P_{pv} = P_{dcload}$$

$$P_{wind} + P_{grid} = P_{aclinearload} + P_{acnon-linearload}$$

- (f) In Section 4.3.6 with (DFIG+PV) RES, the BIC acted as an inverter. Therefore, the power flow equations at the DC bus and the AC bus are:

$$P_{pv} = P_{dcload}$$

$$P_{conv} + P_{wind} = P_{grid} + P_{aclinearload} + P_{acnon-linearload}$$



- Further, the grid current THD was improved using the d-q load current control based FLC compared with the d-q load current control based PI and is summarized in Table 4.1.

**Table 4.1:** Performance of the grid current THD for AC-DC CHM system

Case	Grid current THD before filtering	Grid current THD after filtering	
		PI	FLC
a) PMSG+PV RES under BUGBNL	13.49%	4.18%	2.46%
b) PMSG+PV RES under BUGUNL	23.99%	4.44%	2.35%
c) PMSG+PV RES under UDGUNL	21.28%	4.00%	2.90%
d) DFIG+PV RES under BUGBNL	37.31%	4.47%	2.47%
e) DFIG+PV RES under BUGUNL	42.53%	4.77%	2.95%
f) DFIG+PV RES under UDGUNL	34.14%	3.89%	2.27%



# Chapter 5

## Comparative Analysis of Power Conversion Losses for Various Configurations of the Hybrid Micro-grid Systems

### 5.1 Introduction

The power flow and harmonic analysis of the various configurations of the hybrid micro-grid systems were evaluated in the previous chapters. In both the AC and DC coupled hybrid micro-grid systems, because of more power conversion stages, the power conversion losses are more, leading to lower efficiency. Therefore, the AC-DC coupled hybrid micro-grid system has to be achieved with decreased power conversion losses, which effectively reduces the size of the set-up.

In this chapter, generalized power conversion loss calculation has been discussed wherein the merits of the AC-DC coupled hybrid micro-grid system has been validated and compared with the individual AC and DC coupled hybrid micro-grid systems. The power conversion loss calculation mainly depends on the conduction and switching loss of the semiconductor devices. The conduction and switching losses are calculated to examine the performance of the semiconductor devices. The calculation of the conduction and switching losses are based on the datasheet values.

This chapter is organized as follows: Firstly, the generalized power conversion loss analysis of the IGBT device is presented. Secondly, the overall control diagram of the various configurations of the hybrid micro-grid systems is presented. Finally, the simulation results show the power loss and power flow analysis for different topologies of the hybrid micro-grid systems through a comparative study.

## 5.2 Generalized Power Conversion Loss Analysis of the IGBT device

The generalized block diagram of the power conversion loss analysis of the IGBT device as shown in Figure 5.1. The power converters utilize the IGBT switches for their operation. The power conversion loss calculation mainly depends on the conduction

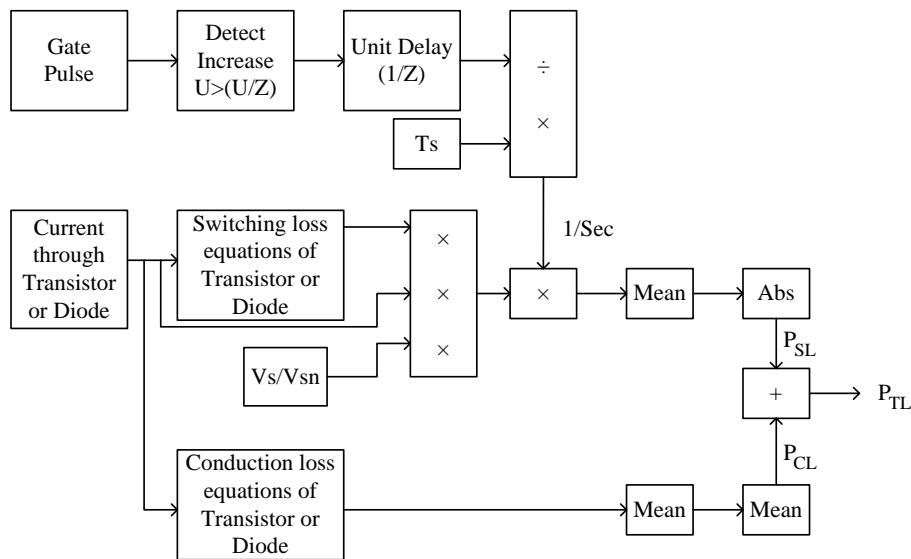


**Figure 5.1:** Generalized block diagram of power conversion loss analysis of IGBT device

and switching losses of IGBT switches. The conduction loss mainly depends on the conduction state of the IGBT switches, and the switching loss mainly depends on the ON and OFF state of the IGBT switches. The IGBT switch consists of a transistor and an antiparallel diode. Both the devices experience losses during the ON and OFF states. If the positive current is flowing through the switch, then the transistor gets shorted, or else an antiparallel diode is conducted for negative switch currents. The generalized power conversion loss equations of the transistor and antiparallel diode

are deduced from the 2<sup>nd</sup> order curve fitting of the IGBT switch datasheets (Drofenik and Kolar, 2005). In general, the transistor collector current,  $i_t$  or diode forward current,  $i_d$  is multiplied with the voltage between the collector and emitter directly from the IGBT switch datasheets to obtain the conduction loss. Hence, the conduction loss of the IGBT switch is given by:

$$P_{CL} = ci_{igbt} + di_{igbt}^2 \quad (5.1)$$

Where, c and d are the coefficients derived from the curve fitting. Based on the 2<sup>nd</sup> order approximations (Venkataramanaiah and Suresh, 2018), the above equation (5.1) for the transistor and diode can be written as:

$$\begin{aligned} P_{CL-t,25^\circ} &= -0.8995 + 1.551i_t + 0.02385i_t^2 \\ P_{CL-t,125^\circ} &= -2.452 + 1.914i_t + 0.02876i_t^2 \end{aligned} \quad (5.2)$$

$$\begin{aligned} P_{CL-d,25^\circ} &= -0.2321 + 1.245i_d + 0.01521i_d^2 \\ P_{CL-d,125^\circ} &= -0.8451 + 1.06i_d + 0.01485i_d^2 \end{aligned} \quad (5.3)$$

As the switching losses are dependent on temperature, the conduction losses are affected by the junction temperature, T. Therefore, the equations (5.2) and (5.3) can be re-written as:

$$\begin{aligned} P_{CL}(i_t, T) &= -(0.511375 + 0.015525T) + (1.46025 + 0.00363T)i_t \\ &\quad + (0.0224 + 0.000058T)i_t^2 \end{aligned} \quad (5.4)$$

$$P_{CL}(i_d, T) = -(0.0789 + 0.0061T) + (1.2913 - 0.0019T)i_d + (0.0153T)i_d^2 \quad (5.5)$$

The switching loss equations of the transistor and diode are expressed by:

$$P_{SL-t} = 170.3 + 3.224i_d - 0.03366i_d^2 + 0.0001487i_d^3 \quad (5.6)$$

$$P_{SL-d} = 65.53 - 0.436i_d - 0.0007726i_d^2 \quad (5.7)$$

The total power loss of the IGBT switch is given by:

$$P_{TL-igbt} = P_{CL}(i_t, T) + P_{CL}(i_d, T) + P_{SL-t} + P_{SL-d} \quad (5.8)$$

Generally, the switching losses of the diode are neglected. The voltage ratio ( $V_s/V_{sn}$ ) is multiplied with total energy to hold a good approximation in loss calculations.  $V_s$  is the operating voltage and  $V_{sn}$  is the maximum blocking voltage of the IGBT switch.

### 5.3 Overall Control Diagram of the Various Topologies of the Hybrid Micro-grid Systems

In Figure 5.2, the AC coupled hybrid micro-grid system consists of five converters, namely the DC-DC boost converter from the PV array to the DC bus, 3 $\phi$  4-leg DC-AC UIC from the DC bus to the AC bus, 3 $\phi$  AC-DC-AC converter from the PMSG variable wind turbine to the AC bus, and the 3 $\phi$  AC-DC and DC-DC boost converters from the AC bus to the DC resistive load.

In Figure 5.3, the DC coupled hybrid micro-grid system consists of four converters, namely the DC-DC boost converter from the PV array to the DC bus, 3 $\phi$  AC-DC and DC-DC boost converters from the PMSG variable wind turbine to the DC bus, and the 3 $\phi$  4-leg DC-AC BIC from the DC bus to the AC bus.

In Figure 5.4, the AC-DC coupled hybrid micro-grid system consists of three converters, namely the DC-DC boost converter from the PV array to the DC bus, 3 $\phi$  4-leg DC-AC BIC from the DC bus to the AC bus, and the 3 $\phi$  AC-DC-AC converter from the PMSG variable wind turbine to the AC bus.

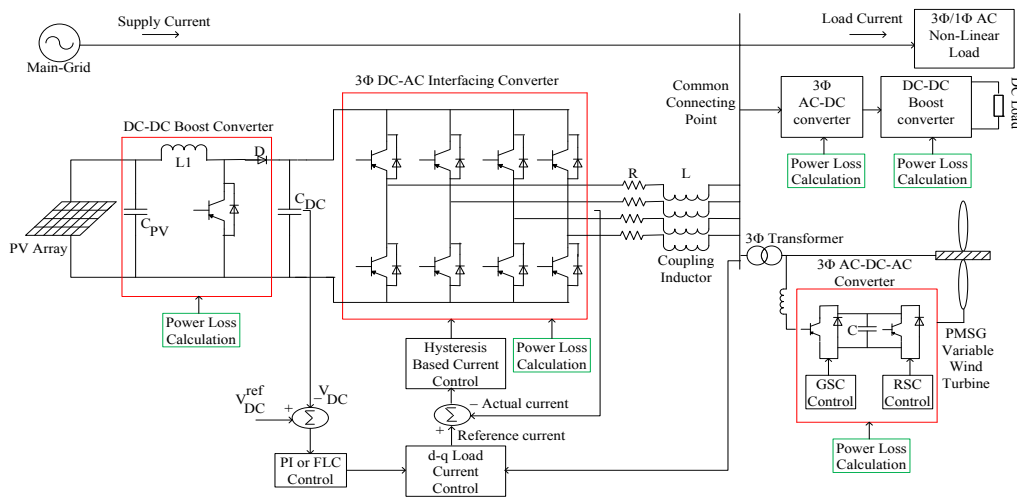


**Figure 5.2:** Overall control diagram of the AC CHM for power flow and conversion loss analysis

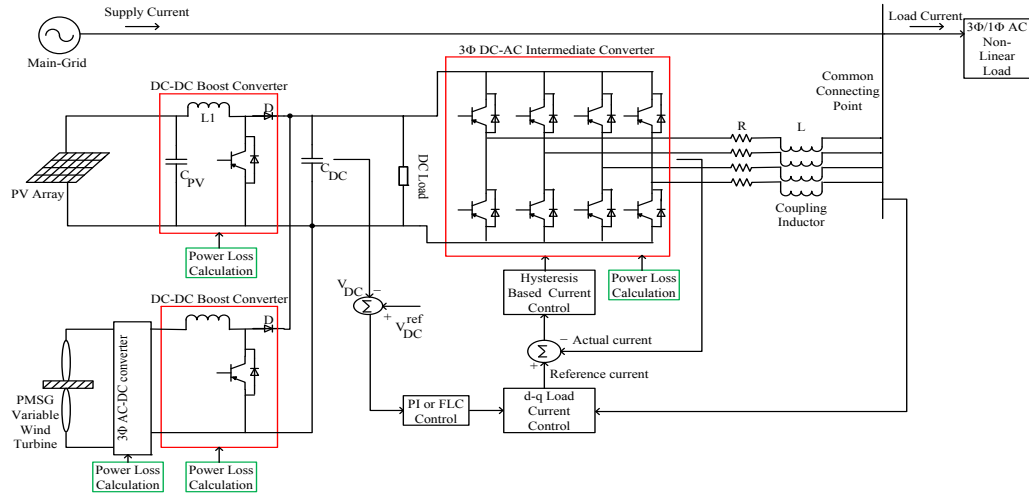


**Figure 5.3:** Overall control diagram of the DC CHM for power flow and conversion loss analysis

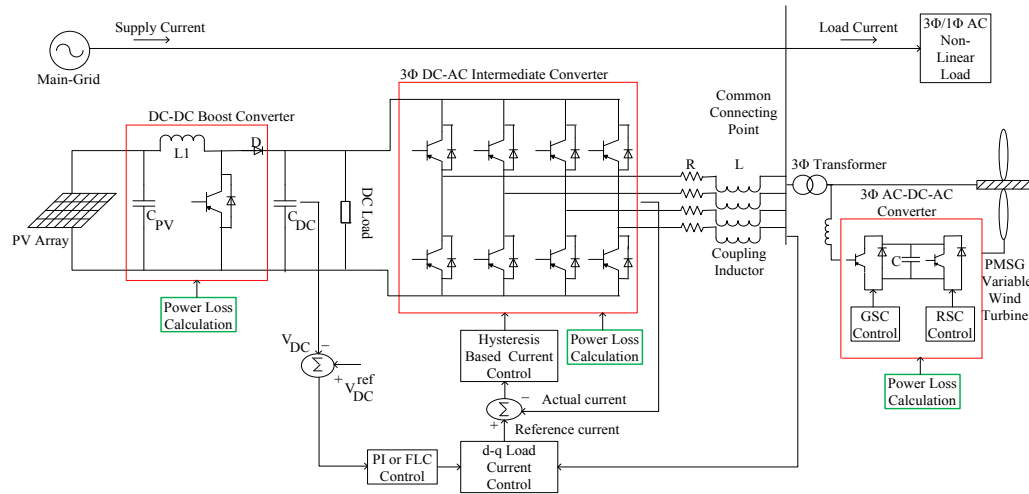


**Figure 5.4:** Overall control diagram of the AC-DC CHM for power flow and conversion loss analysis

## 5.4 Simulation Results

The MATLAB simulation is carried out for Figures 5.2– 5.4 using Figure 5.1. The simulation parameters used for all the topologies of the AC, DC, and AC-DC coupled hybrid micro-grid systems are the same. The performance analysis of power flow and conversion losses for the AC-DC coupled hybrid micro-grid system is compared with the individual AC and DC coupled hybrid micro-grid systems and validated for different case studies.

### 5.4.1 AC CHM (PMSG+PV) – Power flow balance and conversion losses under undistorted grid voltage conditions

In this case, the AC-DC-AC converter loss is 789 W, while converting the power from the PMSG wind to the AC grid side as shown in Figure 5.5(a). The UIC and boost converter losses of the PV array are 540 W and 117 W, as observed in Figure 5.5(b) and Figure 5.5(f). The AC and DC load AC-DC converter losses are 12 W and 530 W as shown in Figure 5.5(c) and Figure 5.5(d). The boost converter loss of the DC load is 92 W as shown in Figure 5.5(e). Therefore, the total power conversion loss of the AC coupled hybrid micro-grid system is 2080 W.

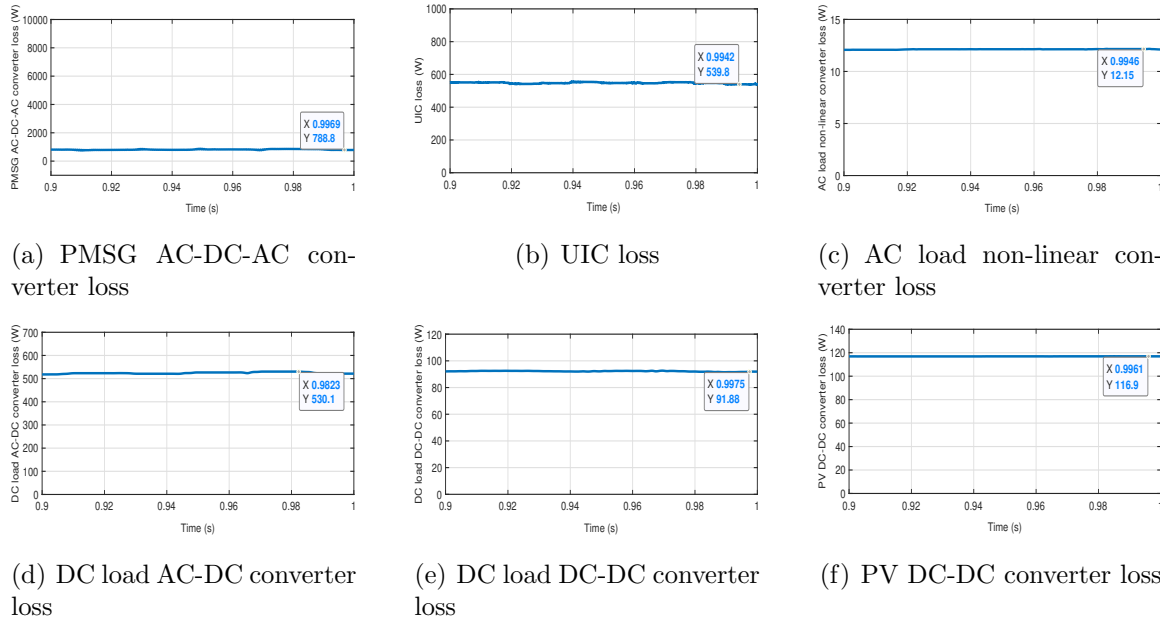
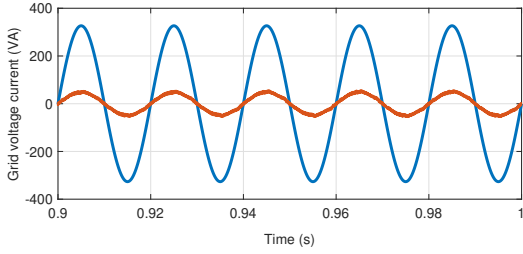


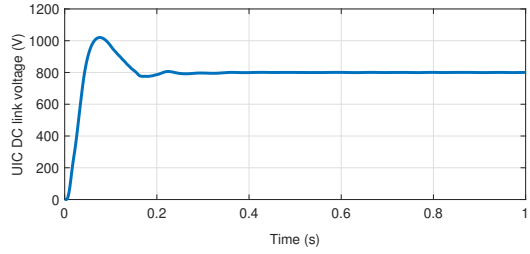
**Figure 5.5:** Power loss analysis of AC CHM with PMSG+PV under undistorted grid voltage

The  $P_{wind}$  generation of 30 kW at wind speed of 7 m/s and the  $P_{pv}$  generation of 3 kW at irradiation of 100 W/m<sup>2</sup> are less than the  $P_{acnon-linearload}$  of 17 kW and  $P_{dload}$  of 40 kW demands as shown in Figures 5.6(e)–5.6(h). Hence, the required deficit power of 24 kW is supplied by the  $P_{grid}$  to meet the load demands as shown in Figure 5.6(c). Therefore, the grid voltage is in phase with the grid current. To supply power to these loads, both the UICs had to operate in inverter mode as shown in Figure 5.6(d). Figure 5.6(a) and Figure 5.6(b) represents the grid voltage current and UIC DC link voltage, respectively.

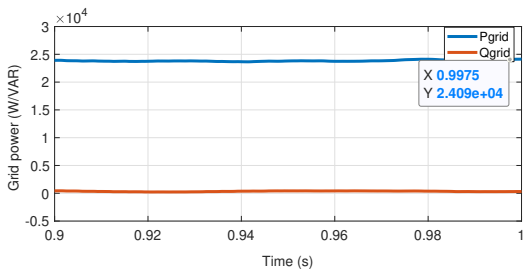




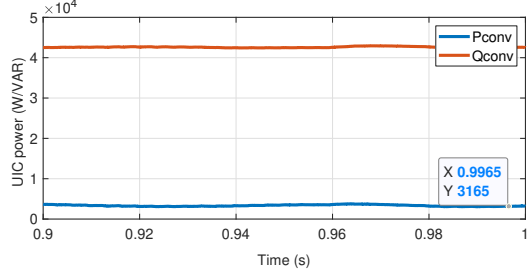
(a) Grid voltage current



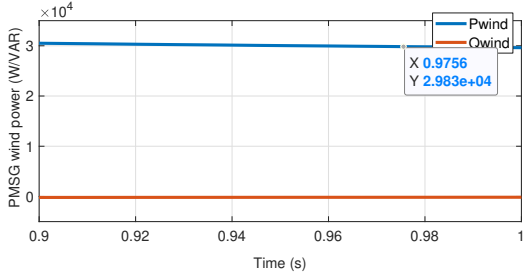
(b) UIC DC link voltage



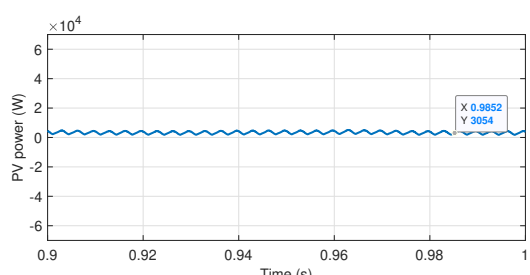
(c) Grid power



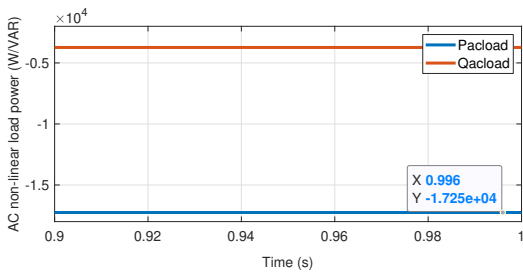
(d) UIC power



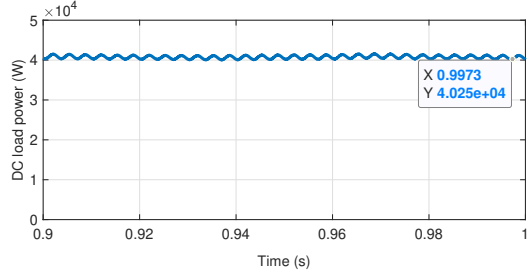
(e) PMSG wind power



(f) PV power



(g) AC Non-linear load power



(h) DC load power

**Figure 5.6:** Power flow analysis of AC CHM with PMSG+PV under undistorted grid voltage

### 5.4.2 AC CHM (PMSG+PV) – Power flow balance and conversion losses under distorted grid voltage conditions

In this case, the AC-DC-AC converter loss is 714 W, while converting power from the PMSG wind to the AC grid side as shown in Figure 5.7(a). The UIC and boost converter losses of the PV array are 500 W and 7 W, as observed in Figure 5.7(b) and Figure 5.7(f). The AC and DC load AC-DC converter losses are 50 W and 1381 W as shown in Figure 5.7(c) and Figure 5.7(d). The boost converter loss of the DC load is 254 W as shown in Figure 5.7(e). Therefore the total power conversion loss of the AC coupled hybrid micro-grid system is 2906 W.

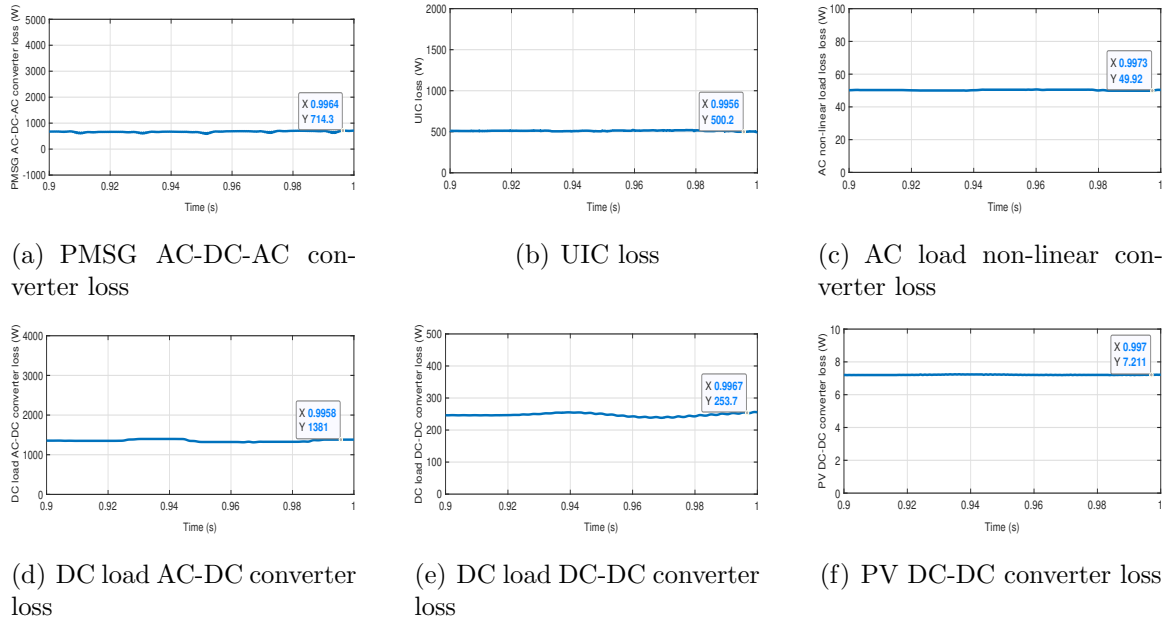
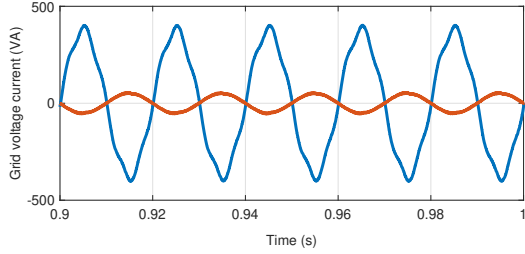
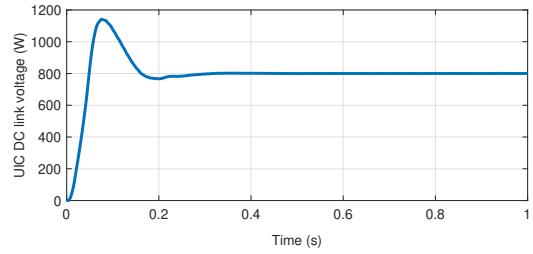


**Figure 5.7:** Power loss analysis of AC CHM with PMSG+PV under distorted grid voltage

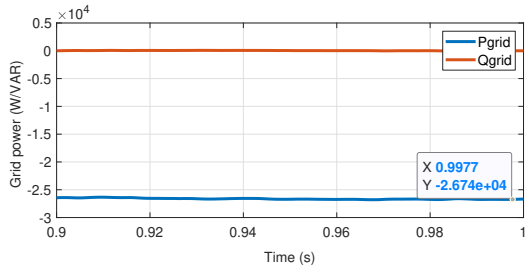
The  $P_{wind}$  generation of 34 kW at wind speed of 8 m/s and the  $P_{pv}$  generation of 32 kW at irradiation of 800 W/m<sup>2</sup> are more than the  $P_{acnon-linearload}$  of 14 kW and  $P_{dcload}$  of 25 kW demands as shown in Figures 5.8(e)–5.8(h). Hence, the remaining surplus power of 27 kW is injected into the  $P_{grid}$  as shown in Figure 5.8(c). Therefore, the grid voltage is in phase opposition with the grid current. To supply power to these loads, both the UICs had to operate in inverter mode as shown in Figure 5.8(d). Figure 5.8(a) and Figure 5.8(b) represents the grid voltage current and UIC DC link voltage, respectively.



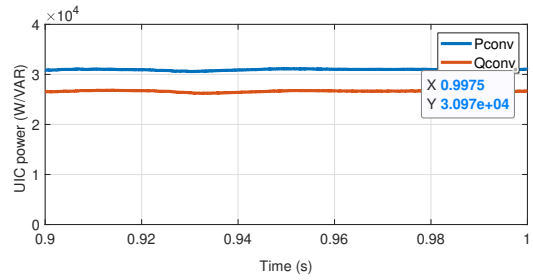
(a) Grid voltage current



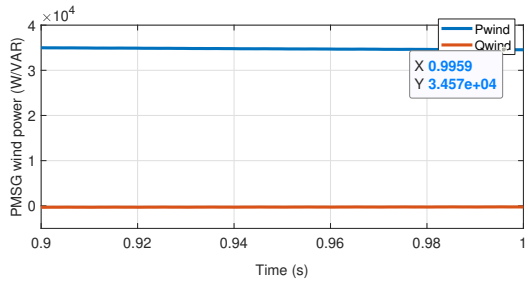
(b) UIC DC link voltage



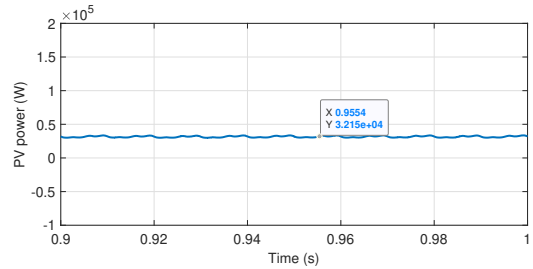
(c) Grid power



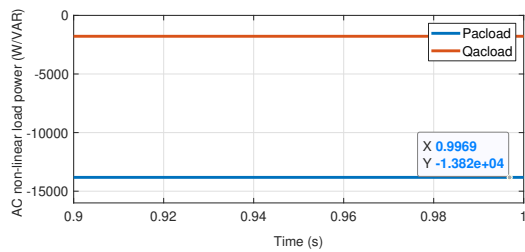
(d) UIC power



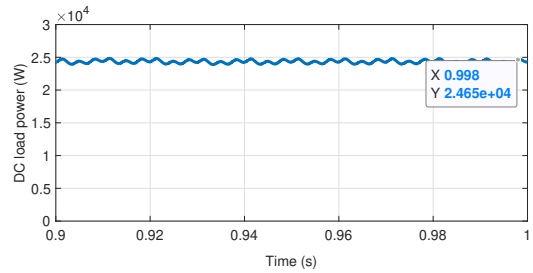
(e) PMSG wind power



(f) PV power



(g) AC Non-linear load power



(h) DC load power

**Figure 5.8:** Power flow analysis of AC CHM with PMSG+PV under distorted grid voltage

### 5.4.3 DC CHM (PMSG+PV) – Power flow balance and conversion losses under undistorted grid voltage conditions

In this case, the AC-DC converter loss of the PMSG wind is 807 W, while converting power to the DC bus as shown in Figure 5.9(a). The BIC loss is 45 W, while transferring power to the DC grid side as shown in Figure 5.9(b). The AC-DC converter loss of the AC load is 77 W as shown in Figure 5.9(c). The boost converter losses of the PMSG wind and PV array are 247 W and 7 W, as observed in Figure 5.9(d). Therefore, the total power conversion loss of the DC coupled hybrid micro-grid system is 1183 W.

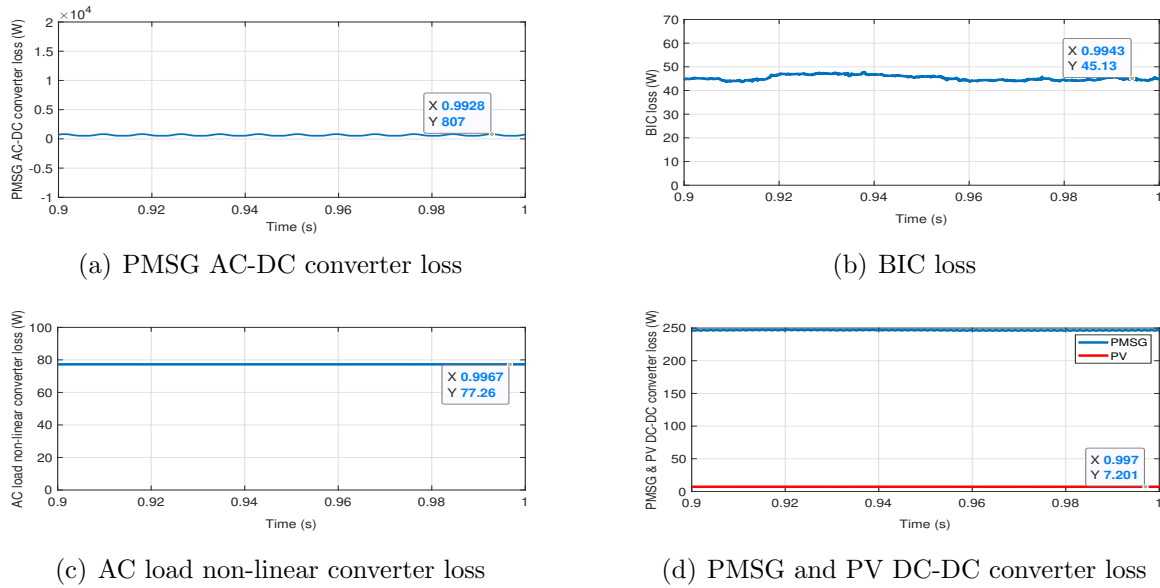
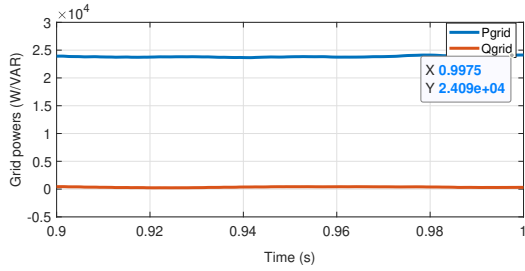
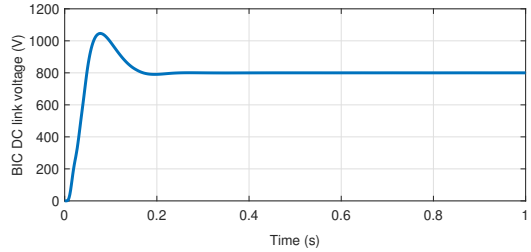


**Figure 5.9:** Power loss analysis of DC CHM with PMSG+PV under undistorted grid voltage

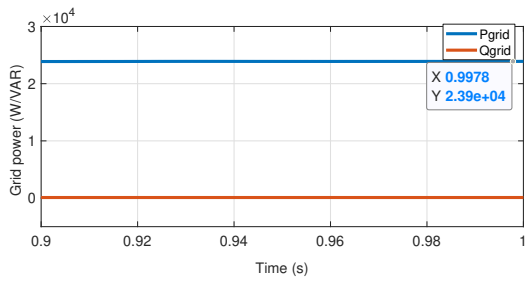
The  $P_{wind}$  generation of 30 kW at wind speed of 7 m/s and the  $P_{pv}$  generation of 3 kW at irradiation of 100 W/m<sup>2</sup> are less than the  $P_{acnon-linearload}$  of 17 kW and  $P_{dload}$  of 40 kW demands as shown in Figures 5.10(e)–5.10(h). Hence, the required deficit power of 24 kW is supplied by the  $P_{grid}$  to meet the load demands as shown in Figure 5.10(c). Therefore, the grid voltage is in phase with the grid current. To satisfy the DC load demand, the BIC acted as a rectifier as shown in Figure 5.10(d). Figure 5.10(a) and Figure 5.10(b) represents the grid voltage current and BIC DC link voltage, respectively.



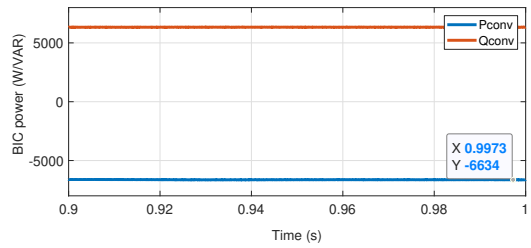
(a) Grid voltage current



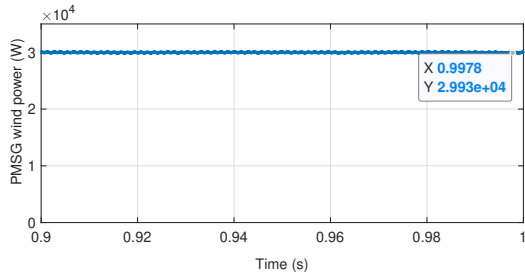
(b) BIC DC link voltage



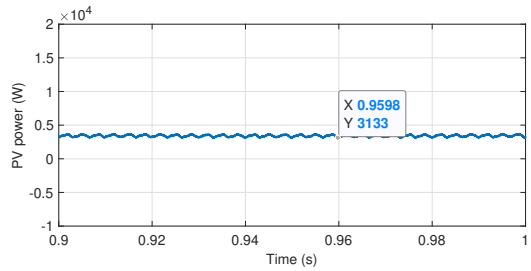
(c) Grid power



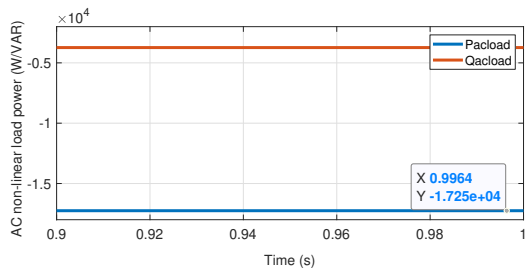
(d) BIC power



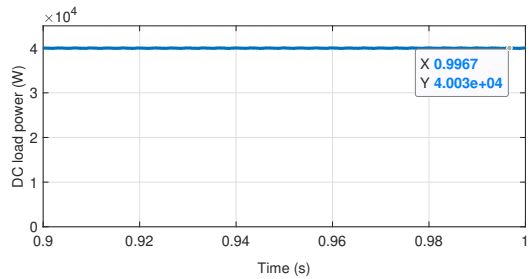
(e) PMSG wind power



(f) PV power



(g) AC Non-linear load power



(h) DC load power

**Figure 5.10:** Power flow analysis of DC CHM with PMSG+PV under undistorted grid voltage

#### 5.4.4 DC CHM (PMSG+PV) – Power flow balance and conversion losses under distorted grid voltage conditions

In this case, the AC-DC converter loss of the PMSG wind is 533 W, while converting power to the DC bus as shown in Figure 5.11(a). The BIC loss is 703 W, while transferring power to the AC grid side as shown in Figure 5.11(b). The AC-DC converter loss of the AC load is 10 W as shown in Figure 5.11(c). The boost converter losses of the PMSG wind and PV array are 296 W and 117 W, as observed in Figure 5.11(d). Therefore the total power conversion loss of the DC coupled hybrid micro-grid system is 1659 W.

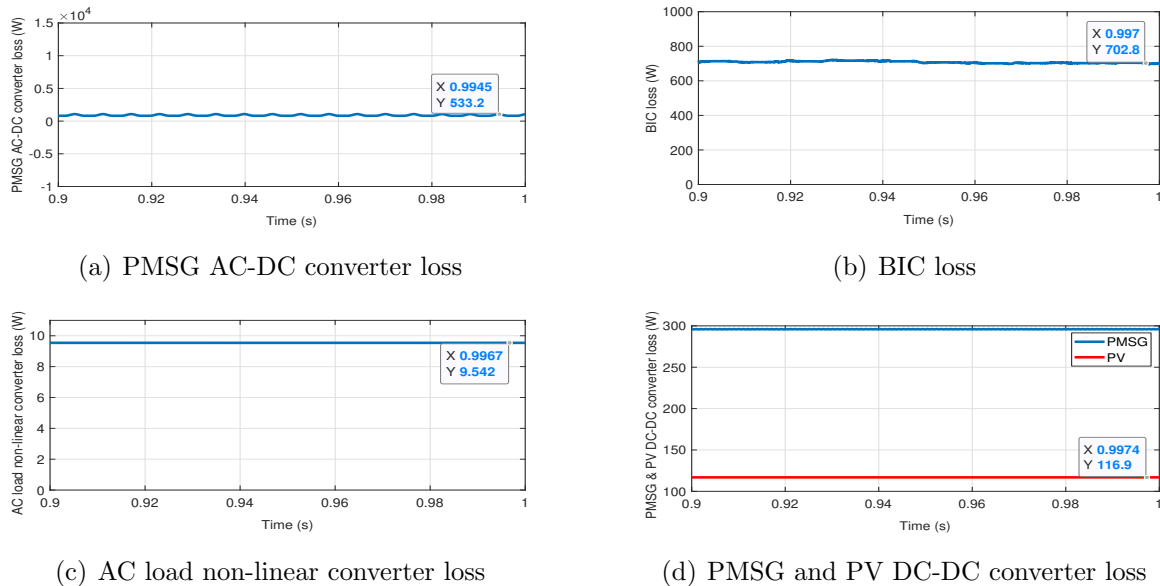
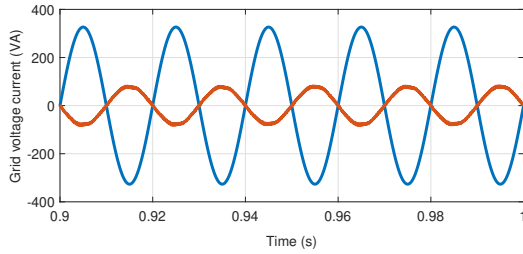
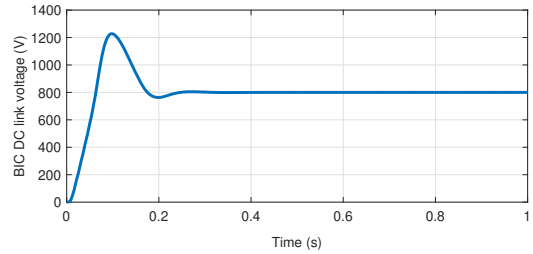


**Figure 5.11:** Power loss analysis of DC CHM with PMSG+PV under distorted grid voltage

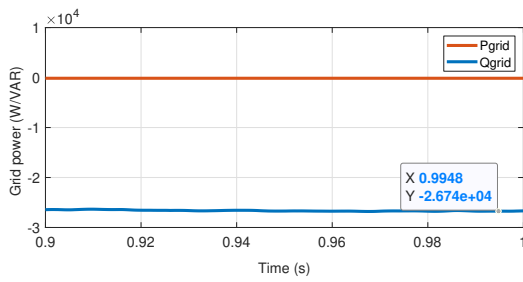
The  $P_{wind}$  generation of 34 kW at wind speed of 8 m/s and the  $P_{pv}$  generation of 32 kW at irradiation of 800 W/m<sup>2</sup> are more than the  $P_{acnon-linearload}$  of 14 kW and  $P_{dload}$  of 25 kW demands are shown in Figures 5.12(e)–5.12(h). Hence, the remaining surplus power of 27 kW is injected into the  $P_{grid}$  as shown in Figure 5.12(c). Therefore, the grid voltage is in phase opposition with the grid current. To transfer the surplus power of the  $P_{pv}$  to the AC grid side, the BIC acted as an inverter as shown in Figure 5.12(d). Figure 5.12(a) and Figure 5.12(b) represents the grid voltage current and BIC DC link voltage, respectively.



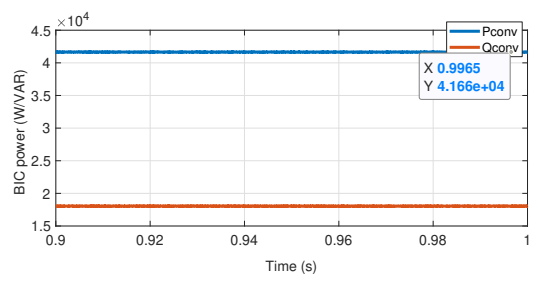
(a) Grid voltage current



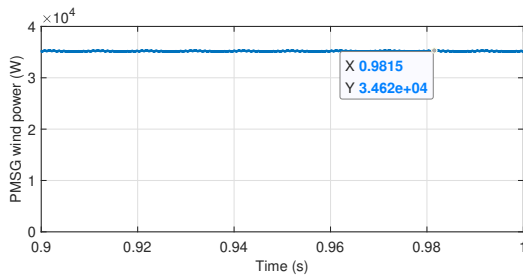
(b) BIC DC link voltage



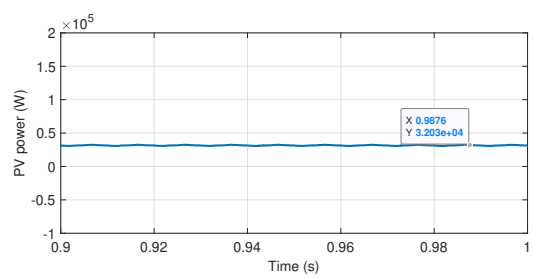
(c) Grid power



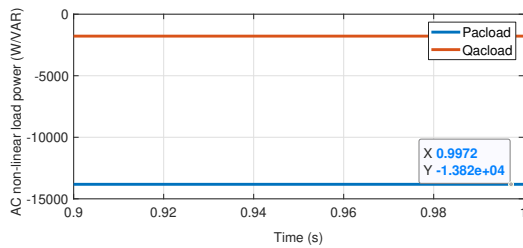
(d) BIC power



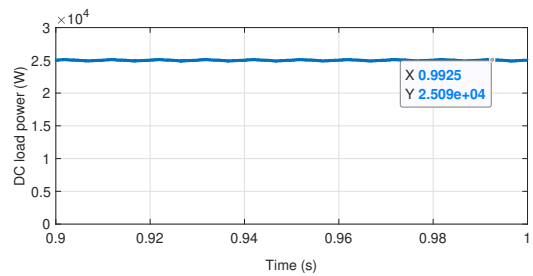
(e) PMSG wind power



(f) PV power



(g) AC Non-linear load power



(h) DC load power

**Figure 5.12:** Power flow analysis of DC CHM with PMSG+PV under distorted grid voltage

### 5.4.5 AC-DC CHM (PMSG+PV) – Power flow balance and conversion losses under undistorted grid voltage conditions

In this case, the AC-DC-AC converter loss of the PMSG wind is 362 W, while converting power to the AC bus as shown in Figure 5.13(a). The BIC loss is 360 W, while transferring power to meet the DC load demand as shown in Figure 5.13(b). The AC-DC converter loss of the AC load is 22 W as shown in Figure 5.13(c). The boost converter loss of the PV array is 7 W, as observed in Figure 5.13(d). Therefore the total power conversion loss of the AC-DC coupled hybrid micro-grid system is 751 W.

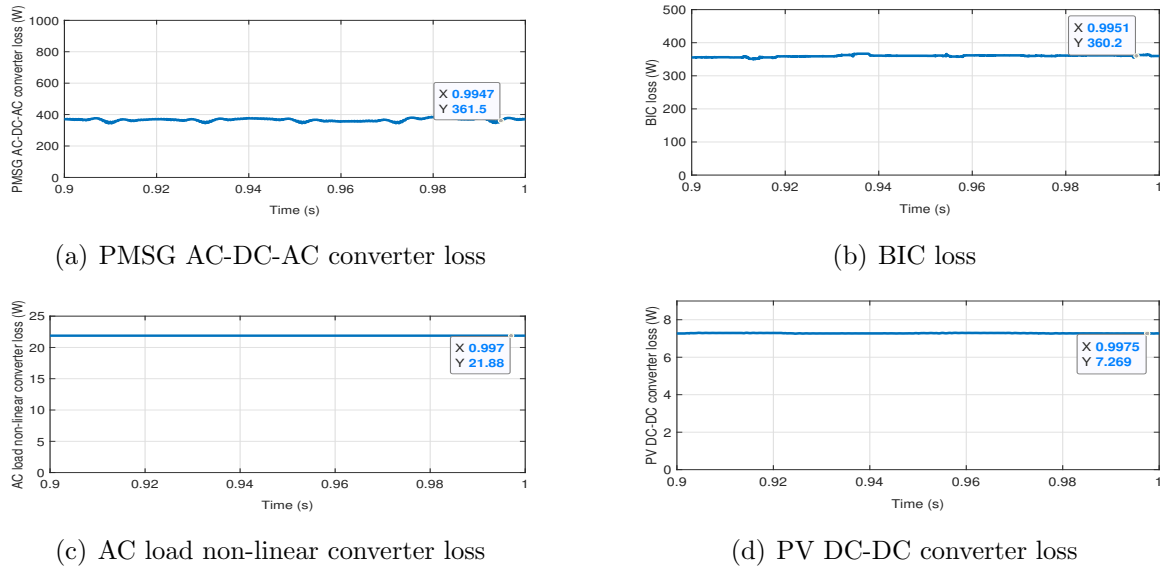
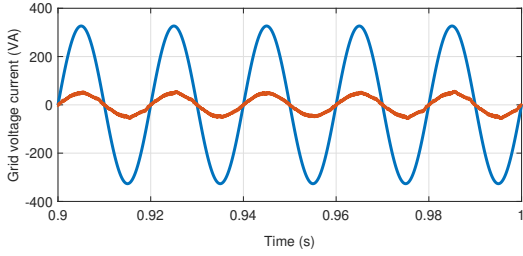


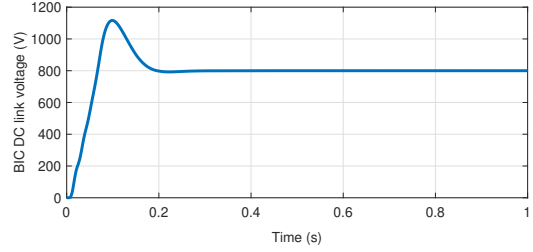
**Figure 5.13:** Power loss analysis of AC-DC CHM with PMSG+PV under undistorted grid voltage

The  $P_{wind}$  generation of 30 kW at wind speed of 7 m/s and the  $P_{pv}$  generation of 3 kW at irradiation of 100 W/m<sup>2</sup> are less than the  $P_{acnon-linearload}$  of 17 kW and  $P_{dload}$  of 40 kW demands as shown in Figures 5.14(e)–5.14(h). Hence, the required deficit power of 24 kW is supplied by the  $P_{grid}$  to meet the load demands as shown in Figure 5.14(c). Therefore, the grid voltage is in phase with the grid current. To satisfy the DC load demand, the BIC acted as a rectifier as shown in Figure 5.14(d). Figure 5.14(a) and Figure 5.14(b) represents the grid voltage current and BIC DC link voltage, respectively.

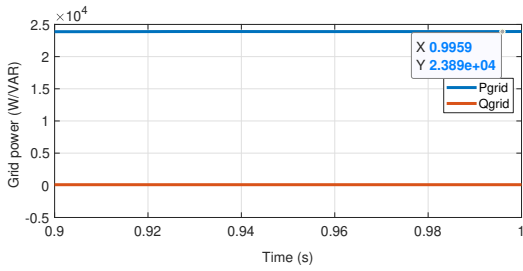




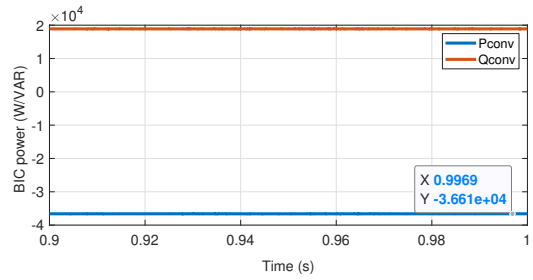
(a) Grid voltage current



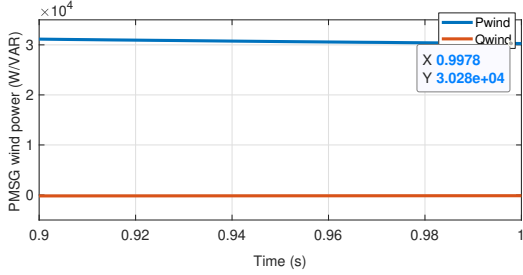
(b) BIC DC link voltage



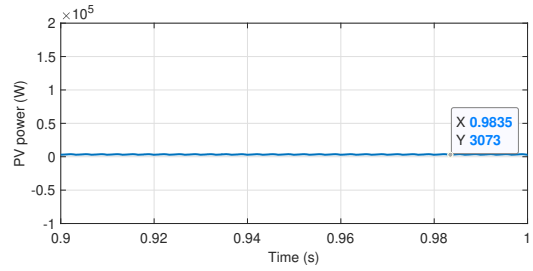
(c) Grid power



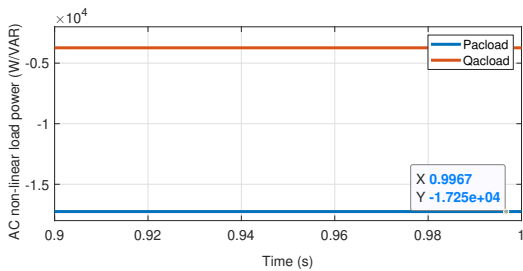
(d) BIC power



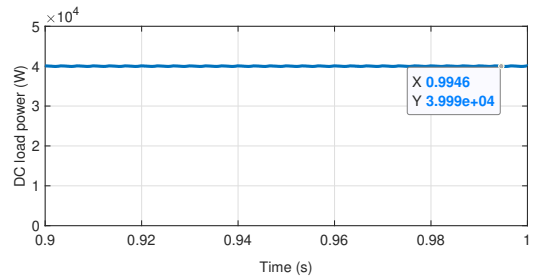
(e) PMSG wind power



(f) PV power



(g) AC Non-linear load power



(h) DC load power

**Figure 5.14:** Power flow analysis of AC-DC CHM with PMSG+PV under undistorted grid voltage

### 5.4.6 AC-DC CHM (PMSG+PV) – Power flow balance and conversion losses under distorted grid conditions

In this case, the AC-DC-AC converter loss of the PMSG wind is 793 W, while converting power to the AC bus as shown in Figure 5.15(a). The BIC loss is 106 W, while transferring power to the AC grid side as shown in Figure 5.15(b). The AC-DC converter loss of the AC load is 19 W as shown in Figure 5.15(c). The boost converter loss of the PV array is 117 W, as observed in Figure 5.15(d). Therefore, the total power conversion loss of the AC-DC coupled hybrid micro-grid system is 1035 W.

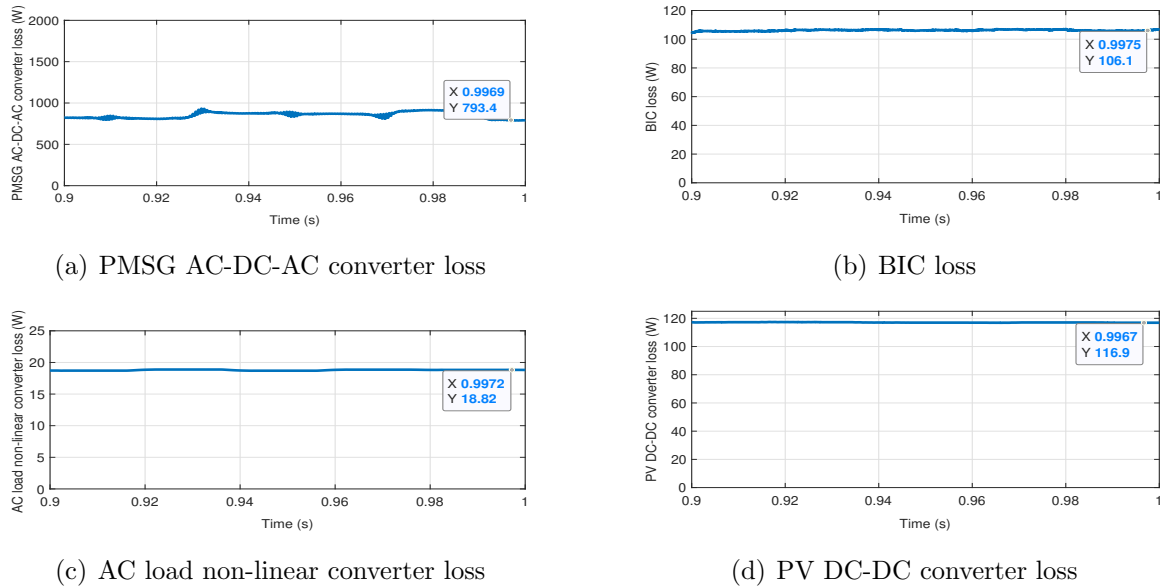
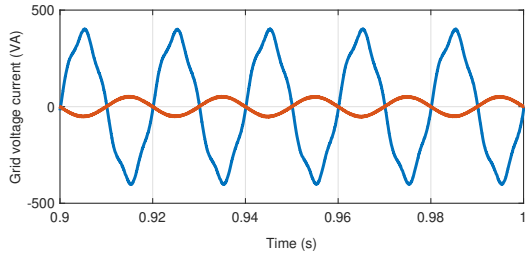
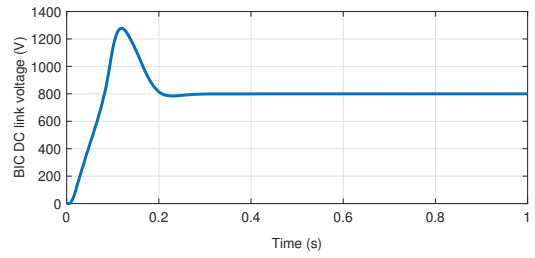


**Figure 5.15:** Power loss analysis of AC-DC CHM with PMSG+PV under distorted grid voltage

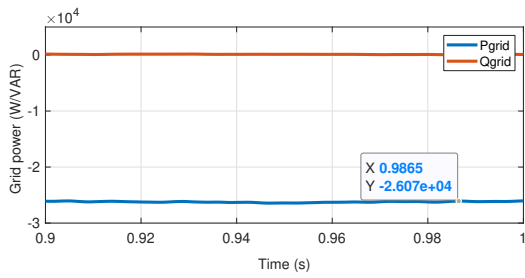
The  $P_{wind}$  generation of 34 kW at wind speed of 8 m/s and the  $P_{pv}$  generation of 32 kW at irradiation of 800 W/m<sup>2</sup> are more than the  $P_{acnon-linearload}$  of 14 kW and  $P_{dload}$  of 25 kW demands as shown in Figures 5.16(e)–5.16(h). Hence, the remaining surplus power of 27 kW is injected into the  $P_{grid}$  as shown in Figure 5.16(c). Therefore, the grid voltage is in phase opposition with the grid current. To transfer the surplus power of the PV array,  $P_{pv}$  to the AC grid side, the BIC acted as an inverter as shown in Figure 5.16(d). Figure 5.16(a) and Figure 5.16(b) represents the grid voltage current and BIC DC link voltage, respectively.



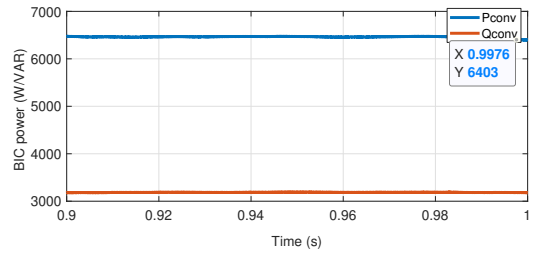
(a) Grid voltage current



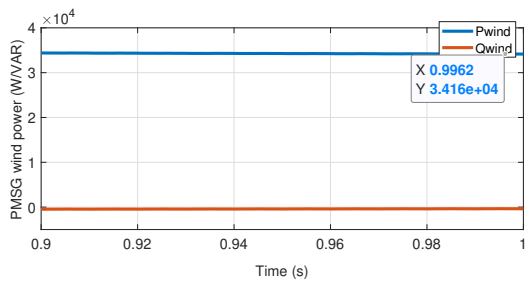
(b) BIC DC link voltage



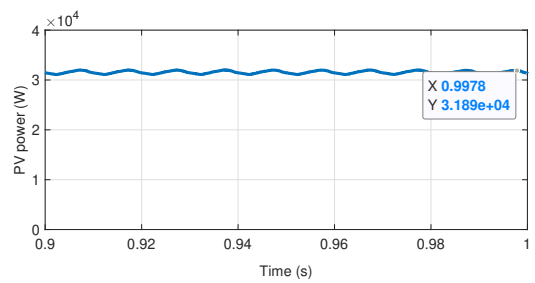
(c) Grid power



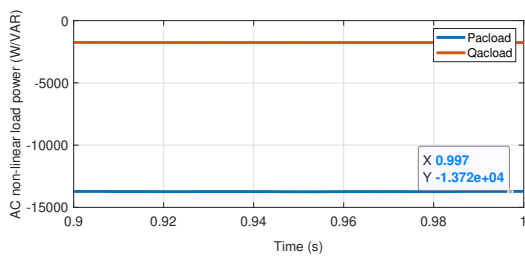
(d) BIC power



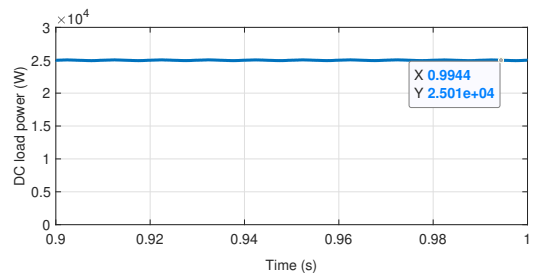
(e) PMSG wind power



(f) PV power



(g) AC Non-linear load power



(h) DC load power

**Figure 5.16:** Power flow analysis of AC-DC CHM with PMSG+PV under distorted grid voltage

## 5.5 Summary

- The same parameters of  $P_{wind}= 30$  kW,  $P_{pv}= 3$  kW,  $P_{acnon-linearload}= 17$  kW and  $P_{dload}= 40$  kW were used for the power flow and loss analysis of all the AC, DC, and the AC-DC coupled hybrid micro-grid systems under undistorted grid voltage conditions.
- The same parameters of  $P_{wind}= 34$  kW,  $P_{pv}= 32$  kW,  $P_{acnon-linearload}= 14$  kW, and  $P_{dload}= 25$  kW were used for the power flow and loss analysis of all the AC, DC, and the AC-DC coupled hybrid micro-grid systems under distorted grid voltage conditions.
- The MATLAB simulation was carried out by considering the variation of RES under different grid voltage scenarios. The power flow balance equations for all the case scenarios were shown below,

- (a) In Section 5.4.1 with (PMSG+PV) RES, the UIC acted as an inverter. Thus, the power flow balance equation is:

$$P_{pv} + P_{wind} + P_{grid} = P_{acnon-linearload} + P_{dload}$$

- (b) In Section 5.4.2 with (PMSG+PV) RES, the UIC acted as an inverter. Thus, the power flow balance equation is:

$$P_{pv} + P_{wind} = P_{grid} + P_{acnon-linearload} + P_{dload}$$

- (c) In Section 5.4.3 with (PMSG+PV) RES, the BIC acted as a rectifier. Therefore, the power flow balance equations at the DC grid side and the AC grid side are:

$$P_{pv} + P_{wind} + P_{conv} = P_{dload}$$

$$P_{grid} = P_{acnon-linearload}$$

- (d) In Section 5.4.4 with (PMSG+PV) RES, the BIC acted as an inverter. Therefore, the power flow balance equations at the DC grid side and the AC grid side are:

$$P_{pv} + P_{wind} = P_{dload}$$

$$P_{conv} = P_{grid} + P_{acnon-linearload}$$

- (e) In Section 5.4.5 with (PMSG+PV) RES, the BIC acted as a rectifier. Therefore, the power flow balance equations at the DC bus and the AC bus are:

$$P_{pv} + P_{conv} = P_{dload}$$

$$P_{wind} + P_{grid} = P_{acnon-linearload}$$

- (f) In Section 5.4.6 with (PMSG+PV) RES, the BIC acted as an inverter. Therefore, the power flow balance equations at the DC bus and the AC bus are:

$$P_{pv} = P_{dload}$$

$$P_{conv} + P_{wind} = P_{grid} + P_{acnon-linearload}$$

- From Sections 5.4.1 to 5.4.6, the obtained results with PMSG+PV using the MATLAB Simulink prove that the power conversion losses were reduced with the AC-DC coupled hybrid micro-grid system over individual AC and DC coupled hybrid micro-grid systems and are summarized in Table 5.1.

**Table 5.1:** Comparison of the power conversion losses for AC-DC CHM over the AC and DC CHM systems

Case	Total power conversion losses for AC CHM system in Watts	Total power conversion losses for DC CHM system in Watts	Total power conversion losses for AC-DC CHM system in Watts
a) PMSG+PV RES under undistorted grid voltage	2080	1183	751
b) PMSG+PV RES under distorted grid voltage	2906	1659	1035



# Chapter 6

## Conclusion and Future Work

### 6.1 Conclusion

Micro-grids are formulated as an enticing way to incorporate DGs or RES into the main-grid. The approach would lead to a reduction in the burden on fossil fuel and improvement in the efficiency of the main-grid. While most of the literature studies focus on individual AC and DC coupled hybrid micro-grid systems, the AC-DC coupled hybrid micro-grid system is an interesting approach as they merge the benefits of the two previous topologies. The present thesis has identified and examined the most important features of the hybrid micro-grid topologies. The general conclusions of each chapter are as follows:

In Chapter 1, the various topologies of the hybrid micro-grid systems, namely the AC coupled, DC coupled, and AC-DC coupled were reviewed. The issues related to power flow and power quality were discussed. To overcome these issues, appropriate control methods were also discussed. A summary of the work and the contents of the chapters that follow are presented.

In Chapter 2, a suitable SAPF based proposed d-q load current control was developed by comparing with SAPF based conventional p-q load current control. The results obtained in the MATLAB Simulink proved that the proposed d-q load current control works well for any grid and load conditions. This controller was designed for both unidirectional as well as bi-directional power flow. The overall control of the AC coupled hybrid micro-grid system was presented. Further, the modeling of the PV array, PMSG, and DFIG variable wind turbine were discussed. Furthermore, the design of the various converters involved was also discussed. The proposed d-q load

current control was applied to the UIC of the AC coupled hybrid micro-grid system to regulate the real and reactive power as well as the harmonic currents mitigation simultaneously. The performance of the proposed d-q load current control based PI and FLC was analyzed using the MATLAB Simulink. This control technique was validated for different grid and load case scenarios with variation of PV array and PMSG or DFIG variable wind turbine RES.

Chapter 3 presented the overall control of the DC coupled hybrid micro-grid system. The BIC controlled by the d-q load current control based-PI and FLC has been discussed in Chapter 2. This d-q load current control based-PI and FLC performs active power flow with current harmonics mitigation effectively,

- If the DC load demand is greater than the generation of PV array and PMSG variable wind turbine RES, the BIC acts as a rectifier.
- If the DC load demand is lesser than the generation of PV array and PMSG variable wind turbine RES, the BIC acts as an inverter.

In Chapter 4, based on the benefits of the individual AC and DC coupled hybrid micro-grid systems, the AC-DC coupled hybrid micro-grid system was proposed in the present research work. The performance of the proposed d-q load current control applied to the BIC was analyzed in the MATLAB Simulink. This results in the inverter-based and rectifier-based power flow exchange between the AC and DC bus with acceptable current harmonics as per IEEE 519 standards,

- If the generation of PV array is more than the DC load demand, the BIC acts as an inverter.
- If the generation of PV array is less than the DC load demand, the BIC acts as a rectifier.

For all the topologies of the AC, DC, and AC-DC coupled hybrid micro-grid, the obtained grid current THD was improved with the d-q load current control based-FLC over d-q load current control based PI as per the IEEE 519 standards.

Chapter 5 presented the methodology for the calculation of the generalized power conversion loss. The overall control of the AC, DC, and AC-DC coupled hybrid microgrid topologies for power flow and conversion loss analysis was discussed. The performance analysis of power flow and conversion losses for the AC-DC coupled hybrid micro-grid system was compared with the individual AC and DC coupled hybrid



micro-grid systems using the MATLAB Simulink for different case studies. The obtained results proved that the power conversion losses were reduced with the AC-DC coupled hybrid micro-grid system over the individual AC and DC coupled hybrid micro-grid systems.

Based on the present dominated AC power system, the proposed AC-DC CHM system faces more practical problems, while integrating with the main-grid. But the proposed system has good scope in the near future to fulfil the customer's load demand, especially in India and China.

## 6.2 Future Work

The future scope of this research work can be extended to study,

- The methodology for reliability issues due to interfaces of more converters in the AC-DC coupled hybrid micro-grid system;
- The control methods for parallel intermediate converters to increase the reliability of the AC-DC coupled hybrid micro-grid system;
- The control algorithms for protection issues in the AC-DC coupled hybrid micro-grid system; and
- The proper co-ordination control strategies for power quality and power flow management for an isolated system.



# Appendix A

## Generalized Curve Fitting Approach for IGBT Device

As stated in Chapter 5, the generalized curve fitting approach is highly accurate and can be directly deployed in any circuit simulator. The conduction loss and switching loss equations from equations (5.1) to (5.7) are derived from this approach, which estimates total losses of the IGBT switch with little effort using the equation (5.8). Such loss calculations are based on switch datasheet values, and the converters presented in Chapters 2, 3 and 4 were constructed using the SKM75GB123D-IGBT as shown in Figure A.1. For further explanation, the SKM75GB123D datasheet details are considered.

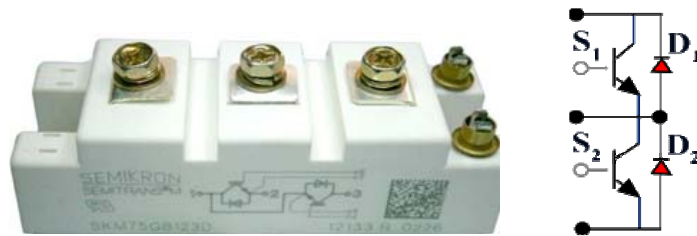


Figure A.1: SKM75GB123D IGBT switch under consideration

### A.1 Conduction Losses of the IGBT Switch

Conduction losses are usually determined by representing the forward voltage drop and a leakage current dependence with an ideal switch in series. Although this

method can only be modeled in the circuit simulator, the diodes and ideal switches are overloaded with additional parameters. In addition, the circuit simulator must accommodate controllable resistors to construct the temperature-dependent properties. Therefore, we followed a specific procedure described in (Drofenik and Kolar, 2005).

### A.1.1 Transistor-conduction power loss calculation ( $P_{CL-t}$ )

The selected SKM75GB123D IGBT switch data-sheet presents characteristic curves at different gate-emitter ( $V_{ge}$ ) values between the collector-emitter voltage ( $V_{ce}$ ) and collector-current ( $i_t$ ) of transistor. In addition, as shown in Figure A.2, the datasheet presented  $V_{ce} - i_t$  curves for minimum and maximum temperatures [ $T_{min} = 25^{\circ}\text{C}$  and  $T_{max} = 125^{\circ}\text{C}$ ] to illustrate the temperature dependence individually.

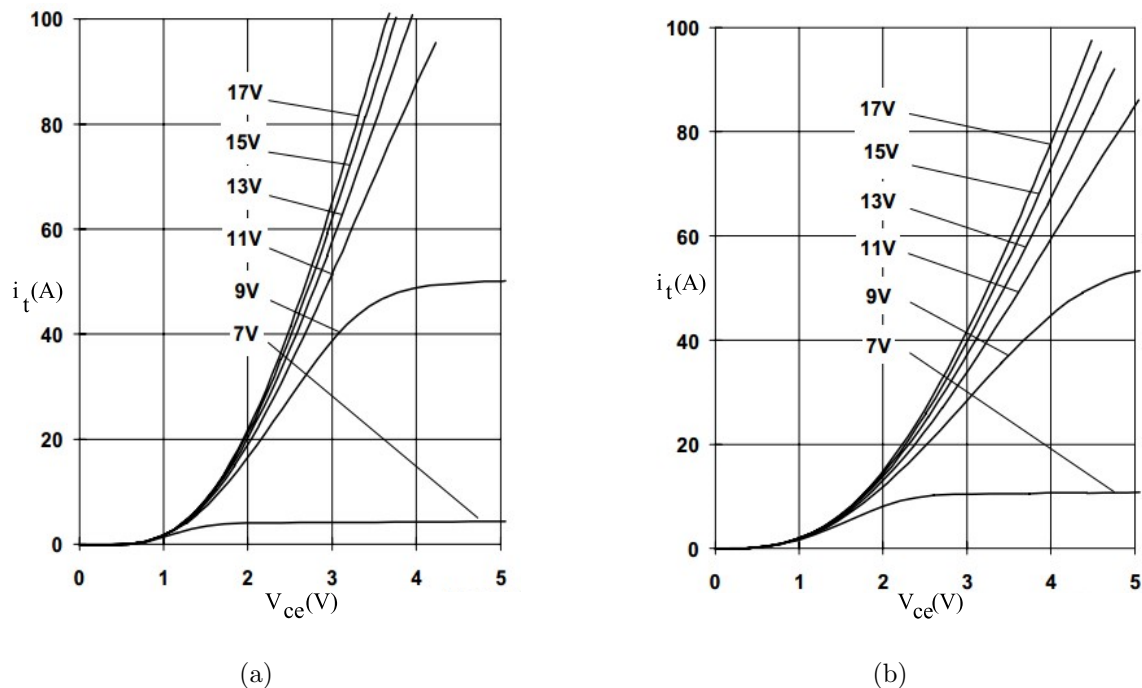


**Figure A.2:** SKM75GB123D transistor characteristic curves: a)  $T_{min} = 25^{\circ}\text{C}$  and b)  $T_{max} = 125^{\circ}\text{C}$

In fact, the potential voltage of the experimental gate-emitter  $V_{ge} = 15\text{ V}$ . Therefore, Figure A.2(a) extracts only one  $V_{ce} - i_t$  curve data and is listed in Table A.1. Later, multiply the  $V_{ce}$  with  $i_t$  to achieve the power at each extracted point. The

**Table A.1:**  $V_{ce}$ - $i_t$  curve extracted points for  $V_{ge} = 15$  V at  $T_{min} = 25^{\circ}\text{C}$

$V_{ce}$ (V)	$i_t$ (A)	$P_{CL-t,25^{\circ}\text{C}} = (V_{ce} \times i_t)$ (W)
0	0	0
1	1.4286	1.4286
1.5	8.5714	12.8571
2	21.4286	42.8572
2.5	40	100
3	62.1429	186.4287
3.5	82.8571	289.999

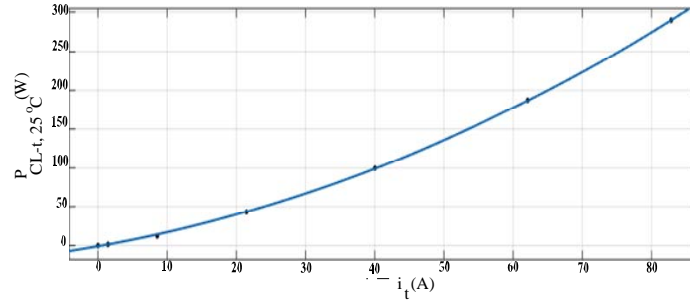


**Figure A.3:** Curve fitting waveform for transistor-conduction power loss at  $25^{\circ}\text{C}$  with respect to  $i_t$

prime motivation behind this mechanism is to estimate the power loss in terms of the transistor-collector current  $i_t$ . To achieve this mechanism,  $P_{CL-t,25^{\circ}\text{C}}$  versus  $i_t$  waveform is developed by using MATLAB curve fitting application. Based on the X and Y axis data, vary the polynomial order until error gets the minimum value. The presented data has arrived a minimum error at  $2^{nd}$  order polynomial equation. Thereby the waveform shown in Figure A.3 at  $25^{\circ}\text{C}$  is finalized, and the corresponding power loss equation is given by,

$$P_{CL-t,25^{\circ}\text{C}} = -0.8995 + 1.551i_t + 0.02385i_t^2 \quad (\text{A.1})$$

Similarly, Figure A.4 at  $125^{\circ}\text{C}$  is drawn based on the Table A.2. Therefore, the corresponding power loss equation is given by,

$$P_{CL-t,125^{\circ}\text{C}} = -2.452 + 1.914i_t + 0.02876i_t^2 \quad (\text{A.2})$$

The coefficients must describe the running temperature (T) to establish the temper-

**Table A.2:**  $V_{ce}$ - $i_t$  curve extracted points for  $V_{ge} = 15$  V at  $T_{min} = 125^\circ\text{C}$

$V_{ce}$ (V)	$i_t$ (A)	$P_{CL-t,125^\circ\text{C}} = (V_{ce} \times i_t)$ (W)
0	0	0
1	2.1429	2.1429
1.5	5.7143	8.5714
2	14.2857	28.5714
2.5	25.7149	64.2873
3	40	120
3.5	55.7143	195.0001
4	72.8571	291.4284
4.5	91.4286	411.4287

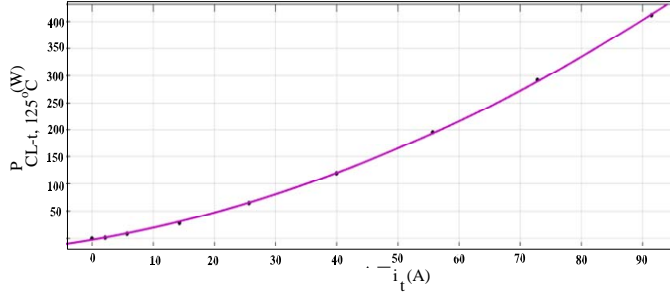


**Figure A.4:** Curve fitting waveform for transistor-conduction power loss at  $125^\circ\text{C}$  with respect to  $i_t$

ature dependence in the transistor-conduction power loss equation. The generalized temperature-dependent conduction power loss equation of second order is illustrated by,

$$P_{CL}(i_t, T) = (c_0 + c_1T) + (b_0 + b_1T)i_t + (a_0 + a_1T)i_t^2 \quad (\text{A.3})$$

The above equation A.3 is derived from the equations A.1 and A.2. Thus, the coefficients matrix equation is given by,

$$\begin{bmatrix} P_{CL-t,25^\circ\text{C},c} & P_{CL-t,25^\circ\text{C},b} & P_{CL-t,25^\circ\text{C},a} \\ P_{CL-t,125^\circ\text{C},c} & P_{CL-t,125^\circ\text{C},b} & P_{CL-t,125^\circ\text{C},a} \end{bmatrix} = \begin{bmatrix} -0.8995 & 1.551 & 0.02385 \\ -2.452 & 1.914 & 0.02876 \end{bmatrix} \quad (\text{A.4})$$

The equation of transistor-conduction power loss is in  $2^{nd}$  order, but the approximation of the  $1^{st}$  order determines the coefficients. In other words, when the loss equation is  $n^{th}$  order, then the related coefficient approximation should be the  $(n-1)^{th}$  order. Hence,

$$\begin{aligned}
c_0 &= \frac{P_{CL-t,25^{\circ}C,c} \times T_{max} - P_{CL-t,125^{\circ}C,c} \times T_{min}}{T_{max} - T_{min}} = -0.511375 \\
c_1 &= \frac{P_{CL-t,125^{\circ}C,c} - P_{CL-t,25^{\circ}C,c}}{T_{max} - T_{min}} = -0.015525 \\
b_0 &= \frac{P_{CL-t,25^{\circ}C,b} \times T_{max} - P_{CL-t,125^{\circ}C,b} \times T_{min}}{T_{max} - T_{min}} = 1.46025 \\
b_1 &= \frac{P_{CL-t,125^{\circ}C,b} - P_{CL-t,25^{\circ}C,b}}{T_{max} - T_{min}} = 0.00363 \\
a_0 &= \frac{P_{CL-t,25^{\circ}C,a} \times T_{max} - P_{CL-t,125^{\circ}C,a} \times T_{min}}{T_{max} - T_{min}} = 1.46025 \\
a_1 &= \frac{P_{CL-t,125^{\circ}C,a} - P_{CL-t,25^{\circ}C,a}}{T_{max} - T_{min}} = 0.00363
\end{aligned}$$

An equation A.3 can be rewritten as follows by substituting all the above coefficients,

$$\begin{aligned}
P_{CL}(i_t, T) &= -(0.511375 + 0.015525T) + (1.46025 + 0.00363T)i_t \\
&\quad + (0.0224 + 0.000058T)i_t^2
\end{aligned} \tag{A.5}$$

### A.1.2 Antiparallel diode-conduction power loss calculation ( $P_{CL-d}$ )

The antiparallel diode performs the same steps as the transistor did to estimate it's conduction power losses.

- Firstly, trace the corresponding diode characteristic curve  $V_d$  ( diode forward voltage drop) versus  $i - d$  (diode forward leakage current) from the datasheet shown in Figure A.5.
- Secondly, trace the samples for minimum and maximum temperatures from the diode characteristic curves, as listed in Table A.3 and Table A.4.
- Thirdly, consider the X and Y axis data of  $i_d$  and  $P_{CL-d}$  at  $T_{min} = 25^{\circ}C$  and  $T_{max} = 125^{\circ}C$ . These data are incorporated into the MATLAB curve fitting application to obtain the suitable loss equations in terms of  $i_d$ . Therefore, the optimized curve fitting graphs for diode-conduction power loss at  $T_{min} = 25^{\circ}C$  and  $T_{max} = 125^{\circ}C$  are shown in Figure A.6 and Figure A.7.

- Finally, Incorporate the temperature dependency in the conduction loss equation as similar to the equation A.3 for this antiparallel diode.

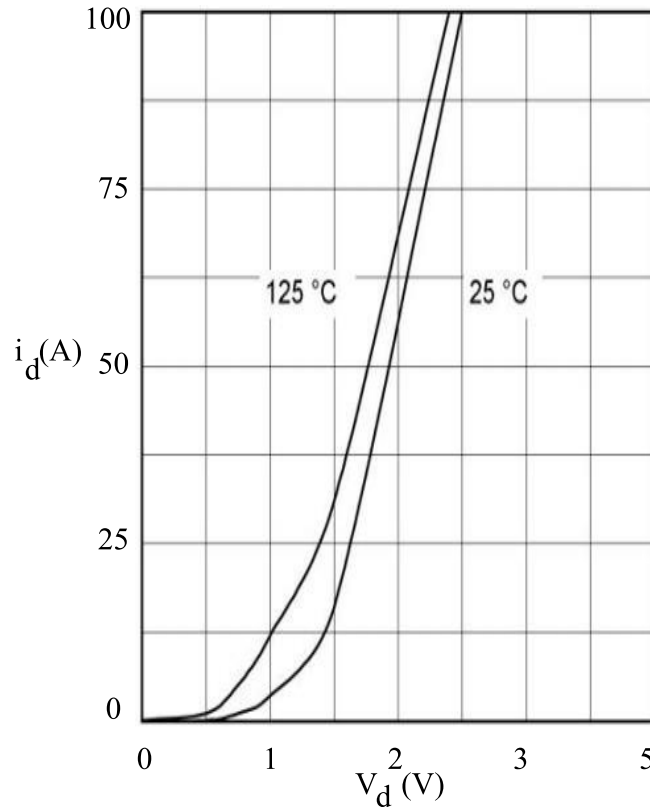


**Figure A.5:** SKM75GB123D diode characteristic curves at  $T_{min} = 25^\circ\text{C}$  and  $T_{max} = 125^\circ\text{C}$

**Table A.3:**  $V_{ce}-i_t$  curve extracted points for  $V_{ge} = 15$  V at  $T_{min} = 25^\circ\text{C}$

$V_d$ (V)	$i_d$ (A)	$P_{CL-d,25^\circ\text{C}} = (V_d \times i_d)$ (W)
0	0	0
0.5	0	0
1	2.8571	2.8571
1.5	17.1429	25.714
2	50	100



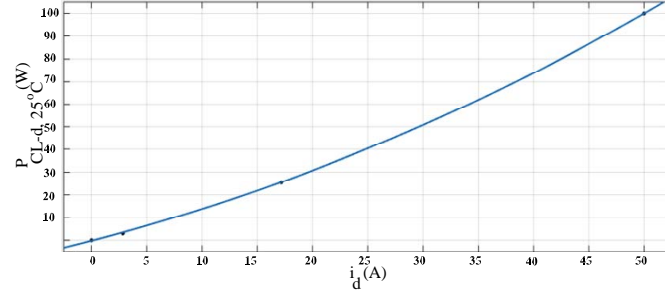


**Figure A.6:** Curve fitting graph for diode-conduction power loss at 25<sup>0</sup>C with respect to  $i_d$

**Table A.4:**  $V_{ce}-i_t$  curve extracted points for  $V_{ge}= 15$  V at  $T_{max}= 125^0$ C

$V_d$ (V)	$i_d$ (A)	$P_{CL-d,125^0C} = (V_d, \times i_d)$ (W)
0	0	0
0.5	1.7143	0.8571
1	10	10
1.5	30	45
2	64.2857	128.5714

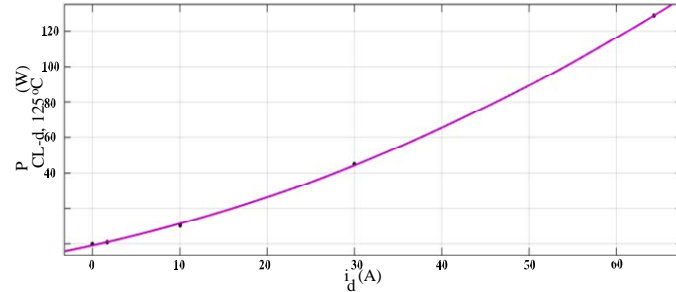


**Figure A.7:** Curve fitting graph for diode-conduction power loss at 125<sup>0</sup>C with respect to  $i_d$

From Figure A.6 and Figure A.7, the diode-conduction power loss equations are deduced as follows,

$$P_{CL-d,25^0C} = -0.2321 + 1.245i_d + 0.01521i_d^2 \quad (\text{A.6})$$

$$P_{CL-d,125^0C} = -0.8451 + 1.06i_d + 0.01485i_d^2 \quad (\text{A.7})$$

The generalized temperature-dependent conduction power loss equation of 2<sup>nd</sup> order is illustrated by,

$$P_{CL}(i_d, T) = (c_0 + c_1T) + (b_0 + b_1T)i_d + (a_0 + a_1T)i_d^2 \quad (\text{A.8})$$

Now, the coefficients matrix equation for diode-conduction power loss is derived as follows,

$$\begin{bmatrix} P_{CL-d,25^\circ C,c} & P_{CL-d,25^\circ C,b} & P_{CL-d,25^\circ C,a} \\ P_{CL-d,125^\circ C,c} & P_{CL-d,125^\circ C,b} & P_{CL-d,125^\circ C,a} \end{bmatrix} = \begin{bmatrix} -0.2321 & 1.245 & 0.01521 \\ -0.8451 & 1.06 & 0.01485 \end{bmatrix} \quad (\text{A.9})$$

From the equation A.9, the following coefficients are,

$$c_0 = \frac{P_{CL-d,25^\circ C,c} \times T_{max} - P_{CL-d,125^\circ C,c} \times T_{min}}{T_{max} - T_{min}} = -0.0789$$

$$c_1 = \frac{P_{CL-d,125^\circ C,c} - P_{CL-d,25^\circ C,c}}{T_{max} - T_{min}} = -0.0061$$

$$b_0 = \frac{P_{CL-d,25^\circ C,b} \times T_{max} - P_{CL-d,125^\circ C,b} \times T_{min}}{T_{max} - T_{min}} = 1.2913$$

$$b_1 = \frac{P_{CL-d,125^\circ C,b} - P_{CL-d,25^\circ C,b}}{T_{max} - T_{min}} = -0.0019$$

$$a_0 = \frac{P_{CL-t,25^\circ C,a} \times T_{max} - P_{CL-t,125^\circ C,a} \times T_{min}}{T_{max} - T_{min}} = 0$$

$$a_1 = \frac{P_{CL-t,125^\circ C,a} - P_{CL-t,25^\circ C,a}}{T_{max} - T_{min}} = 0.0153$$

An equation A.8 can be rewritten as follows by substituting all the above coefficients,

$$P_{CL}(i_d, T) = -(0.0789 + 0.0061T) + (1.2913 - 0.0019T)i_d + (0.0153T)i_d^2 \quad (\text{A.10})$$

## A.2 Switching Losses of the IGBT Switch

The switching losses usually contribute a notable weight in the total power electronic device losses. Switching loss analysis is essential to estimate the junction temperature for improving system reliability. (Chen and Downer, 2004) and (Drofenik and Kolar, 2005) used very simple calculations in MATLAB to estimate switching losses.

### A.2.1 Transistor-switching power loss calculation ( $P_{SL-t}$ )

The data-sheets of a semiconductor device are often provided the current dependency of the energy loss graphs as shown in the Figure A.8. Now, we have to trace and tabulate the total energy loss ( $E_{total}$ ) samples from Figure A.8 and is depicted in Table A.5. Herein, the ratio of the total switching energy loss ( $E_{on} + E_{off}$ ) to the current ( $i_t$ ) has defined the switching power loss ( $P_{(SL,t)}$ ) which can be approximated by a  $3^{rd}$  order polynomial curve fitting depicted in Figure A.9.

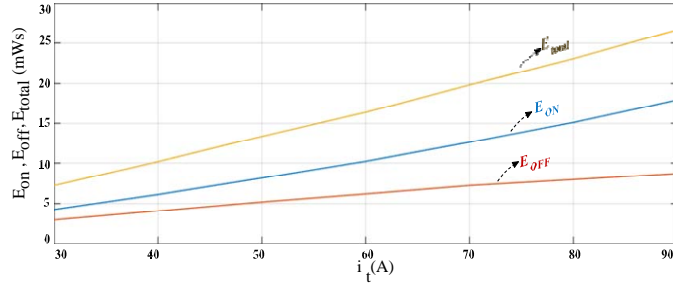


**Figure A.8:** Curve fitting graph for transistor-switching power loss at  $25^{\circ}\text{C}$  with respect to  $i_t$

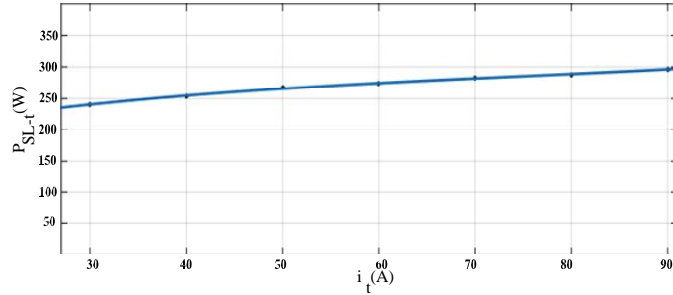


**Figure A.9:** Curve fitting graph for transistor-switching power loss at  $125^{\circ}\text{C}$  with respect to  $i_t$

$$P_{SL-t} = \frac{E_{total}}{i_t} \frac{\mu W s}{A} = 170.3 + 3.224i_t - 0.03366i_t^2 + 0.0001487i_t^3 \quad (\text{A.11})$$

**Table A.5:** Extraction of the samples for deducing the switching factor at  $T_{max} = 125^{\circ}\text{C}$

$i_t$ (A)	$E_{on}$ (mWs)	$E_{off}$ (mWs)	$E_{total}$ (mWs)	$P_{CL-t,125^{\circ}\text{C}}$ ( $\mu\text{Ws}/\text{A}$ )
30	4.2593	2.9630	7.2223	240.7
40	6.1111	4.0741	10.1852	254.6
50	8.1481	5.1852	13.3333	266.7
60	10.2222	6.1852	16.4074	273.5
70	12.5926	7.2222	19.8148	283.1
80	15.1111	7.9630	23.0741	288.4
90	17.9630	8.7037	26.6667	296.3

### A.2.2 Antiparallel diode-switching power loss calculation ( $P_{SL-d}$ )

As the diode turn-on energy losses are negligible, the only turn-off energy losses have taken into account. The turn-off energy loss concerning the diode forward current,  $i_d$ , is shown in Figure A.10. Herein, considered  $R_G = 24\omega$  from the data-sheet and proceeded the above-defined steps to find the diode switching power loss. Now, the final expression is derived as follows,

$$P_{SL-t} = \frac{E_{off} \mu\text{Ws}}{i_d \text{ A}} = 65.53 - 0.0436i_d - 0.00077266i_d^2 \quad (\text{A.12})$$

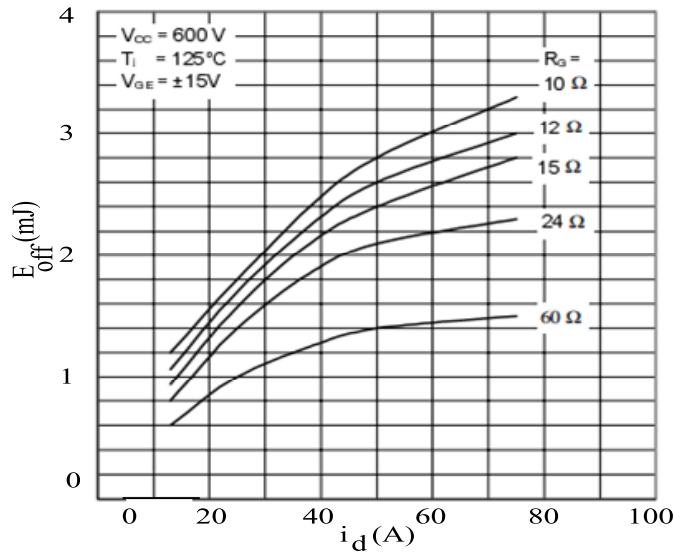


**Figure A.10:** Diode turn-off energy dissipation loss per one switching

# Bibliography

- Al Hadi, A., Fu, X., and Chaloo, R. (2018). Igbt module loss calculation and thermal resistance estimation for a grid-connected multilevel converter. In *Wide Bandgap Power and Energy Devices and Applications III*, volume 10754, page 107540F. International Society for Optics and Photonics.
- Appala, N. K., Suresh, Y., Kotturu, J., et al. (2013). Investigation on shunt active filter with pq theory. In *2013 International Conference on Circuits, Power and Computing Technologies (ICCPCT)*, pages 445–449. IEEE.
- Arul, P., Ramachandaramurthy, V. K., and Rajkumar, R. (2015). Control strategies for a hybrid renewable energy system: A review. *Renewable and sustainable energy reviews*, 42:597–608.
- Barua, A., Jain, A. K., Gupta, M., and Mishra, P. K. (2017). Control and techno-economic analysis of pv-diesel-battery based hybrid microgrid system. In *2017 Conference on Information and Communication Technology (CICT)*, pages 1–5. IEEE.
- Bhattacharjee, C. and Roy, B. K. (2016). Advanced fuzzy power extraction control of wind energy conversion system for power quality improvement in a grid tied hybrid generation system. *IET Generation, Transmission & Distribution*, 10(5):1179–1189.
- Biricik, S., Redif, S., Khadem, S. K., and Basu, M. (2016). Improved harmonic suppression efficiency of single-phase apfs in distorted distribution systems. *International Journal of Electronics*, 103(2):232–246.
- Boukettaya, G. and Krichen, L. (2014). A dynamic power management strategy of a

- grid connected hybrid generation system using wind, photovoltaic and flywheel energy storage system in residential applications. *Energy*, 71:148–159.
- Boukezata, B., Gaubert, J.-P., Chaoui, A., and Hachemi, M. (2016). Predictive current control in multifunctional grid connected inverter interfaced by pv system. *Solar Energy*, 139:130–141.
- Boutoubat, M., Mokrani, L., and Machmoum, M. (2013). Control of a wind energy conversion system equipped by a dfig for active power generation and power quality improvement. *Renewable Energy*, 50:378–386.
- Boutoubat, M., Mokrani, L., and Machmoum, M. (2014). Full capability of harmonic current mitigation for a wind energy system. *Electric Power Components and Systems*, 42(15):1743–1753.
- Chen, J. and Downer, S. (2004). Mosfet loss and junction temperature calculation model in matlab. In *Proc. PCIM*, volume 4, pages 23–27.
- Coelho, R. F., Schmitz, L., and Martins, D. C. (2015). Proposal of a power flow control strategy applied to a hybrid microgrid. In *2015 IEEE 13th Brazilian Power Electronics Conference and 1st Southern Power Electronics Conference (COBEP/SPEC)*, pages 1–6. IEEE.
- Drofenik, U. and Kolar, J. W. (2005). A general scheme for calculating switching- and conduction-losses of power semiconductors in numerical circuit simulations of power electronic systems. In *Proc. IPEC*, volume 5, pages 4–8.
- Eajal, A., Abdelwahed, M. A., El-Saadany, E., and Ponnambalam, K. (2016). A unified approach to the power flow analysis of ac/dc hybrid microgrids. *IEEE Transactions on Sustainable Energy*, 7(3):1145–1158.
- Eghtedarpour, N. and Farjah, E. (2014). Power control and management in a hybrid ac/dc microgrid. *IEEE transactions on smart grid*, 5(3):1494–1505.
- Eid, A. (2014). Utility integration of pv-wind-fuel cell hybrid distributed generation systems under variable load demands. *International Journal of Electrical Power & Energy Systems*, 62:689–699.

- Farshadnia, M. and Taher, S. A. (2014). Current-based direct power control of a dfig under unbalanced grid voltage. *International Journal of Electrical Power & Energy Systems*, 62:571–582.
- Fooladivanda, D., Zholbaryssov, M., and Dominguez-Garcia, A. D. (2017). Control of networked distributed energy resources in grid-connected ac microgrids. *IEEE Transactions on Control of Network Systems*.
- Gaillard, A., Poure, P., Saadate, S. a., and Machmoum, M. (2009). Variable speed dfig wind energy system for power generation and harmonic current mitigation. *Renewable Energy*, 34(6):1545–1553.
- Guo, S., Liu, Q., Sun, J., and Jin, H. (2018). A review on the utilization of hybrid renewable energy. *Renewable and Sustainable Energy Reviews*, 91:1121–1147.
- Gupta, A., Doolla, S., and Chatterjee, K. (2018). Hybrid ac–dc microgrid: systematic evaluation of control strategies. *IEEE Transactions on Smart Grid*, 9(4):3830–3843.
- Hirsch, A., Parag, Y., and Guerrero, J. (2018). Microgrids: A review of technologies, key drivers, and outstanding issues. *Renewable and sustainable Energy reviews*, 90:402–411.
- Hosseinzadeh, M. and Salmasi, F. R. (2015). Robust optimal power management system for a hybrid ac/dc micro-grid. *IEEE Transactions on Sustainable Energy*, 6(3):675–687.
- Hu, J., Shan, Y., Xu, Y., and Guerrero, J. M. (2019). A coordinated control of hybrid ac/dc microgrids with pv-wind-battery under variable generation and load conditions. *International Journal of Electrical Power & Energy Systems*, 104:583–592.
- Hu, J., Zhu, J., and Dorrell, D. G. (2014). Predictive direct power control of doubly fed induction generators under unbalanced grid voltage conditions for power quality improvement. *IEEE Transactions on Sustainable Energy*, 6(3):943–950.
- Hu, W., Chen, H., Yang, X., Xu, K., and Hu, P. (2015). Control strategy of the bi-directional converter for hybrid ac/dc microgrid. In *2015 IEEE PES Asia-Pacific Power and Energy Engineering Conference (APPEEC)*, pages 1–5. IEEE.

- Jayalakshmi, N., Gaonkar, D., and Kumar, K. S. K. (2012). Dynamic modeling and performance analysis of grid connected pmsg based variable speed wind turbines with simple power conditioning system. In *2012 IEEE International Conference on Power Electronics, Drives and Energy Systems (PEDES)*, pages 1–5. IEEE.
- Justo, J. J., Mwasilu, F., Lee, J., and Jung, J.-W. (2013). Ac-microgrids versus dc-microgrids with distributed energy resources: A review. *Renewable and sustainable energy reviews*, 24:387–405.
- Karabiber, A., Keles, C., Kaygusuz, A., and Alagoz, B. B. (2013). An approach for the integration of renewable distributed generation in hybrid dc/ac microgrids. *Renewable Energy*, 52:251–259.
- Kesraoui, M., Chaib, A., Meziane, A., and Boulezaz, A. (2014). Using a dfig based wind turbine for grid current harmonics filtering. *Energy Conversion and Management*, 78:968–975.
- Khanh, L. N., Seo, J.-J., Kim, Y.-S., and Won, D.-J. (2010). Power-management strategies for a grid-connected pv-fc hybrid system. *IEEE transactions on power delivery*, 25(3):1874–1882.
- Krishna, K. S. and Kumar, K. S. (2015). A review on hybrid renewable energy systems. *Renewable and Sustainable Energy Reviews*, 52:907–916.
- Krithiga, S. and Gounden, N. A. (2014). An improved power electronic controller with unity power factor for a single-stage grid-tied pv system. *Arabian Journal for Science and Engineering*, 39(10):7173–7182.
- Kumar, D. and Zare, F. (2015). Harmonic analysis of grid connected power electronic systems in low voltage distribution networks. *IEEE Journal of Emerging and selected topics in Power Electronics*, 4(1):70–79.
- Kumar, M., Srivastava, S., and Singh, S. (2015a). Control strategies of a dc microgrid for grid connected and islanded operations. *IEEE Transactions on Smart Grid*, 6(4):1588–1601.
- Kumar, M. M., Mishra, M. K., and Kumar, C. (2015b). A grid-connected dual voltage source inverter with power quality improvement features. *IEEE Transactions on Sustainable Energy*, 6(2):482–490.



- Li, L., Nian, H., Ding, L., and Zhou, B. (2017). Direct power control of dfig system without phase-locked loop under unbalanced and harmonically distorted voltage. *IEEE Transactions on energy conversion*, 33(1):395–405.
- Liang, B., Kang, L., He, J., Zheng, F., Xia, Y., Zhang, Z., Zhang, Z., Liu, G., and Zhao, Y. (2019). Coordination control of hybrid ac/dc microgrid. *The Journal of Engineering*, 2019(16):3264–3269.
- Liu, X., Wang, P., and Loh, P. C. (2011). A hybrid ac/dc microgrid and its coordination control. *IEEE Transactions on smart grid*, 2(2):278–286.
- Mahela, O. P. and Shaik, A. G. (2016). Topological aspects of power quality improvement techniques: A comprehensive overview. *Renewable and Sustainable Energy Reviews*, 58:1129–1142.
- Majumder, R. (2013). A hybrid microgrid with dc connection at back to back converters. *IEEE Transactions on Smart Grid*, 5(1):251–259.
- Mehrasa, M., Pouresmaeil, E., Zabihi, S., Rodrigues, E. M., and Catalão, J. P. (2016). A control strategy for the stable operation of shunt active power filters in power grids. *Energy*, 96:325–334.
- Mishra, A., Tripathi, P., and Chatterjee, K. (2018). A review of harmonic elimination techniques in grid connected doubly fed induction generator based wind energy system. *Renewable and Sustainable Energy Reviews*, 89:1–15.
- Moreira, A. B., Barros, T. A., Teixeira, V. S., and Ruppert, E. (2017). Power control for wind power generation and current harmonic filtering with doubly fed induction generator. *Renewable energy*, 107:181–193.
- Munir, S. and Li, Y. W. (2013). Residential distribution system harmonic compensation using pv interfacing inverter. *IEEE transactions on smart grid*, 4(2):816–827.
- Nehrir, M., Wang, C., Strunz, K., Aki, H., Ramakumar, R., Bing, J., Miao, Z., and Salameh, Z. (2011). A review of hybrid renewable/alternative energy systems for electric power generation: Configurations, control, and applications. *IEEE Transactions on Sustainable Energy*, 2(4):392–403.

- Nejabatkhah, F. and Li, Y. W. (2014). Overview of power management strategies of hybrid ac/dc microgrid. *IEEE Transactions on Power Electronics*, 30(12):7072–7089.
- Nejabatkhah, F., Li, Y. W., and Tian, H. (2019). Power quality control of smart hybrid ac/dc microgrids: An overview. *IEEE Access*, 7:52295–52318.
- Nian, H., Cheng, P., and Zhu, Z. (2015). Coordinated direct power control of dfig system without phase-locked loop under unbalanced grid voltage conditions. *IEEE Transactions on Power Electronics*, 31(4):2905–2918.
- Nian, H. and Song, Y. (2013). Direct power control of doubly fed induction generator under distorted grid voltage. *IEEE Transactions on Power Electronics*, 29(2):894–905.
- Ouchen, S., Betka, A., Abdeddaim, S., and Menadi, A. (2016). Fuzzy-predictive direct power control implementation of a grid connected photovoltaic system, associated with an active power filter. *Energy conversion and management*, 122:515–525.
- Planas, E., Andreu, J., Gárate, J. I., de Alegría, I. M., and Ibarra, E. (2015). Ac and dc technology in microgrids: A review. *Renewable and Sustainable Energy Reviews*, 43:726–749.
- Pouresmaeil, E., Akorede, M. F., Montesinos-Miracle, D., Gomis-Bellmunt, O., and Caballero, J. C. T. (2014). Hysteresis current control technique of vsi for compensation of grid-connected unbalanced loads. *Electrical engineering*, 96(1):27–35.
- Radwan, A. A. A. and Mohamed, Y. A.-R. I. (2014). Networked control and power management of ac/dc hybrid microgrids. *IEEE Systems Journal*, 11(3):1662–1673.
- Raj, G. S. and Rathi, K. (2015). Pq theory based shunt active power filter for power quality under ideal and non-ideal grid voltage conditions. In *2015 International Conference on Power, Instrumentation, Control and Computing (PICC)*, pages 1–5. IEEE.
- Rajesh, K., Dash, S., Rajagopal, R., and Sridhar, R. (2017). A review on control of ac microgrid. *Renewable and sustainable energy reviews*, 71:814–819.

- Rani, B. I., Ilango, G. S., and Nagamani, C. (2012). Power flow management algorithm for photovoltaic systems feeding dc/ac loads. *Renewable energy*, 43:267–275.
- Rani, M. A., Nagamani, C., Ilango, G. S., and Karthikeyan, A. (2014). An effective reference generation scheme for dfig with unbalanced grid voltage. *IEEE Transactions on Sustainable Energy*, 5(3):1010–1018.
- Sahoo, S. K., Sinha, A. K., and Kishore, N. (2017). Control techniques in ac, dc, and hybrid ac–dc microgrid: A review. *IEEE Journal of Emerging and Selected Topics in Power Electronics*, 6(2):738–759.
- Singh, M., Khadkikar, V., Chandra, A., and Varma, R. K. (2010). Grid interconnection of renewable energy sources at the distribution level with power-quality improvement features. *IEEE transactions on power delivery*, 26(1):307–315.
- Sivakumar, P. and Arutchelvi, M. S. (2018). Modified composite power control strategy for grid connected wind-pv systems with unbalanced nonlinear current. *International Transactions on Electrical Energy Systems*, 28(9):e2587.
- Song, Y. and Nian, H. (2014). Modularized control strategy and performance analysis of dfig system under unbalanced and harmonic grid voltage. *IEEE Transactions on Power Electronics*, 30(9):4831–4842.
- Sun, D. and Wang, X. (2016). Low-complexity model predictive direct power control for dfig under both balanced and unbalanced grid conditions. *IEEE Transactions on Industrial Electronics*, 63(8):5186–5196.
- Sundaramoorthy, K. and Sankar, A. (2014). Performance evaluation of a control strategy developed for a hybrid energy system integrated in dc-ac microgrids. *Electric Power Components and Systems*, 42(15):1762–1770.
- Tareen, W. U., Mekhilef, S., Seyedmahmoudian, M., and Horan, B. (2017). Active power filter (apf) for mitigation of power quality issues in grid integration of wind and photovoltaic energy conversion system. *Renewable and Sustainable Energy Reviews*, 70:635–655.

- Trinh, Q.-N. and Lee, H.-H. (2014). An enhanced grid current compensator for grid-connected distributed generation under nonlinear loads and grid voltage distortions. *IEEE Transactions on Industrial Electronics*, 61(12):6528–6537.
- Unamuno, E. and Barrena, J. A. (2015a). Hybrid ac/dc microgrids—part i: Review and classification of topologies. *Renewable and Sustainable Energy Reviews*, 52:1251–1259.
- Unamuno, E. and Barrena, J. A. (2015b). Hybrid ac/dc microgrids—part ii: Review and classification of control strategies. *Renewable and Sustainable Energy Reviews*, 52:1123–1134.
- Venkataramanaiah, J. and Suresh, Y. (2018). Performance verification of a new cascaded transformer based multilevel inverter using modified carrier spwm strategy. In *2018 International Conference on Power, Instrumentation, Control and Computing (PICC)*, pages 1–6. IEEE.
- Villalva, M. G., Gazoli, J. R., and Ruppert Filho, E. (2009). Comprehensive approach to modeling and simulation of photovoltaic arrays. *IEEE Transactions on power electronics*, 24(5):1198–1208.
- Wang, P., Goel, L., Liu, X., and Choo, F. H. (2013). Harmonizing ac and dc: A hybrid ac/dc future grid solution. *IEEE Power and Energy Magazine*, 11(3):76–83.
- Wu, G., Ono, Y., and Alishahi, M. (2015). Development of a resilient hybrid microgrid with integrated renewable power generations supplying dc and ac loads. In *2015 IEEE International Telecommunications Energy Conference (INTELEC)*, pages 1–5. IEEE.
- Xia, Y., Peng, Y., Yang, P., Yu, M., and Wei, W. (2016). Distributed coordination control for multiple bidirectional power converters in a hybrid ac/dc microgrid. *IEEE Transactions on Power Electronics*, 32(6):4949–4959.
- Yallamilli, R. S. and Mishra, M. K. (2016). Power management of grid connected hybrid microgrid with dual voltage source inverter. In *2016 IEEE International Conference on Renewable Energy Research and Applications (ICRERA)*, pages 407–412. IEEE.

- Yi, Z., Dong, W., and Etemadi, A. H. (2018). A unified control and power management scheme for pv-battery-based hybrid microgrids for both grid-connected and islanded modes. *IEEE Transactions on Smart Grid*, 9(6):5975–5985.
- Zandzadeh, M. J. and Vahedi, A. (2014). Modeling and improvement of direct power control of dfig under unbalanced grid voltage condition. *International Journal of Electrical Power & Energy Systems*, 59:58–65.
- Zhu, J.-p., Zhou, J.-p., and Zhang, H. (2014). Research progress of ac, dc and their hybrid micro-grids. In *2014 IEEE International Conference on System Science and Engineering (ICSSE)*, pages 158–161. IEEE.
- Zolfaghari, M., Abedi, M., and Gharehpetian, G. B. (2019). Power flow control of interconnected ac-dc microgrids in grid-connected hybrid microgrids using modified uipc. *IEEE Transactions on Smart Grid*.



# PUBLICATIONS BASED ON THE RESEARCH WORK

## Refereed journal publications

1. **C. Nagaraj.** and K. Manjunatha Sharma. (2019) 'Bi-directional power flow control with improved power quality using intelligent controller for AC-DC coupled hybrid micro-grid system', *International Journal of Power Electronics*, Article in Press.
2. **Nagaraj C.** and K Manjunatha Sharma. (2019) 'Coordinated Bidirectional Power Flow Management with Power Quality Improvement in AC-DC Hybrid Micro-grid under Unbalanced Scenario', *Majlesi Journal of Electrical Engineering*, vol. 13, no. 1, pp. 109-119.
3. **Nagaraj C.** and K Manjunatha Sharma. (2018) 'Fuzzy PI controller for bidirectional power flow applications with harmonic current mitigation under unbalanced scenario', *AIMS Energy*, vol. 6, no. 5, pp. 695-709.

## Refereed papers in conference proceedings

1. **Nagaraj C** and K Manjunatha Sharma. 'Integration of hybrid solar-wind energy sources with utility grid for improving power quality', *Proceedings of the 3<sup>rd</sup> IEEE International Conference on Recent Trends in Electronics, Information and Communication Technology (RTEICT-2018)*, Bengaluru, May 2018, pp. 1644-1648.
2. **Nagaraj C** and K Manjunatha Sharma. 'Harmonic Current Compensation Improvement at Point of Common Coupling Using Hybrid Natural Green Sources', *Proceedings of the 3<sup>rd</sup> IEEE International Conference on Advances in Electrical, Electronics, Information, Communication and Bio-Informatics (AEEICB-2017)*, Chennai, Feb. 2017, pp. 406-410.
3. **Nagaraj C** and K Manjunatha Sharma. 'Improvement of harmonic current compensation for grid integrated PV and wind hybrid renewable energy system', *Proceedings of the 6<sup>th</sup> IEEE International Conference on Power Systems (ICPS-2016)*, New Delhi, March 2016, pp. 1-6.





## Bio-data

Name: Nagaraj C

Date of birth: 15-09-1985

Marital status: Married

E-mail: nagarajc\_ee13f02@nitk.edu.in, assiniraj@gmail.com

Mobile: +91-9916444330, +91-8904330654

### Permanent Address

S/o: Chinnamadha

No.23, Nethravathy Nilaya

Basthipura Road, Kollegal Town

Chamarajnagara District

Karnataka, 571440, India.

### Education Qualification

- **Ph.D.** in Electrical and Electronics Engineering (Pursuing)  
Institute: National Institute of Technology Karnataka (Deemed University), Surathkal
- **M.Tech.** in Power Systems (2010)  
Institute: The National Institute of Engineering (Autonomous College), Mysuru  
University: Visvesvaraya Technological University, Belagavi  
CGPA: 8.74
- **B.E.** in Electrical and Electronics Engineering (2008)  
Institute: P.E.S college of engineering, Mandya  
University: Visvesvaraya Technological University, Belagavi  
Percentage: 63.19